

G.A. n° 270086

Collaborative Project of the 7th Framework Programme



WP4: Vertical model integration

**Deliverable 4.2: Plan for vertical integration and
assessment of complementary
tools to enhance modelling**

v.0.7 30/11/11

www.Synergy-COPD.eu

Document Information

Project Number	270086	Acronym	Synergy-COPD
Full title	Modelling and simulation environment for systems medicine (Chronic obstructive pulmonary disease -COPD- as a use case)		
Project URL	http://www.Synergy-COPD.eu		
EU Project officer	Marta Lorens		

Deliverable	Number	4.2	Title	Plan for vertical integration and assessment of complementary tools to enhance modelling
Work package	Number	4	Title	Vertical model integration

Date of delivery	Contractual	PM09	Actual	PM10
Nature	Prototype <input type="checkbox"/> Report <input checked="" type="checkbox"/> Dissemination <input type="checkbox"/> Other <input type="checkbox"/>			
Dissemination Level	Public <input checked="" type="checkbox"/> Consortium <input type="checkbox"/> Restricted <input type="checkbox"/> ()			

Document responsible	Dr. Josep Roca		Email	jroca@clinic.ub.es
	Partner	IDIBAPS	Phone	(+34) 932 275 400, ext. 2698

Authors	Name	Partner
Main author(s)	Isaac Cano	IDIBAPS
Co-author(s)	Josep Roca	IDIBAPS
	Vitaly Selivanov	IDIBAPS
	Igor Marin	IDIBAPS
	Marta Cascante	IDIBAPS
	Peter D. Wagner	External Advisor
	Filip Velickovski	BDIGITAL
	Kelly Burrowes	UOXF.BL
	Dieter Maier	BIOMAX
	David Gomez-Cabrero	KI
	Jesper Tegner	KI
	Michel Mickael	KI
	Francesco Falciani	BHAM

Abstract (for dissemination)	<p>The deliverable describes the tasks and the roadmap relative to the generation of an operational prototype covering full automatic vertical integration of the three composite models (i.e. <i>Oxygen Transport and Utilization, Spatial Heterogeneities of Lung Ventilation and Perfusion and Cell Bioenergetics, Mitochondrial Respiration and Reactive Oxygen Species Generation</i>) described in detail in D4.1: <i>Assessment of software tools used for mechanistic modelling at each level of the body</i>. The current document describes the main dimensions and strategies for model optimization (Section 2) taken into account in the project (i.e. <i>Sensitivity Analysis; Model Reduction; Numerical Bifurcation Analysis; Code Optimization and Workflow on Disease Development</i>). In Section 3, we specify the tasks covering different levels of integration among the mechanistic models to achieve full vertical integration (M8). In Section 4, the deliverable addresses the strategy planned for the development of the simulation environment based on interactions between mechanistic and probabilistic modelling. The Section also analyses the architecture of the Clinical Decision Support System (CDSS) and its interactions with the simulation environment.</p>
Key words	<p>Mechanistic modelling, probabilistic modelling, model optimisation, model integration, simulation environment, clinical decision support system.</p>

Version Log			
Issue Date	Version	Author	Change
10/10/2011	0.1	All partners involved	Specific demands to all partners involved.
24/10/2011	0.2	Isaac Cano, David Gomez-Cabrero, Vitaly Selivanov, Kelly Burrowes	First draft text considering input from partners involved.
10/11/2011	0.3	All partners involved	Final draft text for the overview to all partners
20/11/2011	0.4	All partners involved	Submitted document (v. 0.3) reviewed
23/11/2011	0.5	All partners involved	Final demands to all partners from previous review.
28/11/2011	0.6	All partners involved	Final review of the complete manuscript.
29/11/2011	0.7	All partners involved	Final review and document closed.

Index

1	INTRODUCTION.....	7
2	THE BASICS FOR MODEL ANALYSIS AND REFINEMENT.....	8
2.1	THE BASICS FOR MODEL ANALYSIS AND REFINEMENT.....	8
2.2	A CASE MODEL.....	8
2.3	SENSITIVITY ANALYSIS.....	9
2.4	MODEL REDUCTION.....	10
2.5	NUMERICAL BIFURCATION ANALYSIS.....	11
2.6	CODE OPTIMISATION.....	11
2.7	STATUS OF MODEL OPTIMIZATION IN SYNERGY-COPD.....	11
2.8	MECHANISTIC MODELLING IN THE PROJECT.....	12
2.9	TARGETS FOR THE SIMULATION ENVIRONMENT IN SYNERGY-COPD.....	13
2.10	ROADMAP.....	14
3	DESIGN FOR SYNERGY-COPD MECHANISTIC MODELS INTEGRATION.....	15
3.1	IMPACT OF SPATIAL HETEROGENEITIES OF LUNG VENTILATION AND PERFUSION.....	15
3.1.1	<i>Rationale.....</i>	<i>15</i>
3.1.2	<i>Predicting V/Q in patient-specific models derived from the PAC-COPD database.....</i>	<i>15</i>
3.2	LUNG FUNCTIONAL HETEROGENEITIES.....	18
3.2.1	<i>Rationale.....</i>	<i>18</i>
3.2.2	<i>Incorporating lung functional heterogeneities to the oxygen transport and utilization model M6....</i>	<i>19</i>
3.3	FUNCTIONAL HETEROGENEITIES OF PERIPHERAL GAS EXCHANGE.....	22
3.3.1	<i>Rationale.....</i>	<i>22</i>
3.3.2	<i>Incorporating peripheral functional heterogeneities to the oxygen transport and utilization model M6</i>	<i>22</i>
3.4	INTEGRATION AMONG O ₂ TRANSPORT, CENTRAL METABOLISM AND ROS GENERATION.....	22
3.4.1	<i>Rationale.....</i>	<i>22</i>
3.4.2	<i>Oxygen consumption described in the model of mitochondrial respiration.....</i>	<i>23</i>
3.4.3	<i>Oxygen transport from lung to tissues.....</i>	<i>24</i>
3.4.4	<i>Linking the models of mitochondrial respiration and oxygen transport.....</i>	<i>25</i>
4	INTERACTIONS BETWEEN: MECHANISTIC MODELS, “DE NOVO” PROBABILISTIC MODELS AND CDSS.....	29
4.1	INTRODUCTION.....	29
4.2	DATA, MODELS AND INTERACTIONS: CONCEPTS AND DEFINITIONS.....	29
4.2.1	<i>Data.....</i>	<i>30</i>
4.2.2	<i>Models.....</i>	<i>31</i>
4.2.3	<i>A visualization of the connections.....</i>	<i>32</i>
4.3	WORK-PLAN.....	33
4.3.1	<i>Phase I: ROS levels.....</i>	<i>34</i>
4.3.2	<i>Phase II: differential pathways between Group I and Group III of PAC-COPD.....</i>	<i>34</i>
4.3.3	<i>Phase III: shared pathways among co-morbidity studies.....</i>	<i>35</i>
4.4	ADDITIONAL CONSIDERATIONS.....	36
4.4.1	<i>Simulation environment and CDSS (SE-CDSS).....</i>	<i>36</i>
4.4.2	<i>Data and model processing.....</i>	<i>37</i>
4.4.3	<i>Inference of Quantitative Probabilistic Networks (IQPN).....</i>	<i>38</i>
5	REFERENCES.....	39
6	LIST OF KEY WORDS/ABBREVIATIONS.....	45
7	ANNEX 1: MODEL ANALYSIS AND REFINEMENT FOR THE SYNERGY-COPD MECHANISTIC MODELS.....	46
7.1	SENSITIVITY ANALYSIS.....	46
7.1.1	<i>Sensitivity analysis for the model of mitochondrial respiration with regards to parameters.....</i>	<i>46</i>
7.2	MODEL REDUCTION.....	46

7.2.1	<i>Reduction of the mitochondrial respiration model</i>	46
7.2.2	<i>Model reduction for the oxygen transport and utilisation model</i>	49
7.3	NUMERICAL BIFURCATION ANALYSIS	50
7.3.1	<i>Numerical bifurcation analysis of the respiratory chain</i>	50
7.4	CODE OPTIMISATION	56
7.4.1	<i>Code optimisation within M6</i>	56
8	ANNEX 2: SUPPORTING MATERIAL FOR THE DETAILED MODEL OF RESPIRATORY CHAIN	57
9	ANNEX 3: SUPPORTING TABLE FOR THE SENSITIVITY ANALYSIS OF MODEL M7	58
10	ANNEX 4: ROADMAP	59

List of figures

FIGURE 1:	TRAJECTORY OF A CASE-MODEL	9
FIGURE 2:	WORKFLOW TO ANALYSE TIME-TRAJECTORIES IN ODE MODELS	12
FIGURE 3:	CONSTRUCTION OF DISEASE PROGRESSION ESTIMATION IN M6	14
FIGURE 4:	SCHEMATIC ILLUSTRATION OF THE PROCESSES INVOLVED IN CREATING THE ANATOMICALLY-BASED GEOMETRIC MODELS OF THE LUNGS, AIRWAYS AND BLOOD VESSELS	16
FIGURE 5:	ILLUSTRATION OF THE PROCESSES INVOLVED IN THE FUNCTIONAL MODELS	17
FIGURE 6:	PREDICTIONS FOR VENTILATION (LEFT), PERFUSION (CENTER) AND V/Q (RIGHT) PER ACINUS WITHIN THE ANATOMICALLY-BASED LUNG MODEL	17
FIGURE 7:	DISTRIBUTION OF V, Q AND V/Q OVER THE HEIGHT OF THE LUNG (LEFT) AND THE LOG-NORMAL DISTRIBUTION OF V/Q VALUES INCORPORATING ALL 30,000 ACINAR VALUES (RIGHT)	18
FIGURE 8:	SCHEMATIC DESCRIPTION OF THE MAIN COMPONENTS OF THE OXYGEN TRANSPORT AND UTILISATION MODEL (M6)	19
FIGURE 9:	SCHEMATIC DESCRIPTION OF THE MAIN COMPONENTS OF THE OXYGEN TRANSPORT AND UTILISATION CONSIDERING LUNG FUNCTIONAL HETEROGENEITIES	21
FIGURE 10:	TYPES OF MODELS USED IN SYNERGY-COPD	31
FIGURE 11:	ORGANIZATION OF MODELS AND ENTITIES	32
FIGURE 12:	RELATION BETWEEN DATA TYPES, MODELS AND TARGETED USERS	33
FIGURE 13:	CDSS AND SIMULATION ENVIRONMENT	36
FIGURE 14:	IMPACT IN OXYGEN DELIVERY WHEN USING (GREEN) AND NOT USING (BLUE) EQ. 27	49
FIGURE 15:	MULTIPLE STEADY STATE SOLUTIONS FOR THE ODE SYSTEM CORRESPONDING TO THE SIMPLIFIED MODEL OF COMPLEX III (MODEL 145)	50
FIGURE 16:	MULTIPLE STEADY STATE SOLUTIONS FOR THE MODEL OF COMPLEX III CONSISTING OF 257 ODES IN THE SPACE OF THE PARAMETER REFLECTING SUCCINATE CONCENTRATION	51
FIGURE 17:	MULTIPLE STEADY STATES FOR THE INTEGRATED MODELS OF COMPLEX I AND III (MODEL 267) IN THE SPACE OF THE PARAMETER REFLECTING SUCCINATE CONCENTRATION	52
FIGURE 18:	INFINITE INTERVAL OF MULTIPLE STEADY STATES FOR THE INTEGRATED MODELS OF COMPLEXES I AND III (MODEL 267) AS A FUNCTION OF SUCCINATE CONCENTRATION ($V_{M_{SDH}}$)	53
FIGURE 19:	MULTIPLE STEADY STATES AT VARIOUS PYRUVATE CONCENTRATIONS	53
FIGURE 20:	SUSTAINED OSCILLATIONS OF LEVELS OF SQ BOUND AT QO SITE AND $\Delta\Psi$ IN MODEL 272	55

Executive Summary

The current deliverable “**Plan for vertical integration and assessment of complementary tools to enhance modelling**” (D4.2) describes the tasks and associated calendar relative to the generation of an operational prototype covering full automatic vertical integration (model M8) of the three composite Models (M) described in detail in D4.1 (*Assessment of software tools used for mechanistic modelling at each level of the body*), that is:

- ✓ M6 - Oxygen Transport and Utilization (M1+M2 of the Description of Work, DoW)
- ✓ M3 - Spatial Heterogeneities of Lung Ventilation and Perfusion
- ✓ M7- Cell Bioenergetics, Mitochondrial Respiration and Reactive Oxygen Species Generation (M4+M5 of the DoW)

The first part of the document (**Section 1**) discusses the structure of D4.2 and identifies pivotal milestones that are being considered in the roadmap of the project.

Section 2 includes basic definitions and examples of the main dimensions of model optimization taken into account in the project. Those dimensions are: *Sensitivity Analysis, Model Reduction, Numerical Bifurcation Analysis, Code Optimization and Workflow on Disease Development*. An extensive amount of work in this field has been completed for Cell Bioenergetics, Mitochondrial Respiration and Reactive Oxygen Species Generation model M7. To facilitate the reading of the document, a detailed report of M7 results is displayed in Annex 1. Section 2 ends with a summary of the current status and plans for model optimization by model and for the entire model resulting from vertical integration.

Section 3 is dedicated to the specificities of the tasks covering different levels of integration among the three mechanistic models (M3, M6 and M7). In this section, we describe the rationale behind each model and the technological steps planned to achieve full vertical integration (M8). Specific future studies to be undertaken within the scope of the section are reported.

Section 0 updates current knowledge of the interactions between mechanistic and probabilistic modelling aiming at enhancing our understanding of abnormal metabolic pathways that are:

- ✓ associated with each one of the three clinical Chronic Obstructive Pulmonary Disease (COPD) phenotypes identified in PAC_COPD (Garcia-Aymerich et al. 2011).
- ✓ shared by common clusters of co-morbid conditions observed in COPD patients.

In addition, the relation of the simulation environment with the vertical integration and its interaction with probabilistic modelling are described. Also, we address the strategy planned for the full development of the interaction between mechanistic and probabilistic modelling within the frame of the project. A high level description of some specific studies associated to such strategy is also reported. Finally, we address some general considerations regarding the architecture of the Clinical Decision Support System (CDSS), that will be further developed within the context of Work Package 6 (WP6: Tools for bio-researchers and clinicians).

1 Introduction

A **reductionist approach** to the current deliverable should keep its content constrained to two main domains:

- ✓ First, those issues addressing technological integration of the three composite models mentioned in the Executive Summary (M6, M3 and M7) into a fully operational integrated model (M8) describing the relationships among oxygen transport, cell bioenergetics and mitochondrial ROS generation.
- ✓ Second, the analysis and use of available tools for model optimization

Sections 2, 3 and the Annexes of the current D4.2 fully cover the two domains of the reductionist approach. In those sections, besides a conceptual description of the working plan, we specifically identify: a) the achievements done; b) the calendar for those items still in progress; and, c) ancillary studies and planned manuscripts to be done during the project's lifetime.

In the best possible scenario, the fundamental outcomes from M8 will be accurate estimations of muscle ROS levels when varying the characteristics of oxygen transport to the cell. Consequently, in all circumstances, the end result of this reductionist approach will place us far away from the main aim of the project, that is, to significantly enhance our knowledge on underlying mechanisms that explain the three clinical phenotypes identified in PAC_COPD (Garcia-Aymerich et al. 2011).

A **holistic approach** to the deliverable must address the role of the interactions between mechanistic (M8) and probabilistic modelling, as an appropriate strategy aiming at bridging changes in well-established mechanistic processes (M8) with abnormalities in metabolic pathways assessed using network analysis. The potential and achievements in the entire area are described in Section 0 of the document. It is of note that the interactions between mechanistic and probabilistic modelling will be the core element conforming simulation environment and will be useful to generate "in silico" hypothesis to explore biological complexities of COPD patients.

We acknowledge the challenges faced in both technological and biological domains because of the novelty and the complexity of the approach. Those circumstances advise us to progress using a strategy with strong interactions between technology and biology. Steps for progression in this area are described in Section 0.

Finally, the deliverable additionally explores, in a preliminary manner, the implications of the deployment of a *Clinical Decision Support System* (CDSS) on the overall architecture of the Synergy-COPD system. In other words, we have conceived the deliverable with a broad scope covering its fundamental aims, but also displaying a general roadmap for a substantial portion of the project.

2 The basics for model analysis and refinement

This section does a brief description of the basics of mechanistic modelling using Ordinary Differential Equations (ODE) and identifies the key dimensions to be considered for the Synergy-COPD model optimization. To facilitate readability of the document, the body of the text only describes the definition and a short example of each dimension, but a full development of each item is displayed in Annex 1 taking M7 (*Cell Bioenergetics and Mitochondrial ROS generation*) as a model wherein all items have essentially been completed.

The status of the remaining models (M6 and M3) and future plans for the integrated model M8 are summarized under Subsection 2.7 (*Status of Model Optimization*). In the final part of this section, we briefly analyse the limitations of mechanistic modelling for the purposes of the current project (Subsection 2.8) and the three main areas of Synergy-COPD that could potentially be addressed with modelling indicating the two main items to be covered during the lifetime of the project and indicating potential developments beyond Synergy-COPD.

2.1 The basics for model analysis and refinement

Mathematical models (MM) are useful in providing an understanding of complex biological systems. For the development of MM, it is necessary to follow the following steps: model selection, model fitting and model validation.

Model selection denotes the process of translating the chemical and physical rules governing a system into mathematical equations; in very few cases the knowledge of the system allows the development of a model with complete certainty, on the contrary in most of the cases the model is uncertain. Usually different models can be constructed based on the state-of-the-art knowledge of the selected biological system; methods have been developed to analyse or select among competing model options (Tigges et al. 2009). However it is a very challenging field and the selected model reflects in most cases the opinions and intuition of the modeller.

Model fitting is the process of model parameter values estimation based on quantitative data or qualitative knowledge.

Finally the *model must be validated* by the predictions it generates.

The previous paragraphs present an over-simplification of the modeller's task. Once a model is defined many different sub-steps need to be performed in order to both understand and optimize a model. In this section we describe a subset of those steps that are relevant to the Synergy-COPD models. At the end of the section we provide a summary of the status of the tasks (if it applies) for each model. In Synergy-COPD, the mechanistic models were properly defined in D4.1 and those models are considered to have correct estimated parameters.

2.2 A case model

The Ordinary Differential Equation (ODE) Case-Model (CM) described below is intended to be used as an example to illustrate the different dimensions of model analysis and refinement addressed in the current section of the document. The ODE CM is based on the following description of an ODE system:

$$\frac{dx_i(t)}{dt} = f(t, x_1, \dots, x_n, \alpha_1, \dots, \alpha_m) \quad (1)$$

$$x_i(t_0) = x_i^0, i = 1, \dots, n \quad (2)$$

Where $x_i, i=1, \dots, n$ denote the state variables and $\alpha_j, j=1, \dots, m$ denote the parameters of the system. The state of an ODE system at any given time is defined by the vector $x(t)$. Considering this definition of ODE systems, the CM is defined as:

$$\frac{dx_1(t)}{dt} = -(\alpha_1 + \alpha_3)x_1^2 + \alpha_2x_2^2 \quad (3)$$

$$\frac{dx_2(t)}{dt} = -\alpha_2x_2^2 + (\alpha_1 + \alpha_3)x_1^2 \quad (4)$$

$$x_1(t_0) = 2, x_2(t_0) = 5, \alpha_1 = 1, \alpha_2 = 2, \alpha_3 = 0 \quad (5)$$

Figure 1 presents the trajectory of CM from initial time 0 to time 1.

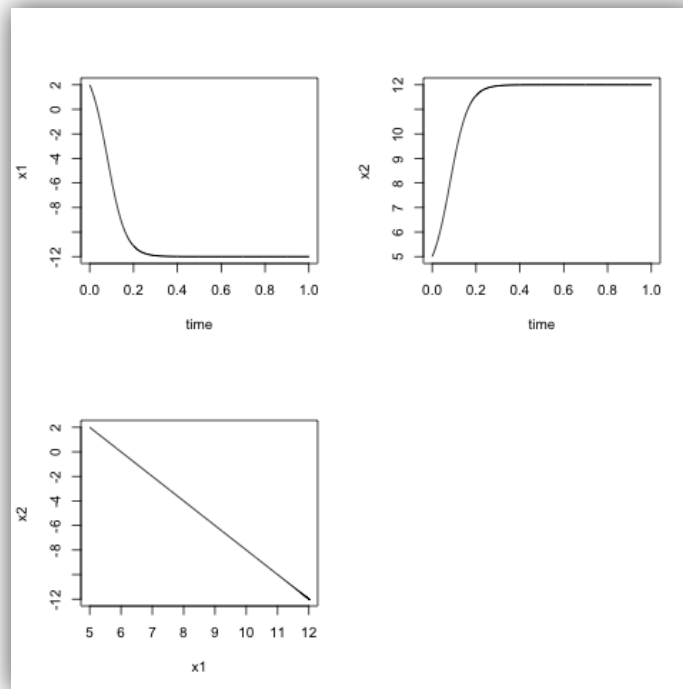


Figure 1: Trajectory of a case-model.

2.3 Sensitivity analysis

Given the ODE CM reported above, and considering that values are given to a set of parameters, it is possible to compute the dynamics of the system by numerical integration. Obviously the output of the system would depend on the parameters selected and the initial conditions, however the relation between a perturbation of a parameter (or an initial condition) and the effect of this perturbation in a given state variable needs further discussion. This analysis is defined as sensitivity analysis.

In many cases the sensitivity analysis is performed by computing the derivative of the system trajectory with respect to different parameters. Such derivatives depend on time and are called sensitivity coefficients. Local sensitivity coefficients are defined as:

$$s_{ij}(t) = \frac{\partial x_i}{\partial \alpha_j}$$

Sensitivity analysis has practical applications. On the one hand it allows the identification (and classification) of parameters that are more sensitive to perturbations; therefore also allowing the identification of model elements that need revision and refinement. On the other hand, the identification of those parameters (or initial conditions) with higher sensitivity to perturbations are targets when designing new experiments; the idea is that, by increasing the knowledge in those cases, it will allow the reduction of the uncertainty of the model and therefore it will increase of its predictive power.

High quality references for the interested reader are (Kaltenbach, Dimopoulos, and Stelling 2009), (Saltelli, Chan, and Scott 2009) and (Cacuci 2007).

2.4 Model reduction

The understanding of a model can only be achieved by the identification and dissection of its core elements. This can be achieved by finding a smaller description of the model that summarizes its relevant aspects; this process is known as model reduction.

Last years' research on model reduction has been at the forefront within the systems biology community (Albert 2003; Radulescu et al. 2008; Schmidt et al. 2008). Using *model reduction* tools, the number of degrees of freedom is reduced, while still remaining within the same model formalism as the original model. Examples of model reduction (Okino and Mavrovouniotis 1998) processes include:

- (a) **Separation of timescales:** e.g. (Klipp et al. 2005; Radulescu et al. 2008) Assuming that we consider a timescale window while neglecting faster or slower processes it is possible to reduce the number of differential equations and to replace them by algebraic equations (for instance, slow processes can be replaced by constants and fast processes can be assumed to be infinitely fast). Two steps are necessary: (1) to define the time window of reference, such as minutes, and (2) to classify processes based on their time-scale. A general mathematical consideration of time-scale separation is given in (Heinrich and Schuster 1996).
- (b) **Lumping of variables:** e.g. (Saez-Rodriguez et al. 2004; Sorensen and DeWeerth 2006). This technique reduces the complexity of a model by identifying pools of variables that can be approximated by a single lumped variable, where the internal distributions among the different sub-states are either irrelevant or assumed to occur momentarily. See (Sunnaker et al. 2010) for a recent uses within the systems biology community.
- (c) **Identifiability Analysis:** e.g. (Schmidt et al. 2008; Roper, Pia Saccomani, and Vicini 2010). This analysis addresses the following question: "*assuming known time courses for some model variables, which parameters are theoretically impossible to estimate, even with continuous, noise-free data?*" (Roper, Pia Saccomani, and Vicini 2010). Furthermore, "*the significance of this theoretical question is that the answer tells us, before the experimentally measured time-course(s) are actually gathered, what parameters would be impossible to uniquely estimate, even with perfect, noise-free data acquired continuously.*" (Roper, Pia Saccomani, and Vicini 2010).

We will not discuss in this deliverable the *transformation of modelling formalism* (such as Boolean approximations (Albert 2003; Davidich and Bornholdt 2008), as we consider these methods do not apply to the Synergy-COPD models.

In our ODE CM the Identifiability analysis would highlight that parameters α_1 and α_3 cannot be identified separately; the logical step is to consider a new parameter $\alpha_4 = \alpha_1 + \alpha_3$ and replace α_1 and α_3 appropriately in the ODE CM.

2.5 Numerical bifurcation analysis

There are mathematical properties of interest to be identified within ODE models. The most relevant is Equilibrium Points (EQ), also denoted as fixed points and within the models considered in Synergy-COPD, can be identified as steady states¹, that is, points in the state variable space where, once a trajectory reaches it, the system is fixed in time. A steady state fulfils the following property:

$$\frac{dx_i(t)}{dt} = f(t, x_1, \dots, x_n, \alpha_1, \dots, \alpha_m) = 0, \forall i = 1, \dots, n \quad (6)$$

EQ can be identified by following the trajectory of a system in time until it remains constant or by numerically solving the systems of equations shown in (3). A system can have any number of EQ (including none); EQ can be *stable* (is the system is in the EQ and is perturbed, the system will return to the EQ) or *unstable* otherwise.

Considering that (a) EQ are dependent of the parameter values and (b) the number and characteristics of EQ are “qualitative characteristics of a model”, then the modification of a parameter value p can lead to qualitative modifications in the system. The modification of a parameter value that leads to a qualitative change in the equilibrium points is called Bifurcation (BI). Some well-known examples of BI are (given a parameter p): *transcritical bifurcation* (two equilibrium points exist, one stable and one unstable, and there is a threshold value for p where equilibrium points exchange properties), *Saddle-node* (two equilibrium points collide and annihilate each other), *Hopf bifurcation* (an equilibrium point loses stability) and *Pitchfork bifurcation*. “*Limit cycle*” is a relevant property of non-linear systems; it denotes the phenomena of finding a closed trajectory within the state space that attracts all states close to it.

In the ODE CM, $x=(0,0)$ is an equilibrium point. However, in this specific example there are infinite number of equilibrium points. Moreover, **Figure 1** shows that the system has a stable equilibrium point at $x=(-12, 12)$.

Classic and new references of interest in the numerical bifurcation analysis are (Hartman 2002; Hale and Koçak 1991; Hurewicz 2002; Seydel 2010).

2.6 Code optimisation

Code optimization is understood here as the technical implementation of the numerical solutions to simulate the models. Within Synergy-COPD we consider on the one hand the stand-alone standards such as: (1) code reduction/simplification, (2) running time reduction and (3) numerical accuracy. On the other hand, we consider code-annotation and code shareability as necessary conditions within a collaborative project such as Synergy-COPD.

2.7 Status of Model Optimization in Synergy-COPD

As alluded to above, all items in **Table 1** have been completed for one of the models (M7). An extended description of the work done in this composite model is displayed in Annex 1 of the current document. Integration of mechanistic models is currently in process (see schedule in 2.10) and so are some of the items in the Table. In particular those related to M8 that will be completed when the entire integration will be achieved. In the Table, there are specific items that do not apply (NA) because of the characteristics of the model. That's the case of Model Reduction in M6.

¹ Within Synergy-COPD, any steady state achieved by a model will be a “dynamic equilibrium” (DE). In a DE the values (e.g. concentrations) of the states (e.g. molecules) do not change with time, but they imply that reactions are occurring at a fixed range.

Finally, as analysed in Subsection 2.9, Workflow on Disease Development is considered conceptually in **Table 1**. We acknowledge that Synergy-COPD will set the tools facilitating Workflow Disease Development and the project may have access to the database required for an initial approach, but we do not plan to undertake that task as part of the current project.

	Model M6	Model M7	Model M3	Model M8
Sensitivity Analysis	In process	Done	In process	In process
Model Reduction	NA	Done	In process	In process
Numerical Bifurcation Analysis	NA	Done	NA	In process
Code Optimization	Done	Done	In process	In process
Workflow on Disease Development	-	-	-	-

Table 1: Summary of Model Analysis and Refinement for each model.

2.8 Mechanistic Modelling in the project

The workflow presented in (Gomez-Cabrero, Compte, and Tegner 2011) and displayed in **Figure 2** identifies those parameters included within the mechanistic model that are abnormal and vary with the disease (COPD in the current project).

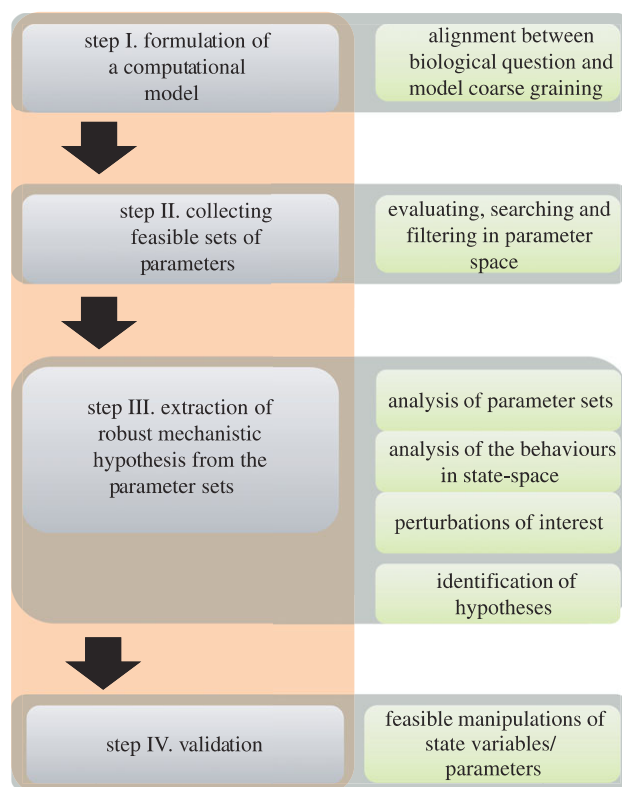


Figure 2: Workflow to analyse time-trajectories in ODE models.

The integrated model (M8) represents a relevant step beyond the state of the art of our current understanding of integrated oxygen transport, oxygen utilization and its interactions with mitochondrial ROS generation. M8 allows multilevel modelling of abnormal interactions between the steps involved in energy production.

It is of note, however, that the mechanistic approach shows intrinsic limitations to explore dimensions of the disease that can be hardly considered in a causal manner into a mechanistic model. As indicated in the Introduction and in Section 0, the interactions between mechanistic and probabilistic modelling seem to offer interesting novel tools to explore underlying mechanisms of complex diseases.

Consequently, the steps indicated in **Figure 2** should be taken more as a description of relevant generic components of mechanistic modelling than key elements for the analysis of disease mechanisms.

2.9 Targets for the Simulation Environment in Synergy-COPD

As indicated in the Executive Summary, the project has two main biological aims:

- ✓ First, identification of abnormal pathways explaining the three clinical subsets of COPD patients reported in PAC_COPD (Garcia-Aymerich et al. 2011). The project has been designed to address specifically group III including those COPD patients with moderate disease and co-morbid conditions such as cardiovascular disorders, metabolic syndrome and/or diabetes Type II.
- ✓ Second, identification of abnormal pathways shared by co-morbid conditions that are often clustered in COPD patients. This goal is somehow related with the previous one, but it will be addressed using the Medicare data base and using previous information from (Goh et al. 2007).

Expected results of the previous analyses will be validation of biomarkers useful for early identification of COPD phenotypes associated to poor prognosis because of susceptibility to systemic effects of the disease.

A completely different issue, not considered in the DoW of Synergy-COPD is the analysis of natural history of the disease or the identification of disease phenotypes associated to differences in the dynamic events of the disease progression. The ECLIPSE (Vestbo et al. 2008) study to be used in the project for validation purposes (WP7) has longitudinal information that eventually could be used for analysis of dynamic events, but the models used in the project show some limitations analysed below.

The models considered in Synergy-COPD represent steady-state conditions of the system. It allows us to observe only snap-shots at different stages of the progression of the disease. There are several limitations that deny the interpretation and modelling of the disease as a dynamic process, for instance: (1) M7 is defined under the assumption that an individual maintains a certain level of activity, so by using this model we cannot model the change of activity such as from sedentary activity to running, (2) the data from the cohort allow grouping patients, but those groups do not map to a time-progression, but to different qualitative COPD-types, therefore it is not possible to use this data to model a COPD-time-progression.

Despite those limitations there is data that can allow us to model the disease over time under certain assumptions. We use an example to illustrate this idea: let's consider model M6 and the maximum oxygen uptake by the tissues (VO_2max). From Biobridge (FP6 Life Sciences program contract 037909) data we observe in **Figure 3** that the values for VO_2max are different for the different groups of patients; this data can be compared also against the average values of a healthy individual. An average healthy male has an VO_2max between 40 and 50 ml/kg/min, (Geddes 2007) while this value in COPD patients it decrease to 15 ml/kg/min or below.

Figure 3 show two snapshots, healthy conditions to the left and COPD-patient conditions to the right. To the best of our knowledge the process of $VO_2\max$ decrease is not defined anywhere, so we make the hypothetic assumption that the decrease is linear over the time. Based on those assumptions we generate a trajectory of $VO_2\max$ values from healthy to COPD and for a set of selected points in the trajectory we compute the snapshot picture. By this process we can compute a trajectory for all state variables within M7 model; this trajectory reflects the healthy to COPD patient progression.

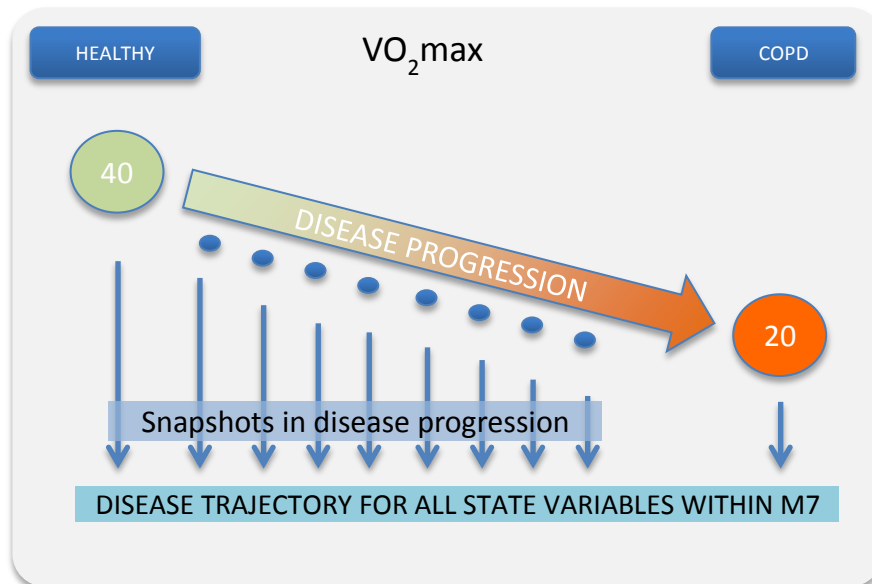


Figure 3: Construction of disease progression estimation in M6.

We can conclude that the simulation environment developed in the project may help to generate future tools to analyse the dynamic events of the disease, but limitations of the models available within the project must be taken into account. Moreover, the assessment of the disease progression is beyond the aims of the current project.

2.10 Roadmap

As indicated below, integration among all components of M8 is already solved. Briefly, M6 is fully prepared to integrate data from M3. Integration between M6 and M7 to generate M8 has been satisfactorily solved in October 2011.

Current work in process is focused on enhanced functionalities of specific aspects of M6. In particular validation of integration of lung heterogeneities within M6 and model optimization of this subset of M6 that should be finished by December 2011.

During January and February 2012 we will be completing integration of heterogeneities of peripheral gas exchange into the M6 module and we will address model optimization of M8. Moreover, specific interventions on M3 will be done and model optimization for M3 completed.

An important milestone of the project is to have an operational prototype of the entire vertical integration by early March 2012 and completed model optimization within that month.

3 Design for Synergy-COPD mechanistic models integration

3.1 Impact of spatial heterogeneities of lung ventilation and perfusion

3.1.1 Rationale

Distributions of ventilation (V) and perfusion (Q) within the lung exhibit significant heterogeneity due to the influence of branching structure, fluid properties, gravity and regional tissue forces (dependent on both posture and lung inflation level). Gas exchange efficiency is maximised by ensuring the delivery of blood is well matched to the delivery of air at the gas exchange surface (i.e. the ratio of V/Q is close to unity). This occurs naturally within a healthy lung due to both passive (similar branching structures) and active (hypoxic pulmonary vasoconstriction and/or bronchoconstriction) mechanisms. All forms of respiratory disease ultimately result in an impairment of gas exchange. This is normally a consequence of a reduction in matching between V and Q. By integrating patient-specific predictions of the regional distribution of V and Q we intend to investigate the impact of these heterogeneities – and the impact of the reduction in V/Q matching in COPD – on the amount of Oxygen (O₂) exchanged from the lungs into the blood stream. The impact of these heterogeneities within the lung will then impact on oxygen transport across each of the biological scales represented in the models in Synergy-COPD.

3.1.2 Predicting V/Q in patient-specific models derived from the PAC-COPD database

3.1.2.1 Geometric modelling

Before we can estimate functional properties we first need to generate a computational mesh that represents the geometry of the lung. There are several steps involved in this process and these are illustrated in the schematic diagram in **Figure 4**. Given CT data for a certain patient from the PAC-COPD database (Garcia-Aymerich et al. 2011) we first need to segment the images. Image segmentation refers to the process of partitioning a digital image into different segments and translating this information into a format that is easier to use. In this process we separate the lung surface and the central airways and blood vessels from the CT image. The resolution of the PAC-COPD data is relatively low (approximately 7 mm thick slices are imaged) therefore we are only able to extract the first two generations of airway and vascular branching. Details of the lung surface and central branches are then used to define a computational representation of the geometry for use in functional simulations. An estimation of the branching geometry of additional airways and blood vessels, down to the level of the acini, is generated using a computational algorithm referred to as the volume-filling branching algorithm (VFB). This method was developed by Tawhai et. al (Tawhai, Pullan, and Hunter 2000; Tawhai et al. 2004) and the structures produced using this method have been validated against morphometric studies. These branching networks terminate in approximately 30,000 acinar units. While the branching structure is only an estimate, it is still somewhat patient-specific in that the branching geometry is defined by the starting locations of the branches as well as the lung volume and shape – all defined from that patient's CT scan. This process has been applied to three subjects so far within this project (one for each COPD phenotype identified in the PAC-COPD study) and we are currently working on making this process more streamlined and efficient to enable models to be created for multiple subjects.

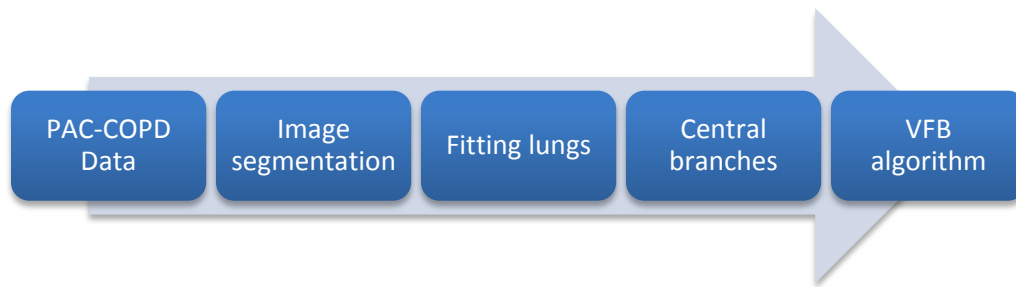


Figure 4: Schematic illustration of the processes involved in creating the anatomically-based geometric models of the lungs, airways and blood vessels.

3.1.2.2 Functional modelling

The ventilation and perfusion models determine the V and Q received by each acinar unit. These models were described in '**Deliverable 4.1: Assessment of software tools used for mechanistic modelling at each level of the body**' and will only be summarised briefly here. We have three separate functional models: **tissue mechanics, ventilation and perfusion**. To enable a realistic prediction of the distribution of ventilation and perfusion within the lung we need to incorporate the impact of several factors including:

- A realistic **branching structure** to enable more accurate predictions of the resistance to flow (achieved via the geometric modelling described above);
- **Tethering forces** being exerted on the airways, vessels and alveolar tissue (achieved by a model that predicts tissue mechanics, see details below);
- **Gravity** (included in tissue mechanics and resistance to flow equations - this causes an increase in both V and Q in the gravitationally-dependent region);
- **Other mechanisms** altering V and/or Q during disease (i.e. airway remodelling, emphysema, air trapping, hypoxic pulmonary vasoconstriction).

The ventilation and perfusion models are solved separately using geometries from the same subject with the same elastic recoil pressure (P_e) and compliance (C) distributions calculated by the tissue mechanics model. Therefore both blood and airflow through a common piece of tissue are subjected to the same local stress and strain. The tissue mechanics model is based on that by Tawhai et al. (2009) and assumes that the lung tissue is a continuum (meaning that air, airways, blood, vessels and parenchymal tissue are considered as one non-linearly elastic material). This model predicts the P_e acting on each airway and blood vessel. It also predicts the relative compliance (C) of each acinar unit which is used within the ventilation model. **Figure 5** illustrates the processes involved in the functional models, including predictions of tissue mechanics, ventilation (V) and perfusion (Q) predicted at each acinar unit. These values are then fed into the O_2 transport and utilization model with lung functional heterogeneities (described in subsection 3.2.2).

The Poiseuille resistance equations are used to represent both V and Q . Ventilation in the conducting airways is coupled to lumped representations of compliant terminal acinar units, such that the ventilation distribution is governed by local tissue density and elastic recoil pressure, airway resistance and acinar compliance. Predictions of blood flow are determined within the full pulmonary circuit (arteries, capillaries and veins) after applying pressure or flow boundary conditions on either side of the heart.

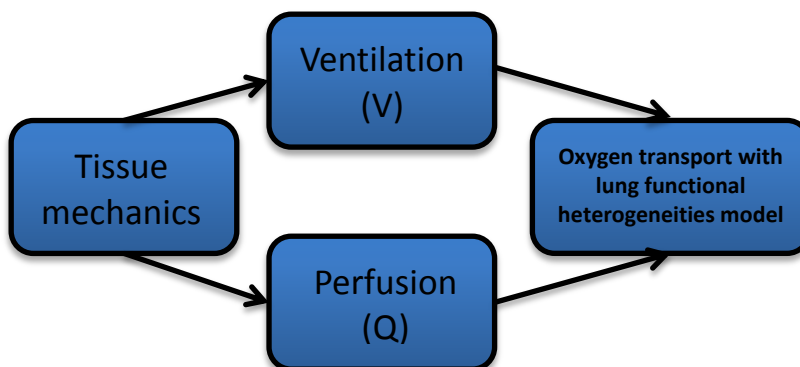


Figure 5: Illustration of the processes involved in the functional models.

Matching of ventilation and perfusion is evaluated for each acinar unit. V , Q and V/Q values throughout the lung geometry are shown in **Figure 6** where each sphere represents an acinar unit. This figure is composed of 3 images that represent predictions for (left) ventilation, V , (center) perfusion, Q and resultant V/Q values per acinus in (right) per acinus within the anatomically-based lung model. Spectrum ranges are (a) 3.2-4.5 mm^3/s , (b) 0.6-6 mm^3/s and (c) 0.5-5). The variation of these values with (gravitationally-dependent) lung height are illustrated more clearly in **Figure 7a** where we average values within 10 mm isogravitational slices. Both V and Q increase on average from apex to base. Q decreases slightly in the basal regions due to the arterial structure (longer pathways to basal regions). Higher V/Q values are evident in the lung apex compared to in the lung base, with substantial isogravitational heterogeneity. It is important to note that model predictions are for time-averaged ventilation and perfusion distributions, so air and blood flow models employ static solutions over one time interval, as opposed to dynamic solutions (changing over a breath or heartbeat). The strength of the modelling approach applied here is the detail of spatial information. V and Q are *spatial* distributions predicted within an anatomically-structured geometry that includes asymmetric branching of the airway and pulmonary vascular trees.



Figure 6: Predictions for ventilation (left), perfusion (center) and V/Q (right) per acinus within the anatomically-based lung model.

In respiratory diseases, such as COPD, additional mechanisms impact on V and Q . Ventilation is affected by airway remodelling (increasing the resistance to airflow and may lead to air trapping) and emphysema (alterations in the parenchymal mechanics and amount of surface area available for gas exchange). These alterations are being incorporated into a new model of ventilation being primarily developed within the EC project AirPROM (FP7 ref:270194). As this model develops new techniques will be incorporated into the Synergy-COPD simulations. On the vascular side, the mechanism of Hypoxic Pulmonary Vasoconstriction (HPV) induces blood vessels to constrict in areas of low alveolar oxygen thus diverting blood flow away from diseased areas. The development and integration of a mechanism for HPV is underway within the Synergy-COPD project and will be incorporated into the blood flow model used here.

3.1.2.3 Strategy for integration with the oxygen transport and utilisation with lung functional heterogeneities model

The patient-specific model described above predicts V/Q at each individual acinus, of which there are approximately 30,000 in a typical human lung. These values are equivalent to alveolar ventilation ($V_{A,i}$) and cardiac output for a compartment (Q_i) in the oxygen transport and utilisation with lung functional heterogeneities model – where a compartment is equivalent to an acinus - described in subsection 3.2.2. It is not currently feasible to incorporate this many values of V/Q into model M6 with lung functional heterogeneities. **Figure 7** illustrates the distribution of V , Q and V/Q (left hand side) over the height of the lung (values are averaged within 10 mm isogravitational slices) and the log-normal distribution of V/Q values incorporating all 30,000 acinar values (right hand side). The best method is to produce a presentation of the V/Q log-normal distribution of these values within the full lung model and interpolate these values for a given number of compartments (n). These compartmental values will then be integrated into model M6 with lung functional heterogeneities.

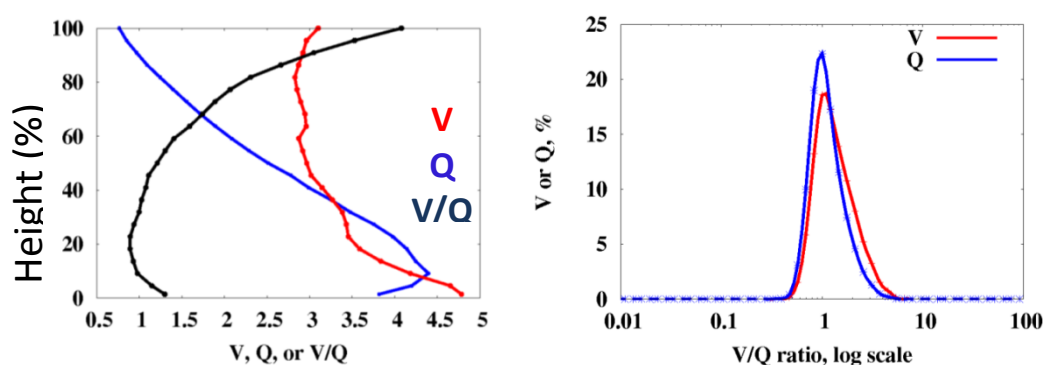


Figure 7: Distribution of V , Q and V/Q over the height of the lung (left) and the log-normal distribution of V/Q values incorporating all 30,000 acinar values (right).

The entire process is summarised here:

- 1) Generate patient-specific model geometries based on PAC-COPD CT image data;
- 2) Predict tissue mechanics – this provides predictions of stresses and strains acting on airways and vessels;
- 3) Predict the distribution of alveolar ventilation (V_A) at each acinus;
- 4) Predict the distribution of blood flow (Q) at each acinus;
- 5) Produce a log-normal curve of V/Q values and interpolate for n compartments (V_{A_i}/Q_i) to be passed to model M6 with lung functional heterogeneities.

3.2 Lung functional heterogeneities

3.2.1 Rationale

The heterogeneities of the ventilation-perfusion (V_A/Q) ratios within the lung are the major factor causing alterations of respiratory blood gases (hypoxemia & hypercapnia) in different disease conditions. During the last few months, lung functional heterogeneities have been introduced in the model previously reported in D4.1, as described in detail below. Accordingly, an enhanced M6 with an enriched description of pulmonary gas exchange is now ready to be further integrated into M8.

The new version of M6 facilitates integration of information from M3 into the current model. Moreover, the current setting will allow to use for the purposes of the project, the available clinical research

information on lung functional heterogeneities that has been collected in COPD patients over the last 30 years (Rodríguez-Roisín et al. 2009) using the multiple inert gas elimination technique (MIGET) (Roca and Wagner 1993).

3.2.2 Incorporating lung functional heterogeneities to the oxygen transport and utilization model M6

Model M6 (Oxygen transport and utilization) considers the Oxygen (O_2) transport and utilisation pathway as an integrated system in order to predict O_2 transport from air to mitochondria, and then couples this to O_2 utilisation by the mitochondria. The physical concept is illustrated in **Figure 8**: ventilation to bring O_2 from environmental air to the alveolar gas, diffusion of O_2 from alveolar gas into pulmonary capillary blood, circulation transport of O_2 from lungs to tissue (muscle) micro-vessels and diffusion of O_2 from tissue micro-vessels to mitochondria. In this Figure, \dot{V}_A stands for Alveolar Ventilation, $P_{I_{O_2}}$ stands for Inspired Partial pressure of Oxygen, $P_{A_{O_2}}$ is the Alveolar Partial pressure of Oxygen, D_L and D_M stand for Lung and tissue (Muscle) diffusing capacity, $P_{a_{O_2}}$ and $P_{v_{O_2}}$ are the arterial and venous Partial pressure of Oxygen, \dot{Q}_T is the Total cardiac output, \dot{V}_{O_2MAX} is the maximum Oxygen uptake by the tissues, P_{50} is the oxygen partial pressure at which respiratory flux is half maximum (\dot{V}_{O_2MAX}) and $P_{MITO_{O_2}}$ is the mitochondrial partial pressure of oxygen.

Broadly speaking, given the transport capacity of the lungs, heart, blood and muscles (characterised by numerical values for the major transport variables), model M6 computes how much O_2 can be supplied to the tissues, and what are the partial pressure of oxygen (P_{O_2}) values at each step of the oxygen transport and utilization pathway. For a more detailed description of the model see **Deliverable 4.1: Assessment of software tools used for mechanistic modelling at each level of the body**.

There are some important assumptions/approximations in Model M6:

- O_2 transport is in **steady state** so all input and output variables are constant in time.
- The **lungs** are assumed to be **homogeneous** (main reason for this section).
- The **tissues** are likewise assumed to be **homogeneous**.

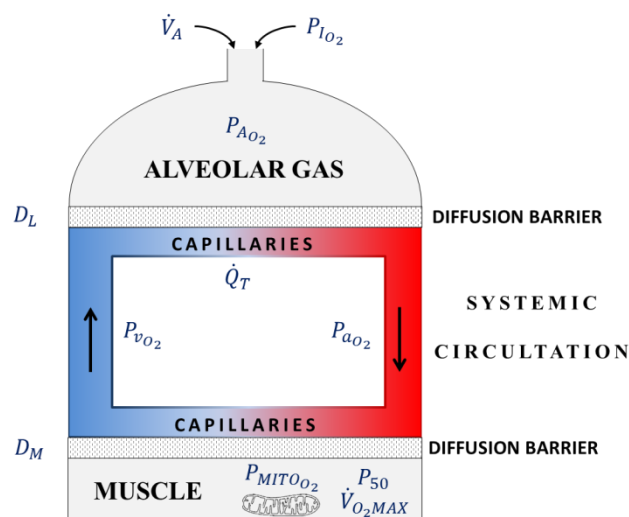


Figure 8: Schematic description of the main components of the Oxygen transport and utilisation model (M6).

In order to incorporate lung functional heterogeneities to the oxygen transport and utilization model three basic steps need to be accomplished:

- Provide a validated lung functional heterogeneities model.
- Make both model M6 and the lung functional heterogeneities models' source code modular-programming compliant.

- Integrate model M6 and the lung functional heterogeneities model in a single model for the oxygen transport and utilisation with lung functional heterogeneities and validate it.

Model M6 is implemented as a computing program written in one of the earlier versions of IBM mathematical FORMula TRANslating system 77 (FORTRAN 77). FORTRAN is a general-purpose, procedural, imperative programming language that is especially suited to numeric computation and scientific computing. As any modern imperative programming language, FORTRAN 77 supports modular programming, which allows representing a separation of concerns, and improving maintainability by enforcing logical boundaries between interchangeable components called modules. Accordingly, model M6 is composed of several modules called subroutines that perform specific tasks within the whole program and are relatively independent of the remaining code.

Specifically, model M6 make use of two principal subroutines to compute oxygen diffusion from lung to artery (LT0) and oxygen diffusion from artery to tissue (LT1). This feature makes M6 ready for integration with the lung functional heterogeneities model and the linking point is to “replace” model M6 subroutine LT0 with the lung functional heterogeneities model. **Algorithm 1** shows a simplified pseudocode for M6 implementation.

Algorithm 1: Oxygen transport and utilisation

Data: $P_{I_{O_2}}, \dot{V}_A, D_L, \dot{Q}_T, D_M, \dot{V}_{O_2MAX}, P_{50}$

Result: $P_{A_{O_2}}, P_{MITO_{O_2}}, P_{a_{O_2}}, P_{v_{O_2}}, \dot{V}_{O_2}$

```

1 begin
2   Input data entry
3   While ( $P_{MITO_{O_2}} \neq \dot{V}_{O_2}$ ) do
4     LT0 computes  $P_{a_{O_2}}$  depending on  $P_{v_{O_2}}, P_{A_{O_2}}$  and  $D_L$ 
5     LT1 computes  $P_{v_{O_2}}$  depending on  $P_{a_{O_2}}, P_{MITO_{O_2}}$  and  $D_M$ 
6   Compute  $\dot{V}_{O_2}$ 

```

Lung functional heterogeneities model has been developed by Prof. Peter D Wagner to compute the effects of \dot{V}_A/\dot{Q}_T mismatch and diffusion limitation on gas exchange. So that, lung heterogeneity is simulated using a compartmental definition of the lung. Each lung compartment (*compartment_i*: $i = 2..n$) have their own \dot{V}_A/\dot{Q}_T mode. Specifically, *compartment_i* is defined by having specific alveolar ventilation \dot{V}_{A_i} , alveolar partial pressure of oxygen $P_{A_{iO_2}}$, lung diffusing capacity D_{L_i} and cardiac output \dot{Q}_i . Hence, total lung alveolar ventilation \dot{V}_A , partial pressure of oxygen $P_{A_{O_2}}$, diffusing capacity D_L and total cardiac output \dot{Q}_T is computed as follows:

$$\dot{V}_A = \sum_{i=1}^n \dot{V}_{A_i}$$

$$P_{A_{O_2}} = \frac{\sum_{i=1}^n P_{A_{iO_2}} \times \dot{V}_{A_i}}{\sum_{i=1}^n \dot{V}_{A_i}}$$

$$D_L = \sum_{i=1}^n D_{L_i}$$

$$\dot{Q}_T = \sum_{i=1}^n \dot{Q}_i$$

The overall output of the lung functional heterogeneities model are the arterial concentration of oxygen C_{aO_2} , which is computed as a weighted mean of the compartmental endcapillary concentration of oxygen $C_{ec_{iO_2}}$, and the corresponding arterial partial pressure of oxygen P_{aO_2} by means of the oxygen–haemoglobin dissociation curve:

$$C_{aO_2} = \frac{\sum_{i=1}^n C_{ec_{iO_2}} \times \dot{Q}_i}{\sum_{i=1}^n \dot{Q}_i}$$

With respect to lung heterogeneity related parameters, currently there are two data entry options. On the one hand, compartmental specifics can be manually entered by specifying the total number of lung compartments (n) as well as individual compartmental characteristics (i.e. \dot{V}_{A_i} , $P_{A_{iO_2}}$, D_{L_i} and \dot{Q}_i : $i = 2..n$). On the other hand, compartmental specifics can be entered as a \dot{V}_A/\dot{Q}_T log-normal distribution, most suitable for the simulation of a large number of compartments and for incorporating model M3 output as stated in subsection 3.1.2.3.

In order to integrate model M6 with the lung functional heterogeneities model, the latter have to be encoded as a FORTRAN subroutine (from the lung functional heterogeneities standalone FORTRAN program) so that it will replace LT0 subroutine of model M6 for computing oxygen diffusion from lung to artery. Then, shared common variables and modules between both models must be merged in a single FORTRAN main program. Finally, the integrated model for oxygen transport and utilisation with lung functional heterogeneities will be created as stated in **Figure 9**. In this figure \dot{V}_{A_i} stands for compartmental alveolar ventilation, $P_{A_{iO_2}}$ is the compartmental alveolar partial pressure of oxygen, D_{L_i} is the compartmental diffusing capacity, \dot{Q}_i is the compartmental cardiac output, $C_{ec_{iO_2}}$ stands for compartmental endcapillary concentration of oxygen and C_{aO_2} is the arterial concentration of oxygen. Other parameters stand the same as in **Figure 8**. The simplified pseudocode for the integrated model implementation is presented in **Algorithm 2**.

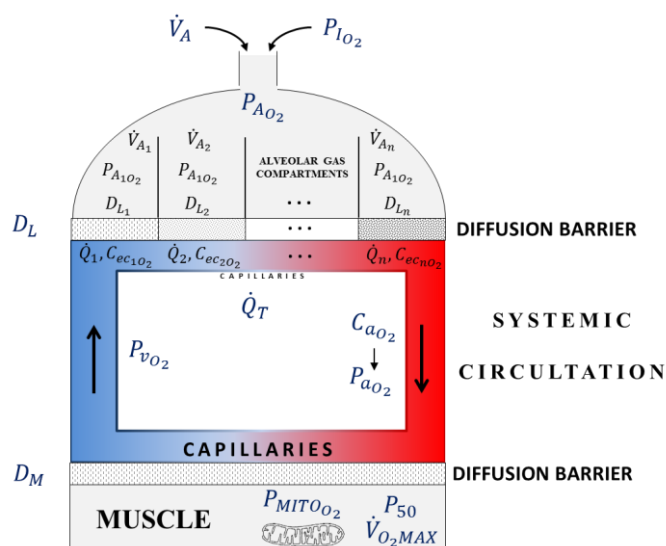


Figure 9: Schematic description of the main components of the oxygen transport and utilisation considering lung functional heterogeneities.

Currently, the oxygen transport and utilisation with lung functional heterogeneities model implementation is accomplished and model validation is under way.

Algorithm 2: Oxygen transport and utilisation with lung functional heterogeneities

Data: $P_{I_{O_2}}, \dot{V}_{A_i}, D_{L_i}, \dot{Q}_i, D_M, \dot{V}_{O_2MAX}, P_{50}$

Result: $P_{A_{iO_2}}, P_{MITO_{O_2}}, P_{a_{O_2}}, P_{v_{O_2}}, \dot{V}_{O_2}$

```

1  begin
2  |   Input data entry
3  |   While ( $P_{MITO_{O_2}} \neq \dot{V}_{O_2}$ ) do
4  |   |   M8 computes  $P_{a_{O_2}}$  depending on  $P_{v_{O_2}}, P_{A_{iO_2}}$  and  $D_{L_i}$ 
5  |   |   LT1 computes  $P_{v_{O_2}}$  depending on  $P_{a_{O_2}}, P_{MITO_{O_2}}$  and  $D_M$ 
6  |   |   Compute  $\dot{V}_{O_2}$ 

```

3.3 Functional heterogeneities of peripheral gas exchange

3.3.1 Rationale

The skeletal muscles, similar to the lungs, are subject to a corresponding set of oxygen exchange limitations, namely: a) oxygen uptake-blood flow (VO_2/Q) ratios inequality, b) limitation of diffusive transport of oxygen from the muscle microcirculation to the mitochondria, c) shunting of blood flow through non-nutrient vessels, and d) diminished total blood flow. Many studies have indirectly suggested that, contrary to most circumstances in the lungs, diffusion limitation is the principal mechanism of oxygen unloading limitation, even in healthy controls (Gayeski and Honig 1988; Hogan, Bebout, and Wagner 1991; Honig et al. 1991; Richardson et al. 2001). However, the contribution of VO_2/Q heterogeneities has been largely obscure for lack of direct methods for its measurement. During the next three months, we will enhance M6 addressing: a) heterogeneities (VO_2/Q ratios) of skeletal muscle gas exchange, b) heterogeneities of peripheral gas exchange in territories other than skeletal muscle, and, c) regional heterogeneities.

3.3.2 Incorporating peripheral functional heterogeneities to the oxygen transport and utilization model M6

The task is in process. A similar approach to functional heterogeneities of lung gas exchange has been done. It should be finished by March 2012 in order to proceed to full integration of the final M6 model into M8.

3.4 Integration among O_2 transport, central metabolism and ROS generation

3.4.1 Rationale

Prevalent chronic diseases, such as Chronic Obstructive Pulmonary Disease (COPD) are associated with significant systemic alterations. Since the function, which is primarily affected in COPD, is oxygen diffusive capacity of the lung, it has long been proposed that the inability to sustain a high level of ventilation was the main factor inducing various systemic alterations (Bye, Farkas, and Roussos 1983). Given this, all the systemic effects, developed with the progression of the disease, must be mediated by oxygen deficiency as a primary defect. However, the details of the underlying mechanism of the systemic effects of oxygen deficiency are not understood. It is known that oxidative stress in respiratory (Klimathianaki, Vaporidi, and Georgopoulos 2011) and skeletal muscles (Roche et al. 2011; Abdellaoui et al. 2011; Barreiro et al. 2010) is one of the hallmarks of systemic effects of COPD. Oxidative stress in COPD is characterized by the increased levels of oxidation, nitration and carbonylation of proteins as a

result of increased production of Reactive Oxygen Species (ROS) in mitochondrial electron transport chain. The electron transport chain links the central carbohydrate energy metabolism with ATP synthesis. It transforms the free energy, released in the oxidation of NADH and succinate, into the form of transmembrane electrochemical potential ($\Delta\Psi$), which is used for ATP synthesis (Mitchell 1961). Reactive oxygen species (ROS) are byproducts of electron transport (Turrens, Alexandre, and Lehninger 1985) that play roles of metabolic signals and destructive agents (Li and Jackson 2002; Bottino et al. 2004; Guzy et al. 2005; Cai and Jones 1999; Griffiths et al. 2011; Gupta et al. 2011). The defects in oxygen supply thus can affect both important functions of mitochondria: ATP synthesis and ROS production, and the investigation of the respiratory chain operation and the effects of oxygen depletion are necessary to understand the mechanisms of pathology in COPD.

The electron transport reactions are strictly organized in space and functionally. To understand their complex organization and the properties that follow from this organization, a detailed mathematical model that implements the known details of electron transport is indispensable. We started such modelling from complex III of respiratory chain, where the Q-cycle mechanism of electron transport is investigated in most detail (Selivanov et al. 2009). The applied rule-based algorithms constructed a 400-equation model describing dynamics of all possible redox states of the model. This detailed model allowed revealing multiple steady states at the same values of parameters. The revealed phenomenon can be a basis for multiple modes of ROS production observed in the same conditions, for instance, before and after passing through hypoxia and then return to the normal oxygenation.

Then in the framework of Synergy-COPD we extended the model to the whole respiratory chain and reactions of TCA cycle supplying substrates for respiration (Selivanov et al. 2011). The set of parameters for this model (described in **Deliverable 4.1 (D4.1): Assessment of software tools used for mechanistic modelling at each level of the body**) was restricted by model behaviour consistent with the measured data, such as maximal respiration rate and ROS production in a suspension of mitochondria respiring on succinate or pyruvate and malate, and also the dynamics of NAD^+ reduction to NADH in the presence of succinate as a substrate, and with or without addition of rotenone. This extended model confirmed the existence of multiple steady states in the range of parameters that are consistent with the measured experimental data.

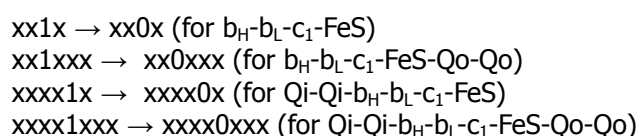
Here we describe the next step to make a model useful for clinical predictions. Specifically, the model of mitochondrial respiration, which describes TCA cycle dependent electron flow reducing molecular oxygen and free radical formation contributing to ROS production, with the model of oxygen transport from lung to tissue in its complete form. This integration gives access to the clinical data and allows prediction the rate of ROS production for various oxygen supply restricted by the disease conditions.

With regards to the link between mitochondrial respiration and TCA cycle, we implemented a new tool for model discrimination analysis, which gives more possibilities in refining the model of central metabolism. This tool allows comparing models, implementing various metabolic schemes, by their capacity to reproduce experimental data and reject schemes not consistent with experimental data. Specifically, this tool allowed to reveal the compartmental structure of intracellular metabolism in the upper glycolysis (Marin de Mas et al. 2011).

3.4.2 Oxygen consumption described in the model of mitochondrial respiration

A detailed model of respiratory chain developed in the framework of Synergy-COPD is described elsewhere (Selivanov et al. 2011) and is presented in **Annex 2**.

The net electron flow from cytochrome *c1* to *c* is then delivered to oxygen and therefore it can be considered as a flux of oxygen consumption. The reactions contributing to the net flux of oxygen in the algorithmic form used in the model can be written as follows:



Here “x” designates any of the symbols “0” or “1”. Symbol “1” situated in the place of cytochrome c1 indicates that c1 is reduced, and symbol “0” indicates that it is oxidized.

To calculate the total rate of electron flow to oxygen (V_{O_2}) the algorithm sums the parts of this flow computed for each of the redox states containing reduced c1. The individual rates for participating redox states (e.g. v_{xx1x} for the core states $xx1x$ with concentrations C_{xx1x}) are computed as follows:

$$V_{xx1x} = k_{O_2} \cdot C_{xx1x} \cdot O_2 / (O_2 + K_m) \quad (7)$$

Here O_2 is a fraction of dissolved oxygen with respect to its content at equilibrium with atmospheric oxygen at normal pressure, k is reaction rate constant, K_m is Michaelis constant for interaction with oxygen. These parameters were adjusted so that the model describes limitation of electron flow by oxygen, which was found experimentally.

3.4.3 Oxygen transport from lung to tissues

The main principles of this model were described in **D4.1**. It is possible to solve analytically the equations of this model using the simplifications of hemoglobin saturation curve. However, numerical solution of the model equations allows using more precise, experimentally measured, hemoglobin saturation curve and its change with the change of pH and temperature. The numerical algorithm is as follows:

Step 0. Guessing an initial value for venous partial pressure of O_2 and CO_2 , and calculation of corresponding concentrations using hemoglobin saturation curve.

Step 1. Solving numerically two differential equation describing the change of concentration (C) in the process of saturation with O_2 and release of carbon dioxide (CO_2) for a portion of blood during the time of passing through the lung capillary:

$$\frac{dC_{O_2}}{dt} = k_{AO_2} \cdot (P_{AO_2} - P(C_{O_2})) \quad (8)$$

$$\frac{dC_{CO_2}}{dt} = k_{ACO_2} \cdot (P_{ACO_2} - P(C_{CO_2})) \quad (9)$$

Here symbol P designates partial pressure of O_2 or CO_2 in the lung capillary or alveoli (P_A). It is supposed to be constant in alveoli and function of concentration in capillary. This function is defined by measured hemoglobin saturation at various partial pressures, and empirical dependence on pH and temperature. Symbol k designates the constant of diffusion in alveoli.

Starting from the initial values for venous partial pressure and concentrations, numerical solution gives final pressure and concentrations acquired by the considered portion of blood after passing through lung. These final values correspond to the concentrations and pressure in arterial blood.

Step 2. Solving numerically two differential equation describing the change of concentration in the process of O_2 delivery to tissues and uptake of CO_2 for a portion of blood during the time of passing through the tissue capillary:

$$\frac{dC_{O_2}}{dt} = k_{TO_2} \cdot (P_{TO_2} - P(C_{O_2})) \quad (10)$$

$$\frac{dC_{CO_2}}{dt} = k_{TCO_2} \cdot (P_{TCO_2} - P(C_{CO_2})) \quad (11)$$

Here symbol P designates partial pressure of O_2 or CO_2 in the tissue capillary or inside the cells (P_T). It is supposed to be constant in cells and function of concentration in capillary. This function is the same

as in **step 1**. Symbol **k** designates the constant of diffusion in tissue. Starting from the initial values for arterial partial pressure obtained as a result of **step 1**, numerical solution gives final pressure and concentrations acquired by the considered portion of blood after passing through tissue capillary. These values correspond to the concentrations and pressure in venous blood.

Step 3. Taking the new values for venous blood go to **step 1** and recalculate arterial pressure and concentrations, then with new values for arterial blood pass to **step 2** and then to **step 3** again.

The cycle step 1-2-3 repeats until the computed values for venous and arterial blood do not change. These values correspond to the steady state for a given set of parameters (described in Deliverable 4.1). Then the rate of oxygen transport (V_{O_2}) is calculated as a function of blood flow rate (V_{BL}) and difference between arterial and venous O_2 concentrations:

$$V_{O_2} = V_{BL} \cdot (C_{O_{2a}} - C_{O_{2v}}) \quad (12)$$

3.4.4 Linking the models of mitochondrial respiration and oxygen transport

In the model of oxygen transport, atmospheric and tissue levels of O_2 are considered to be constant. Given the parameters of ventilation in lungs, O_2 diffusion in lungs and tissues, and blood flow, the atmospheric and tissue O_2 concentrations define O_2 levels in arteries and veins and, consequently, corresponding VO_2 value. The tissue oxygen levels vary depending on the intensity of work performed by cells. This cellular work requires restoring the consumed energy, in a great part, through oxidative phosphorylation, which is stoichiometrically linked with oxygen consumption. In accordance with equation (10), the more oxygen needs to be consumed, the lower tissue levels of oxygen have to be established. On the one hand, if the tissue oxygen levels are already close to zero, they can restrict further increase of work intensity. Thus, tissue oxygen levels depend on, and at the same time, define the intensity of work performed by cells. On the other hand, tissue oxygen levels depend on and define the rate of oxygen transport. Thus, tissue oxygen levels represent a variable linking the model of oxygen transport with the model of mitochondrial respiration. The levels of tissue oxygen, the same for the both models, must correspond to the consumption rate in respiration the same as transport rate from lung. This is the main principle defining models linkage.

There are various ways of linking the two models keeping the same main principle. Specifically, one of such ways, using analytical solution of O_2 transport, was described in **Deliverable 4.1**. Here the link of models in their most complete form, keeping the modularity of the integrated model, is described:

3.4.4.1 Compatibility of the code

The model of mitochondrial respiration is written in C++ whereas the model of O_2 transport is written in FORTRAN. Functions written in FORTRAN can be called from C++ code, thus linking the model does not require essential change of the code. The main program of O_2 transport model was presented as a subroutine taking oxygen partial pressure in tissue ($P_{T_{O_2}}$) as input parameter and oxygen transport (V_{O_2}), from eq. (12) as output parameter. Then, without any other change in the original code, for the same tissue O_2 the program can call the model of respiration and get O_2 consumption rate, and call the model of O_2 transport and get O_2 transport rate. At this level, we implemented *iterative procedure* that finds the tissue O_2 levels that corresponds to the same rate of oxygen transport and consumption.

- **Step 0.** Take some guessed tissue O_2 partial pressure.
- **Step 1.** Using the taken O_2 levels run the model of mitochondrial respiration and to obtain O_2 consumption $V_{O_{2c}}$. This value depends on many parameters and it can be limited or not limited by the given O_2 levels.
- **Step 2.** To run the model of O_2 transport for the same guessed O_2 levels and to obtain the O_2 transport $V_{O_{2t}}$.
- **Step 3.** To compare the obtained $V_{O_{2c}}$ and $V_{O_{2t}}$. If $V_{O_{2c}} > V_{O_{2t}}$ then to decrease the guessed O_2 levels, in the opposite case to increase the guessed O_2 levels. Come back to the step 1 and

repeat the whole procedure. Stop, when the difference between $V_{O_{2c}}$ and $V_{O_{2t}}$ is less than some assumed threshold.

This algorithm defines tissue O_2 levels that correspond to the same O_2 consumption and delivery. The model of O_2 transport gives corresponding values of oxygen levels in arteries and veins. The O_2 consumption and O_2 levels are clinically measured values; they can be fitted and the corresponding mitochondrial respiratory state and ROS production, and the state of central metabolism can be evaluated from the simulation of the model of respiration.

3.4.4.2 Correspondence of units between the two models

Since the tissue O_2 levels are considered a constant that corresponds to steady state when the consumption equals to delivery it can be expressed in any units without adjusting to the other units of the model of mitochondrial respiration, provided that K_m in eq. (7) is expressed in the same units. It is convenient to express it in mmHg, the same units as in the model of oxygen transport. K_m in eq. (7) was set as 1 mmHg, or ~1% of saturated O_2 concentration.

$V_{O_{2c}}$ is expressed in nmol/min/(mg of mitochondrial protein), whereas $V_{O_{2t}}$ in the current version of the model of O_2 transport is expressed as mL/min. To make the units consistent the both values are transformed to mL/min/(kg of working muscle) in accordance with the transformation of units:

- 1 g of muscle tissue contains 53 mg of mitochondrial protein (Vinnakota and Bassingthwaighte 2004).
- 1 mol of gas occupies 22.4 L.
- 1nmol/min/(mg of mitochondrial protein)= 53 nmol/min/(g of tissue)=53 μ mol/min/kg =53·22.4 μ L/min/kg=1187.2 μ L/min/kg ~1.2mL/min/kg.

Oxygen consumption measured for the whole body can be recalculated for 1 kg of exercising muscle taking into account the difference of consumption at rest and exercise, and the total mass of exercising muscle.

3.4.4.3 Link between the model of central metabolism and respiration

Electrons transported by the respiratory chain to oxygen are taken from succinate or/and NADH as substrates, which are products of central carbohydrate metabolism (glycolysis, TCA cycle). The reactions of TCA cycle are included in the integrated model as follows. The expressions for some of the reaction rates lump several reactions together and account phenomenological for the substrates rather than real reaction mechanisms.

Succinate dehydrogenase:

$$V_{SDH} = \frac{V_{m_{SDH}} \cdot Q \cdot suc}{(K_{m_Q} + Q) \cdot (K_{m_{suc}} + suc)} \quad (13)$$

The fumarate oxidation and malate dehydrogenase (MDH) reactions forming oxaloacetate (oa) assume that fumarate and malate represented as a single pool (mal):

$$V_{MDH} = k_{MDH} \cdot (NAD \cdot mal - NADH \cdot oa) \quad (14)$$

The citrate synthase reaction assumes that pyruvate and acetyl CoA are combined in a single pool (pyr):

$$V_{CS} = k_{CS} \cdot pyr \cdot oa \quad (15)$$

Transport of pyruvate assumes a constant cytosolic concentration (C_{pyr}) and a variable mitochondrial concentration (pyr):

$$V_{pyr} = k_{pyr} \cdot (C_{pyr} - pyr)$$

(16)

A number of TCA cycle reactions from citrate (cit) to succinate are combined. The whole set depends on citrate as input substrate and NAD^+ :

$$V_{TCA} = k_{TCA} \cdot NAD \cdot cit \quad (17)$$

Succinate exchange to fumarate/malate assumes constant external concentrations (C_{suc} , C_{mal}):

$$V_{sm} = k_{sm} \cdot (C_{suc} \cdot mal - C_{mal} \cdot suc) \quad (18)$$

Succinate entry when it is added externally is modelled by:

$$V_{suc} = k_{suc} \cdot (C_{suc} - suc) \quad (19)$$

Malic enzyme transforms malate into pyruvate:

$$V_{ME} = k_{ME} \cdot NAD \cdot mal \quad (20)$$

The parameter values for the reactions listed above are shown in **Table 3**.

Dynamics of the new variables (suc, mal, oa, pyr, cit) are described by following ODEs incorporated in the model:

$$\frac{d(suc)}{dt} = V_{TCA} - V_{SDH} + V_{sm} + V_{suc} \quad (21)$$

$$\frac{d(mal)}{dt} = V_{SDH} - V_{ME} - V_{MDH} \quad (22)$$

$$\frac{d(oa)}{dt} = V_{MDH} - V_{CS} \quad (23)$$

$$\frac{d(cit)}{dt} = V_{CS} - V_{TCA} \quad (24)$$

$$\frac{d(pyr)}{dt} = V_{pyr} + V_{ME} - V_{CS} \quad (25)$$

The dynamics of NAD^+ are now described as follows

$$\frac{d(NAD)}{dt} = V_{cl} - 3 \cdot V_{TCA} - V_{ME} - V_{MDH} \quad (26)$$

Here V_{cl} is the reaction of NADH oxidation by complex I. The TCA cycle reactions from citrate to succinate reduce two molecules of NAD^+ for each succinate produced, but the model also accounts for

a molecule of NADH produced by transformation of pyruvate into acetyl CoA, which is not included explicitly.

3.4.4.4 Implementation of a new complementary tool for the analysis of compartmental structure and metabolic fluxes in central carbohydrate metabolism

The fluxes in central carbohydrate metabolism affect mitochondrial respiration, oxygen consumption and ROS production. Their analysis is complicated by the fact that the metabolites can be intricately separated and organized in sub-compartments as a result of metabolic channelling. In the framework of this technological project we developed software as a general tool for investigation the compartmental structure of central carbohydrate metabolism. This tool can be applied for the analysis of compartmental structure and evaluation of metabolic fluxes in central carbohydrate metabolism in various types of living cells under various conditions. The description of this tool is presented in our recent accepted publication in BMC Systems Biology 2011 (Marin de Mas et al. 2011).

The model that takes into account the compartmental structure of central metabolic pathways, revealed using this software tool, can be linked with the model of mitochondrial respiration, thus extending the current version of the model of central metabolism.

Plan for further development of the integrated model:

- **Technology.**

In the model of mitochondrial respiration include detailed description of cytochrome c reduction by cytochrome c1 and oxidation by complex IV, and reactions performed by complex IV. In the model of central metabolism introduce more complete set of reactions of glycolysis, TCA cycle, pentose phosphate pathway, specifically those related with decarboxylation. In the integrated model make a link between CO₂ release in lung and production in central metabolism.

- **Application.**

Start analysis of clinical data on gas exchange and lactate in blood refine the integrated model to customize it for the particular data analysis (make convenient interface, supplement with algorithms for the particular data fitting, statistical analysis, etc.).

4 Interactions between: mechanistic models, “de novo” probabilistic models and CDSS

4.1 Introduction

In **Deliverable 5.1** (D5.1), “**Horizontal integration: Strategies for connecting mechanistic and probabilistic modelling**”, we proposed a first general approach to integrate mechanistic and probabilistic models into the Synergy-COPD simulation environment. This approach is extended and further detailed in the current document.

This section describes the stepwise strategy used in the project to build-up the Cross-Talk between Mechanistic and Probabilistic modelling (CTMP) aiming at generating the simulation environment that should facilitate achievement of the two main objectives of the project, as described in Section 1 of the current document.

CTMP can only be detailed if the different elements and the goals (considering goals as the grouping of major and minor objectives) are first described. The present section aims at setting the goals, the long-term working schedules, the methodological framework and the detailed description of the initial tasks that can be defined at the present stage.

Subsection 4.2 details the bio-entities and the models we are considering. This subsection does not provide any specific biological output, but specifies three key aspects (i.e. bio-entities, models and their interaction) in such a way that define and allows their use within Synergy-COPD.

Once the basis is defined, Subsection 4.3 details the long-term perspective of the integration. The simulation environment, the CDSS and the different elements and concepts described in Subsection 4.2 are observed in an integrated manner in order to answer specific biological questions. Each biological question is planned under a certain schedule where different objectives and deadlines are settled. The three biological questions under consideration are:

- ✓ **Phase I:** Mechanistic and probabilistic study of ROS levels pre- and post-training in Biobridge , an integrated approach.
- ✓ **Phase II:** Differences in metabolic pathways between Group I and Group III from PAC-COPD study (Garcia-Aymerich et al. 2011).
- ✓ **Phase III:** Co-morbidity study in COPD patients based on Medicare database and PAC-COPD study.

Specifically, Subsection 4.3 refers to specific actions that are described in larger detailed in Subsection 4.4.

4.2 Data, models and interactions: concepts and definitions

Synergy-COPD combines the effort of groups from very different backgrounds. The interaction of such heterogeneous groups provides a unique strength, but it also uncovers certain challenges. One challenge is the definition of a shared terminology; that makes this sub-section necessary.

Furthermore, the sources of bio-entities we work with are also very heterogeneous; therefore, their usefulness from the bio-researcher or from the clinician point of view is different. To clarify this part, we enumerate and describe the different data types in this aspect.

Finally all the bio-entities and models are integrated within the simulation environment; therefore we need to define the underlying structure, even if in this subsection it is only graphically.

4.2.1 Data

Data within Synergy-COPD is obtained from various sources; therefore we are considering a large heterogeneous data set. We denote the data types considered as bio-entities. Some examples of bio-entities are physiological measures such as VO_2 max (Wagner 1996), genome wide profiling such as expression arrays (Turan et al. 2011), and patient classification (as the classification provided in PAC-COPD). Therefore an initial and necessary classification of the bio-entities is their qualitative (nominal or ordinal) or quantitative properties.

However other types of characteristics are needed to be defined such as (1) their existence in data sets, (2) if they are mathematically deducible or (3) their clinical relevance. A first step is then to provide a detailed enumeration and classification of the bio-entities within Synergy-COPD.

The data can be classified by their source:

- ✓ Biobridge (FP6 Life Sciences program contract 037909).
- ✓ Data from public repositories (such as expression arrays data-sets of interest) .
- ✓ PAC-COPD (Garcia-Aymerich et al. 2011).
- ✓ Eclipse-GSK (Vestbo et al. 2008).
- ✓ Medicare (Lee et al. 2008).

First the bio-entities overlapping more than one source need to be characterized. Secondly, the unit of each entity in each source and the possibility of comparison between sources need to be described.

Previously enumerated sources are described elsewhere (see, for instance, Deliverable 5.1), however we propose to review all the sources in order to classify bio-entities by the following characterization:

a. **Observable Bio/Physiological Entities (OBPE):**

- i. **Definition:** bio-entities that can be measured.
- ii. **Types:** we observe two subtypes: **OBPE1** denotes the observable entities that are currently measured in the clinical environment (such as some protein concentrations). **OBPE2** denotes those entities that are not used for diagnosis; for instance transcriptomic array expression.
- iii. **Usage:** OBPE are used to deduce other bio-entities' measures and/or predict unobservable (possibly clinical) entities.
- iv. **Examples:** for OBPE1, protein concentrations, inspired PO_2 and CT scan image. For OBPE2 the transcriptional profiling of Interleukin 2.

b. **Deducible Bio/Physiological Entities (DBPE):**

- i. **Definition:** bio-entities that are not usually measured but can be deduced by the use of quantitative models (see 4.2.2).
- ii. **Types:** "physiological DBPE" (measures with physiological meaning) and "non-physiological DBPE".
- iii. **Usage:** DBPE are used to deduce other bio-entities' measures and/or predict unobservable clinical entities.
- iv. **Examples:** ROS levels, consumed O_2 , Mitochondrial PO_2 , etc.

c. **Unobservable Clinical Entities (UCE):**

- i. **Definition:** qualitative condition of a patient.
- ii. **Types:** the classification considers the usage of the UCE. Some examples can be: UCE1, patient classification (such as COPD phenotype), UCE2, prediction of patient evolution.
- iii. **Usage:** within the CDSS.
- iv. **Examples:** COPD phenotype, predicted COPD severity, effectiveness of a given therapy, etc.

Bio-entities can pertain to more than one group in the previous classification. The outcome of the proposed classification is to “map” the relations among sources and the characteristics of those links.

4.2.2 Models

The different types of data are being used through models. Despite the descriptions and classifications presented in different deliverables (D4.1 and D5.1) in reference to the nature of the models used, we proposed an extended classification that allows a practical visualization of the models to be used.

The following figure summarizes the description; however this description is of use within Synergy-COPD and does not intend to be exhaustive. First models are classified as (1) mechanistic or probabilistic and as (2) quantitative or not-quantitative.

Mechanistic models, such as M8, have been described in detail in D4.1 and some section within D4.2; those models pertain to the class of quantitative models, where each entity of the model has associated a value or measure. By mechanistic modelling we denote to model a system as unambiguously defined by its previous state and given relationships between variables, normally using a system of differential/algebraic equations.

By probabilistic model we denote the representation of the system based on estimating the statistical dependency between variables. More precisely, such relationship may express a probability that the state of a variable influence another. The process of estimating the dependency and/or the quantification of it is named Inference. Because the underlying structure to represent probabilistic models is a network, the process is named Network Inference.

Probabilistic models (PM) can include or exclude causality in their representation. For instance ARACNE returns a network, where bio-entities are nodes and where an edge between two nodes denotes some evidence of regulation among them. Despite the interest and usefulness of this network it does not assess causality or quantitative prediction.

Bayesian networks or Structural Models are Quantitative PM (QPM). Those models can be used to generate quantitative predictions. QPM are very useful when there is no information or data to generate a reliable mechanistic model or when the variables included are, for instance, not physiological.

Figure 10 shows a gradient of causality. Non-quantitative PM (NqPM) denote relations among bio-entities, those relations become quantitative in the QPM. In general QPM do not explain causality better than NqPM, however within Synergy we will use QPM to gain better insights in the causality underlying COPD disease evolution. The specifics of this usage, when possible, will be detailed in next subsections.

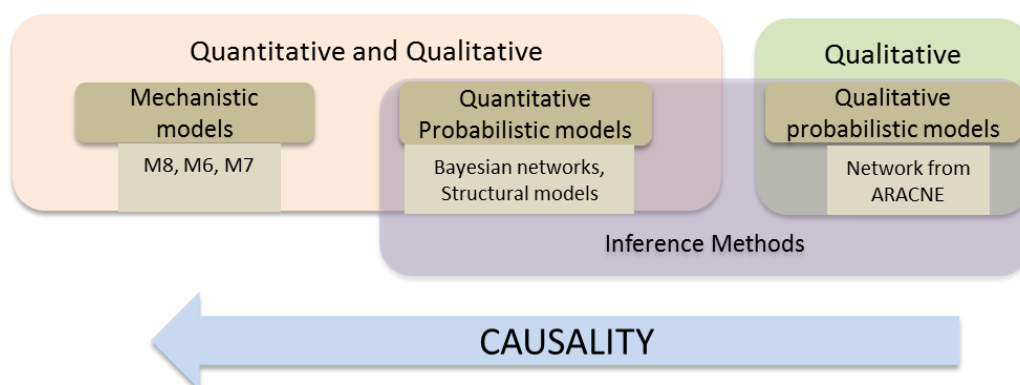


Figure 10: Types of models used in Synergy-COPD.

4.2.3 A visualization of the connections

Figure 11 describes the relation among the models and the entities. This figure presents the working framework that links data and models within the simulation environment. Most importantly, it establishes the key link between basic low-level observable physiological or biological parameters (such as DBPE and OBPE) and high-level unobservable outputs (such as UCE). This is especially relevant for the development of CDSS, as UCEs cannot be used directly within mechanistic models.

In the generic sense mechanistic models are used to deduce the values of some entities; however probabilistic models are key linking measures and predictions for patients. Specific implementation of the model presented in **Figure 11** will depend in the different biological question we aim to address.

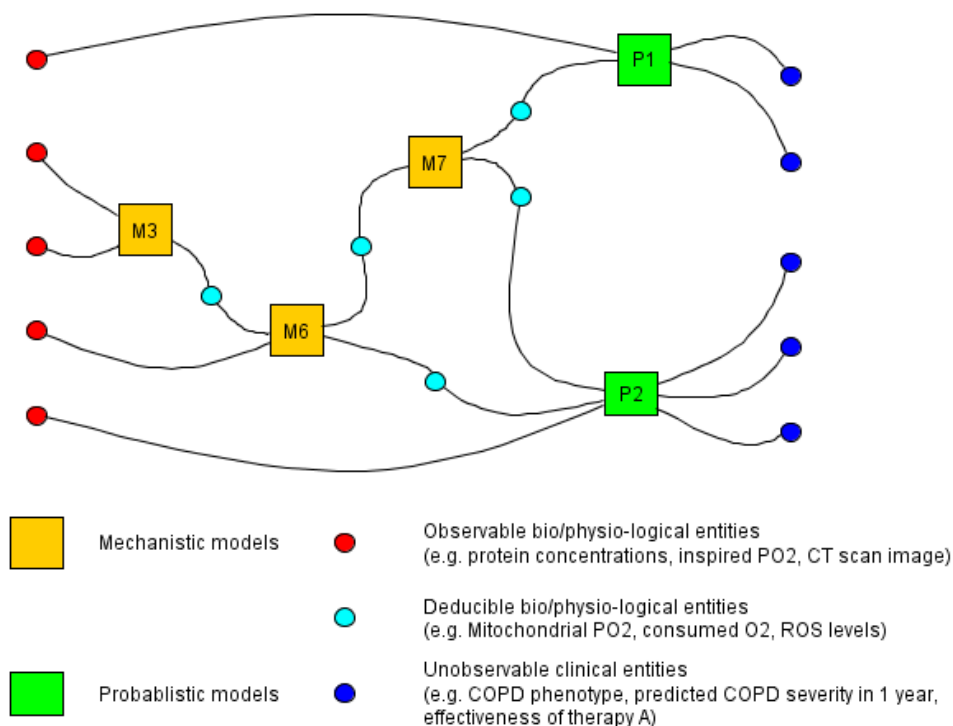


Figure 11: Organization of models and entities.

Whereas **Figure 11** shows the framework of the integration, **Figure 12** highlights the idea of the usage of the different types of models and data types involved. This figure also shows the possible user profiles within different areas of interest.

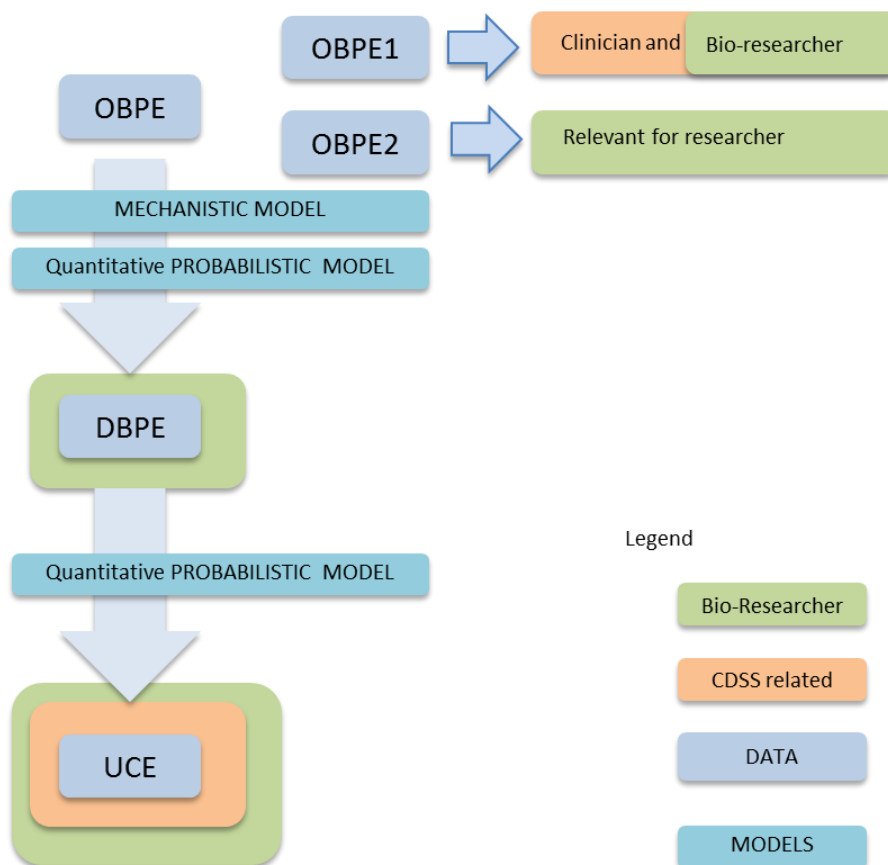


Figure 12: **Relation between data types, models and targeted users.**

4.3 Work-plan

Previous subsections detailed the bio-entities and models to be used within a mechanistic-probabilistic integration. However all those definitions and guidelines were generic as they can only be instantiated once a biological or physiological question is addressed.

Once a question is addressed, we need to follow a step-wise approach that details: (1) the full description of the biological question, (2) the data to be used, (3) the classification of the data (as shown in Subsection 4.2), (4) the integration to be achieved, (5) the models to be used and/or develop within the integration, (6) the relevance to the target users and (7) the practical implementation within the simulation environment.

In this subsection we describe the set of biological questions of interest to be addressed and we describe the long-term goals and the steps to be taken in order to fulfil those goals. Some steps are referring to parts of Subsection 4.4 where the methods to use are described in a generic sense. For instance DS1 denotes the process of enumeration of OBPE, DBPE and UCE entities of interest; see subsection 4.4 for more details.

4.3.1 Phase I: ROS levels

We aim to develop a ROS-centred approach where our capacity to predict ROS levels through mechanistic modelling (M8) and the relation of estimated ROS levels to other elements is studied. This case-study considers the following:

Schedule: October 2011 to December 2012.

Overall goal: Study ROS, our capacity of prediction and its prediction power in COPD.

Data sets to be used: PAC-COPD and Biobridge.

Objectives:

- I. Objective 1. Assessment of associations between estimated ROS levels with mechanistic modelling and blood & skeletal muscle nitroso-redox stress measured in healthy subjects and in COPD patients in Biobridge pre- and post-endurance training (Rodriguez et al. 2011). Interactions of nitroso-redox stress (estimated and measured) within an enhanced network analysis (Turan et al. 2011) will be explored.
 - a. Time to start: December 2011.
 - b. Time to end: December 2012.
 - c. Tasks to perform:
 - i. Related to data: DS1, DS2, DS3 (related to ROS)
 - ii. Related to the models: MechM1, MechM2.
 - iii. Network analysis: PM1.

- II. Objective 2. Mapping of skeletal muscle gene expression into the integrated mechanistic model (M8) to establish semantic interoperability between mechanistic and probabilistic modelling.
 - a. Time to start: October 2011.
 - b. Time to end: June 2012.
 - c. Tasks to perform:
 - i. Data: DS1, DS2, DS3.
 - ii. Model inference: PM2, PM3.

- III. Objective 3. Explore novel ways for quantitative assessment of the interactions between the two modalities of modelling.
 - a. Time to start: June 2012.
 - b. Time to end: October 2012.
 - c. Tasks to perform:
 - i. Definition of the Simulation environment.
 - ii. Define the QPM of interest:
 - iii. Specific instantiations of QPM and mechanistic models.
 - iv. Generate the IQPN.

4.3.2 Phase II: differential pathways between Group I and Group III of PAC-COPD

We aim to explore differential pathways between Group I and Group III of PAC-COPD using network analysis and assess the impact of cell oxygenation by probabilistic modelling.

Schedule: June 2012 to June 2013.

Overall goal: Improve prediction power of COPD-patient classification.

Data sets to be used: PAC-COPD and Biobridge

Objectives:

- I. Objective 1. Identification of differential pathways between Group I and Group III. Exploring the role of nitroso-redox stress on the systemic effects of the disease.
 - a. Time to start: June 2012.
 - b. Time to end: February 2013.
 - c. Tasks to perform:

- i. Related to data: DS1, DS2, DS3.
- ii. Network analysis: PM1, PM2.

II. Objective 2. Identification and validation of biomarkers of the differences found in Objective 1 with potential clinical applications.

- a. Time to start: November 2012.
- b. Time to end: June 2013.
- c. Tasks to perform:
 - i. Model inference: PM3, IQPN.
 - ii. Implementation in the SE-CDSS.

4.3.3 Phase III: shared pathways among co-morbidity studies.

We aim at exploring shared pathways among clusters of co-morbid conditions.

Schedule: June 2012 to June 2013.

Overall goal: the use of co-morbidity studies to identify shared pathways to improve our prognosis power.

Data sets to be used: PAC-COPD, Biobridge and Medicare.

Objectives:

- I. Objective 1. Identification of shared pathways among clusters of co-morbidities observed in COPD patients of the Medicare dataset.
 - a. Time to start: June 2012.
 - b. Time to end: February 2013.
 - c. Tasks to perform:
 - i. Related to data: DS1, DS2, DS3.
 - ii. Network analysis: PM1, PM2, IQPN.

- II. Objective 2. Identification of shared pathways among clusters of co-morbidities observed in PAC-COPD (entire study and group III).
 - a. Time to start: November 2012.
 - b. Time to end: June 2013.
 - c. Tasks to perform:
 - i. Related to data: DS1, DS2, DS3.
 - ii. Network analysis: PM1, PM2, IQPN.

- III. Objective 3. Identification of biomarkers of co-morbidity.
 - a. Time to start: November 2012.
 - b. Time to end: June 2013.
 - c. Tasks to perform:
 - i. Model inference: PM3 (IQPN).
 - ii. Implementation in the SE-CDSS.

4.4 Additional considerations

Previous subsection described three biological and clinically questions to be addressed. Details for each question, including a schedule, were proposed. Each question has specific models, types of models and databases; however in most cases the tasks to perform are similar. We describe these tasks in the current subsection.

For instance in previous subsection, Phase III, Objective 2, it is defined the task DS1. DS1 is, in the present subsection, described as “Enumerate OBPE, DBPE and UCE entities of interest”;

Therefore it states the need of enumeration and classification of the different types of bio-entities within PAC-COPD.

In the current sub-heading, we describe three major, differentiated and independent steps: a) the simulation environment definition (and the CDSS) (Subsection 4.4.1); b) the tasks on data management-classification (Subsection 4.4.2); and, c) the inference of causality by inference methodologies (Subsection 4.4.3).

4.4.1 Simulation environment and CDSS (SE-CDSS)

One major goal of Synergy-COPD is to provide with a COPD-simulation environment to bio-researchers and clinicians. This simulation environment is of use as part of the CDSS (clinicians) or independently of it (bio-researchers). **Figure 13** presents the design of these interactions.

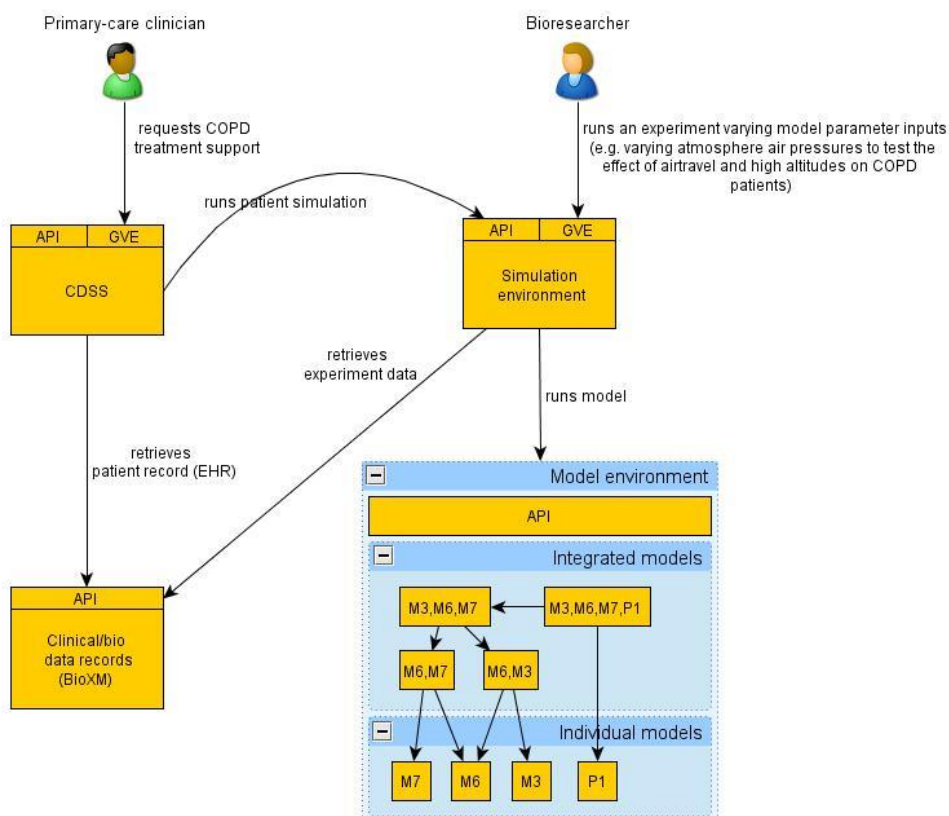


Figure 13: CDSS and Simulation Environment.

Two potential methods can be considered to link the simulation environment (WP4/WP5) with the CDSS (WP6):

- ✓ **Static approach** can be used to link via a *discovered rule* placed in the CDSS. As an example, a bio-researcher, discovers that *inhaled corticosteroids* are only effective in subjects with low protein plasma levels (below a threshold). In this scenario, a rule is then inserted into the CDSS that tests the *protein concentration level* parameter
- ✓ **Integrative approach** (preferred method) - A clinical parameter, *inhaled-corticosteroids effectiveness*, exists in the models and its value is calculated within the simulation environment. The CDSS obtains information of this parameter from a specific patient via execution of the models.

Clearly, the Integration Approach is the one that will be considered in Synergy-COPD because it shows higher modularity and scalability.

The CDSS only operates on high-level clinical rules and parameters, whereas the simulation environment is responsible for representing the relationships between low-level biological or physiological parameters and high-level clinical outcome parameters. See **Figure 13** wherein the Integrative approach is assumed as part of the scheme.

4.4.2 Data and model processing

We aim at using data and models in an integrative approach. Previous sections and subsections detailed a high-level approach of integration, however it is necessary to define a step-wise detailed description of the tasks to be completed in order to succeed in the integration scheme.

The following set of tasks defines the specific actions to be done given a certain conditions (such as sources of data in use); those conditions are detailed in subsection 4.3. We divide the sets of tasks in two subsets; the first subset includes those tasks related to the process and classification of the bio-entities, while the second one aims to describe the different steps in the use of the models.

The tasks described are (note that the tasks are named by different set of letters, those references were used in the previous subsection):

- **DataSets (DS):**
 - **DS1:** Enumerate OBPE, DBPE and UCE entities of interest. Note that UCE entities are most important as they define the validity of the approach.
 - **DS2:** Describe the units of each bio-entity.
 - **DS3:** Describe the present methods used to define UCE entities; nowadays they make use of OBPE entities (see for instance PAC-COPD phenotype classification) and we need to clarify how it was achieved and its validity and usefulness for the clinician.
- **Models:**
 - Use of Mechanistic Models (**MechM**):
 - **MechM1:** Enumerate entities of the mechanistic models that are in OBPE and DBPE.
 - **MechM2:** Compare with units used in data-sets. Translation if necessary.
 - **MechM3:** Evaluation of physiological relevance and correctness of DBPE outputs.
 - Use of Probabilistic Models (**PM**):
 - **PM1:** Search for links of interest:
 - Relations between “UCE” and “OBPE or DBPE”.
 - Relations between OBPE and DBPE.
 - **PM2:** Generate network models for those relations.
 - **PM3:** Infer probabilistic models by (1) using the network models and templates and (2) integrating other sources of data.

- Define the links between mechanistic and probabilistic models and check for their validity.

Steps PM1 to PM3 are further described in the next subsection.

4.4.3 Inference of Quantitative Probabilistic Networks (IQPN)

Probabilistic models are used, for instance, in the linkage between observable, deduced and unobservable clinical bio-entities. This was previously described in **Figure 11** and **Figure 12**. To this end inference network methods are used in the discovery of the **quantitative links among bio-entities**.

The nature of the inference approaches and how to use them in order to discover causal relations is a hot topic within the research community where no consensus of best-approach exists. We propose the following step-wise approach:

- a. Inference of the qualitative network model: for instance we use ARACNE to derive a large network representing the whole spectrum of potential connections between the variables of interest (genes, proteins, metabolites, physiology, etc.).
- b. Selection of modules of interest (subsets of Bio-Entities of interest (BE)): we can apply network modularization approaches that have been designed to integrate knowledge and additional data, which is relevant to a specific biological/clinical context (for example predictive of clinical outcome). These algorithms allow the integration of this information in a search procedure that identifies smaller sub-networks of interest.
- c. Filtering BE: Despite the information generated by the inference network methodologies such as ARACNE, the network proposed does not include causality, and most importantly, it probably includes many false positives. To discard those false positives we aim to intersect the set of bio-entities within the modules of interest with other resources such as the “diseasome” network (Barabási 2007; Lee et al. 2008) and eQTL datasets (Kang et al. 2011; Chambers et al. 2011) (Coassin, Brandstätter, and Kronenberg 2010; Veyrieras et al. 2008).

Quantitative probabilistic modelling of the filtered module: Methods to discover Bayesian network structures of Structural Equation Models, are considered appropriate if they are used to define causal relation when there are a reduced number of BE.

Conclusions of the deliverable

The current document shows that the main challenges of the vertical integration of the different mechanistic models into M8 have been adequately faced. The work in progress is being timely accomplished such that by the end of March 2012 the tools to be developed within WP4 should be fully operational and ready to address specific biological questions of the project.

We understand that section 4 represents a relevant step toward maturity of the whole project. The consortium shares both the conceptual formulations and the working plan (Subsection 4.3) including interrelated biological and technological goals.

In summary, the achievements in vertical integration together with the working plan indicated in Section 4 will be pivotal to formulate the basis of the architecture of the simulation environment and its interactions with the CDSS.

5 References

- Abdellaoui, A., C. Préfaut, F. Gouzi, A. Couillard, M. Coisy-Quivy, G. Hugon, N. Molinari, T. Lafontaine, O. Jonquet, D. Laoudj-Chenivresse, and M. Hayot. 2011. "Skeletal muscle effects of electrostimulation after COPD exacerbation: a pilot study." *European Respiratory Journal* no. 38 (4):781-788. doi: 10.1183/09031936.00167110.
- Albert, Othmer. 2003. "The topology of the regulatory interactions predicts the expression pattern of the *Drosophila* segment polarity genes." *J Theor Biol* no. 223:1-18.
- Aon, M. A., S. Cortassa, E. Marban, and B. O'Rourke. 2003. "Synchronized whole cell oscillations in mitochondrial metabolism triggered by a local release of reactive oxygen species in cardiac myocytes." *J Biol Chem* no. 278 (45):44735-44. doi: 10.1074/jbc.M302673200.
- Barabási, Albert-László. 2007. "Network medicine--from obesity to the "diseasome"." *The New England journal of medicine* no. 357:404-7.
- Barreiro, E., V. I. Peinado, J. B. Galdiz, E. Ferrer, J. Marin-Corral, F. Sanchez, J. Gea, and J. A. Barbera. 2010. "Cigarette smoke-induced oxidative stress: A role in chronic obstructive pulmonary disease skeletal muscle dysfunction." *Am J Respir Crit Care Med* no. 182 (4):477-88. doi: 10.1164/rccm.200908-1220OC.
- Bottino, R., A. N. Balamurugan, H. Tse, C. Thirunavukkarasu, X. Ge, J. Profozich, M. Milton, A. Ziegenfuss, M. Trucco, and J. D. Piganelli. 2004. "Response of human islets to isolation stress and the effect of antioxidant treatment." *Diabetes* no. 53 (10):2559-68.
- Bye, P T P, G A Farkas, and C Roussos. 1983. "Respiratory Factors Limiting Exercise." *Annual Review of Physiology* no. 45 (1):439-451. doi: doi:10.1146/annurev.ph.45.030183.002255.
- Cacuci, D.G. 2007. *Sensitivity and Uncertainty Analysis: Theory*. Chapman & Hall/CRC.
- Cai, J., and D. P. Jones. 1999. "Mitochondrial redox signaling during apoptosis." *J Bioenerg Biomembr* no. 31 (4):327-34.
- Coassin, Stefan, Anita Brandstätter, and Florian Kronenberg. 2010. "Lost in the space of bioinformatic tools: A constantly updated survival guide for genetic epidemiology. The GenEpi Toolbox." *Atherosclerosis* no. 209 (2):321-335.
- Chambers, John C., Weihua Zhang, Joban Sehmi, Xinzhong Li, Mark N. Wass, Pim Van der Harst, Hilma Holm, Serena Sanna, Maryam Kavousi, Sebastian E. Baumeister, Lachlan J. Coin, Guohong Deng, Christian Gieger, Nancy L. Heard-Costa, Jouke-Jan Hottenga, Brigitte Kuhnel, Vinod Kumar, Vasiliki Lagou, Liming Liang, Jian'an Luan, Pedro Marques Vidal, Irene Mateo Leach, Paul F. O'Reilly, John F. Peden, Nilufer Rahmioglu, Pasi Soininen, Elizabeth K. Speliotes, Xin Yuan, Gudmar Thorleifsson, Behrooz Z. Alizadeh, Larry D. Atwood, Ingrid B. Borecki, Morris J. Brown, Pimphen Charoen, Francesco Cucca, Debashish Das, Eco J. C. de Geus, Anna L. Dixon, Angela Doring, Georg Ehret, Gudmundur I. Eyjolfsson, Martin Farrall, Nita G. Forouhi, Nele Friedrich, Wolfram Goessling, Daniel F. Gudbjartsson, Tamara B. Harris, Anna-Liisa Hartikainen, Simon Heath, Gideon M. Hirschfield, Albert Hofman, Georg Homuth, Elina Hypponen, Harry L. A. Janssen, Toby Johnson, Antti J. Kangas, Ido P. Kema, Jens P. Kuhn, Sandra Lai, Mark Lathrop, Markus M. Lerch, Yun Li, T. Jake Liang, Jing-Ping Lin, Ruth J.

F. Loos, Nicholas G. Martin, Miriam F. Moffatt, Grant W. Montgomery, Patricia B. Munroe, Kiran Musunuru, Yusuke Nakamura, Christopher J. O'Donnell, Isleifur Olafsson, Brenda W. Penninx, Anneli Pouta, Bram P. Prins, Inga Prokopenko, Ralf Puls, Aimo Ruokonen, Markku J. Savolainen, David Schlessinger, Jeffrey N. L. Schouten, Udo Seedorf, Srijita Sen-Chowdhry, Katherine A. Siminovitch, Johannes H. Smit, Timothy D. Spector, Wenting Tan, Tanya M. Teslovich, Taru Tukiainen, Andre G. Uitterlinden, Melanie M. Van der Klauw, Ramachandran S. Vasan, Chris Wallace, Henri Wallaschofski, H. Erich Wichmann, Gonneke Willemsen, Peter Wurtz, Chun Xu, Laura M. Yerges-Armstrong, Goncalo R. Abecasis, Kourosh R. Ahmadi, Dorret I. Boomsma, Mark Caulfield, William O. Cookson, Cornelia M. van Duijn, Philippe Froguel, Koichi Matsuda, Mark I. McCarthy, Christa Meisinger, Vincent Mooser, Kirsi H. Pietilainen, Gunter Schumann, Harold Snieder, Michael J. E. Sternberg, Ronald P. Stolk, Howard C. Thomas, Unnur Thorsteinsdottir, Manuela Uda, Gerard Waeber, Nicholas J. Wareham, Dawn M. Waterworth, Hugh Watkins, John B. Whitfield, Jacqueline C. M. Witteman, Bruce H. R. Wolffenbuttel, Caroline S. Fox, Mika Ala-Korpela, Kari Stefansson, Peter Vollenweider, Henry Volzke, Eric E. Schadt, James Scott, Marjo-Riitta Jarvelin, Paul Elliott, and Jaspal S. Kooner. 2011. "Genome-wide association study identifies loci influencing concentrations of liver enzymes in plasma." *Nat Genet* no. 43 (11):1131-1138. doi: <http://www.nature.com/ng/journal/v43/n11/abs/ng.970.html#supplementary-information>.

Davidich, Maria, and Stefan Bornholdt. 2008. "The transition from differential equations to Boolean networks: A case study in simplifying a regulatory network model." *Journal of Theoretical Biology* no. 255 (3):269-277. doi: 10.1016/j.jtbi.2008.07.020.

Fang, H., M. Chen, Y. Ding, W. Shang, J. Xu, X. Zhang, W. Zhang, K. Li, Y. Xiao, F. Gao, S. Shang, J. C. Li, X. L. Tian, S. Q. Wang, J. Zhou, N. Weisleder, J. Ma, K. Ouyang, J. Chen, X. Wang, M. Zheng, W. Wang, and H. Cheng. 2011. "Imaging superoxide flash and metabolism-coupled mitochondrial permeability transition in living animals." *Cell Res* no. 21 (9):1295-304. doi: 10.1038/cr.2011.81.

Garcia-Aymerich, Judith, Federico P Gómez, Marta Benet, Eva Farrero, Xavier Basagaña, Àngel Gayete, Carles Paré, Xavier Freixa, Jaume Ferrer, Antoni Ferrer, Josep Roca, Juan B Gáldiz, Jaume Sauleda, Eduard Monsó, Joaquim Gea, Joan A Barberà, Àlvar Agustí, and Josep M Antó. 2011. "Identification and prospective validation of clinically relevant chronic obstructive pulmonary disease (COPD) subtypes." *Thorax* no. 66 (5):430-437. doi: 10.1136/thx.2010.154484.

Gayeski, T. E., and C. R. Honig. 1988. "Intracellular PO₂ in long axis of individual fibers in working dog gracilis muscle." *American Journal of Physiology - Heart and Circulatory Physiology* no. 254 (6):H1179-H1186.

Geddes, Linda. 2007. "Superhuman: what gives elite athletes the edge?" *New Scientist* (2614):35-41.

Goh, Kwang-Il, Michael Cusick, David Valle, Barton Childs, Marc Vidal, and Albert-László Barabási. 2007. "The human disease network." *Proceedings of the National Academy of Sciences* no. 104 (21):8685-8690. doi: citeulike-article-id:1320727.

- Gomez-Cabrero, David, Albert Compte, and Jesper Tegner. 2011. "Workflow for generating competing hypothesis from models with parameter uncertainty." *Interface Focus* no. 1 (3):438-449. doi: 10.1098/rsfs.2011.0015.
- Griffiths, H. R., C. R. Dunston, S. J. Bennett, M. M. Grant, D. C. Phillips, and G. D. Kitas. 2011. "Free radicals and redox signalling in T-cells during chronic inflammation and ageing." *Biochem Soc Trans* no. 39 (5):1273-8. doi: 10.1042/BST0391273.
- Gupta, S., M. Dhiman, J. J. Wen, and N. J. Garg. 2011. "ROS signalling of inflammatory cytokines during *Trypanosoma cruzi* infection." *Adv Parasitol* no. 76:153-70. doi: 10.1016/B978-0-12-385895-5.00007-4.
- Guzy, Robert D., Beatrice Hoyos, Emmanuel Robin, Hong Chen, Liping Liu, Kyle D. Mansfield, M. Celeste Simon, Ulrich Hammerling, and Paul T. Schumacker. 2005. "Mitochondrial complex III is required for hypoxia-induced ROS production and cellular oxygen sensing." *Cell metabolism* no. 1 (6):401-408.
- Hale, J.K., and H. Koçak. 1991. *Dynamics and bifurcations*: Springer-Verlag.
- Hartman, Philip. 2002. *Ordinary Differential Equations (2nd Edition)*: {Society for Industrial Mathematics}.
- Heinrich, R., and S. Schuster. 1996. *The regulation of cellular systems*: Chapman & Hall.
- Hogan, M. C., D. E. Bebout, and P. D. Wagner. 1991. "Effect of increased Hb-O₂ affinity on VO₂max at constant O₂ delivery in dog muscle in situ." *Journal of Applied Physiology* no. 70 (6):2656-2662.
- Honig, C. R., T. E. Gayeski, A. Clark, and P. A. Clark. 1991. "Arteriovenous oxygen diffusion shunt is negligible in resting and working gracilis muscles." *American Journal of Physiology - Heart and Circulatory Physiology* no. 261 (6):H2031-H2043.
- Hurewicz, W. 2002. *Lectures on Ordinary Differential Equations*: Dover Publications.
- Kaltenbach, Hans-Michael, Sotiris Dimopoulos, and Jörg Stelling. 2009. "Systems analysis of cellular networks under uncertainty." *FEBS Letters* no. 583 (24):3923-3930. doi: 10.1016/j.febslet.2009.10.074.
- Kang, Hyo Jung, Yuka Imamura Kawasawa, Feng Cheng, Ying Zhu, Xuming Xu, Mingfeng Li, Andre M. M. Sousa, Mihovil Pletikos, Kyle A. Meyer, Goran Sedmak, Tobias Guennel, Yurae Shin, Matthew B. Johnson, Zeljka Krsnik, Simone Mayer, Sofia Fertuzinhos, Sheila Umlauf, Steven N. Lisgo, Alexander Vortmeyer, Daniel R. Weinberger, Shrikant Mane, Thomas M. Hyde, Anita Huttner, Mark Reimers, Joel E. Kleinman, and Nenad Sestan. 2011. "Spatio-temporal transcriptome of the human brain." *Nature* no. 478 (7370):483-489. doi: <http://www.nature.com/nature/journal/v478/n7370/abs/nature10523.html#supplementary-information>.
- Klimathianaki, M., K. Vaporidi, and D. Georgopoulos. 2011. "Respiratory muscle dysfunction in COPD: from muscles to cell." *Curr Drug Targets* no. 12 (4):478-88.
- Klipp, E., R. Herwig, A. Kowald, C. Wierling, and H. Lehrach. 2005. "Basic Principles." In *Systems Biology in Practice*, 1-17. Wiley-VCH Verlag GmbH & Co. KGaA.

- Lee, D.-S., J. Park, K. A. Kay, N. A. Christakis, Z. N. Oltvai, and A.-L. Barabási. 2008. "The implications of human metabolic network topology for disease comorbidity." *Proceedings of the National Academy of Sciences* no. 105 (29):9880-9885. doi: 10.1073/pnas.0802208105.
- Li, C., and R. M. Jackson. 2002. "Reactive species mechanisms of cellular hypoxia-reoxygenation injury." *Am J Physiol Cell Physiol* no. 282 (2):C227-41. doi: 10.1152/ajpcell.00112.2001.
- Marin de Mas, Igor, Vitaly Selivanov, Silvia Marin, Josep Roca, Matej Oresic, Lorraine Agius, and Marta Cascante. 2011. "Compartmentation of glycogen metabolism revealed from ¹³C isotopologue distributions." *BMC Systems Biology* no. 5 (1):175.
- Mitchell, P. 1961. "Coupling of phosphorylation to electron and hydrogen transfer by a chemi-osmotic type of mechanism." *Nature* no. 191:144-8.
- Okino, Miles S., and Michael L. Mavrovouniotis. 1998. "Simplification of Mathematical Models of Chemical Reaction Systems." *Chemical Reviews* no. 98 (2):391-408. doi: 10.1021/cr950223l.
- Radulescu, Ovidiu, Alexander Gorban, Andrei Zinovyev, and Alain Lilienbaum. 2008. "Robust simplifications of multiscale biochemical networks." *BMC Systems Biology* no. 2 (1):86.
- Richardson, Russell S., Luke J. Haseler, Anders T. Nygren, Stefan Bluml, and Lawrence R. Frank. 2001. "Local perfusion and metabolic demand during exercise: a noninvasive MRI method of assessment." *Journal of Applied Physiology* no. 91 (4):1845-1853.
- Roca, J, and PD Wagner. 1993. "Principles and information content of the multiple inert gas elimination technique." *Thorax* no. 49:815-824.
- Roche, N., R. Marthan, P. Berger, A. Chambellan, P. Chanez, B. Aguilaniu, P-Y Brillet, P-R Burgel, A. Chauat, P. Devillier, R. Escamilla, R. Louis, H. Mal, J-F Muir, T. Pérez, T. Similowski, B. Wallaert, and M. Aubier. 2011. "Beyond corticosteroids: future prospects in the management of inflammation in COPD." *European Respiratory Review* no. 20 (121):175-182. doi: 10.1183/09059180.00004211.
- Rodríguez-Roisín, Roberto, Mitra Drakulovic, Diego A Rodri, Josep Roca, and Peter D Wagner. 2009. "Ventilation-perfusion imbalance and chronic obstructive pulmonary disease staging severity." *Journal of Applied Physiology*:1902-1908.
- Rodríguez, Diego A., Susana Kalko, Ester Puig-Vilanova, Maitane Perez-Olabarria, Francesco Falciani, Joaquim Gea, Marta Cascante, Esther Barreiro, and Josep Roca. 2011. "Muscle and blood redox status after exercise training in severe COPD patients." *Free Radical Biology and Medicine* (0). doi: 10.1016/j.freeradbiomed.2011.09.022.
- Roper, Ryan T., Maria Pia Saccomani, and Paolo Vicini. 2010. "Cellular signaling identifiability analysis: A case study." *Journal of Theoretical Biology* no. 264 (2):528-537. doi: 10.1016/j.jtbi.2010.02.029.
- Saez-Rodriguez, J., A. Kremling, H. Conzelmann, K. Bettenbrock, and E. D. Gilles. 2004. "Modular analysis of signal transduction networks." *Control Systems Magazine, IEEE* no. 24 (4):35-52. doi: citeulike-article-id:1582732.
- Saltelli, A., K. Chan, and E.M. Scott. 2009. *Sensitivity Analysis*. John Wiley & Sons.

- Schmidt, Henning, Mads F. Madsen, Sune Danø, and Gunnar Cedersund. 2008. "Complexity reduction of biochemical rate expressions." *Bioinformatics* no. 24 (6):848-854. doi: 10.1093/bioinformatics/btn035.
- Selivanov, Vitaly A., Tatyana V. Votyakova, Violetta N. Pivtoraiko, Jennifer Zeak, Tatiana Sukhomlin, Massimo Trucco, Josep Roca, and Marta Cascante. 2011. "Reactive Oxygen Species Production by Forward and Reverse Electron Fluxes in the Mitochondrial Respiratory Chain." *PLoS Comput Biol* no. 7 (3):e1001115. doi: 10.1371/journal.pcbi.1001115.
- Selivanov, Vitaly A., Tatyana V. Votyakova, Jennifer A. Zeak, Massimo Trucco, Josep Roca, and Marta Cascante. 2009. "Bistability of Mitochondrial Respiration Underlies Paradoxical Reactive Oxygen Species Generation Induced by Anoxia." *PLoS Comput Biol* no. 5 (12):e1000619. doi: 10.1371/journal.pcbi.1000619.
- Seydel, R. 2010. *Practical Bifurcation and Stability Analysis*: Springer Verlag.
- Sheu, S. S., W. Wang, H. Cheng, and R. T. Dirksen. 2008. "Superoxide flashes: illuminating new insights into cardiac ischemia/reperfusion injury." *Future Cardiol* no. 4 (6):551-554.
- Slodzinski, M. K., M. A. Aon, and B. O'Rourke. 2008. "Glutathione oxidation as a trigger of mitochondrial depolarization and oscillation in intact hearts." *J Mol Cell Cardiol* no. 45 (5):650-60. doi: 10.1016/j.yjmcc.2008.07.017.
- Sorensen, Michael, and Stephen DeWeerth. 2006. "An Algorithmic Method for Reducing Conductance-based Neuron Models." *Biological Cybernetics* no. 95 (2):185-192. doi: 10.1007/s00422-006-0076-6.
- Sunnaker, Mikael, Henning Schmidt, Mats Jirstrand, and Gunnar Cedersund. 2010. "Zooming of states and parameters using a lumping approach including back-translation." *BMC Systems Biology* no. 4 (1):28.
- Tawhai, M. Howatson, A. J. Pullan, and P. J. Hunter. 2000. "Generation of an Anatomically Based Three-Dimensional Model of the Conducting Airways." *Annals of biomedical engineering* no. 28 (7):793-802. doi: 10.1114/1.1289457.
- Tawhai, Merryn H., Peter Hunter, Juerg Tschirren, Joseph Reinhardt, Geoffrey McLennan, and Eric A. Hoffman. 2004. "CT-based geometry analysis and finite element models of the human and ovine bronchial tree." *Journal of Applied Physiology* no. 97 (6):2310-2321. doi: 10.1152/jappphysiol.00520.2004.
- Tigges, Marcel, Tatiana T. Marquez-Lago, Jorg Stelling, and Martin Fussenegger. 2009. "A tunable synthetic mammalian oscillator." *Nature* no. 457 (7227):309-312. doi: http://www.nature.com/nature/journal/v457/n7227/supinfo/nature07616_S1.html.
- Turan, Nil, Susana Kalko, Anna Stincone, Kim Clarke, Ayesha Sabah, Katherine Howlett, S. John Curnow, Diego A. Rodriguez, Marta Cascante, Laura O'Neill, Stuart Egginton, Josep Roca, and Francesco Falciani. 2011. "A Systems Biology Approach Identifies Molecular Networks Defining Skeletal Muscle Abnormalities in Chronic Obstructive Pulmonary Disease." *PLoS Comput Biol* no. 7 (9):e1002129. doi: 10.1371/journal.pcbi.1002129.

- Turrens, J. F., A. Alexandre, and A. L. Lehninger. 1985. "Ubisemiquinone is the electron donor for superoxide formation by complex III of heart mitochondria." *Arch Biochem Biophys* no. 237 (2):408-14.
- Vestbo, J, W Anderson, H O Coxson, C Crim, F Dawber, L Edwards, G Hagan, K Knobil, D a Lomas, W MacNee, E K Silverman, and R Tal-Singer. 2008. "Evaluation of COPD Longitudinally to Identify Predictive Surrogate End-points (ECLIPSE)." *The European respiratory journal : official journal of the European Society for Clinical Respiratory Physiology* no. 31:869-73.
- Veyrieras, Jean-Baptiste, Sridhar Kudaravalli, Su Yeon Kim, Emmanouil T. Dermitzakis, Yoav Gilad, Matthew Stephens, and Jonathan K. Pritchard. 2008. "High-Resolution Mapping of Expression-QTLs Yields Insight into Human Gene Regulation." *PLoS Genet* no. 4 (10):e1000214. doi: 10.1371/journal.pgen.1000214.
- Vinnakota, K. C., and J. B. Bassingthwaighte. 2004. "Myocardial density and composition: a basis for calculating intracellular metabolite concentrations." *Am J Physiol Heart Circ Physiol* no. 286 (5):H1742-9. doi: 10.1152/ajpheart.00478.2003.
- Wagner, Peter D. 1996. "A theoretical analysis of factors determining VO₂max at sea level and altitude."
- Wang, W., H. Fang, L. Groom, A. Cheng, W. Zhang, J. Liu, X. Wang, K. Li, P. Han, M. Zheng, J. Yin, M. P. Mattson, J. P. Kao, E. G. Lakatta, S. S. Sheu, K. Ouyang, J. Chen, R. T. Dirksen, and H. Cheng. 2008. "Superoxide flashes in single mitochondria." *Cell* no. 134 (2):279-90. doi: 10.1016/j.cell.2008.06.017.
- Zhou, L., M. A. Aon, T. Almas, S. Cortassa, R. L. Winslow, and B. O'Rourke. 2010. "A reaction-diffusion model of ROS-induced ROS release in a mitochondrial network." *PLoS Comput Biol* no. 6 (1):e1000657. doi: 10.1371/journal.pcbi.1000657.
- Zorov, D. B., C. R. Filburn, L. O. Klotz, J. L. Zweier, and S. J. Sollott. 2000. "Reactive oxygen species (ROS)-induced ROS release: a new phenomenon accompanying induction of the mitochondrial permeability transition in cardiac myocytes." *J Exp Med* no. 192 (7):1001-14.
- Zorov, D. B., M. Juhaszova, and S. J. Sollott. 2006. "Mitochondrial ROS-induced ROS release: an update and review." *Biochim Biophys Acta* no. 1757 (5-6):509-17. doi: 10.1016/j.bbabi.2006.04.029.

6 List of Key Words/Abbreviations

BE	Bio-Entities
BI	Bifurcation
CDSS	Clinical Decision Support System
CM	Case Model
COPD	Chronic Obstructive Pulmonary Disease
CT	x-ray Computed Tomography
CTMP	Cross-Talk between Mechanistic and Probabilistic modelling
D	Deliverable
DBPE	Deducible Bio/Physiological Entities
DS	DataSets
EQ	Equilibrium Point
HPV	Hypoxic Pulmonary Vasoconstriction
IQPN	Inference of Quantitative Probabilistic Networks
MechM	Mechanistic Models
MM	Mathematical Model
NqPM	Non-quantitative Probabilistic Models
OBPE	Observable Bio/Physiological Entities
ODE	Ordinary Differential Equation
PM	Probabilistic Models
QPM	Quantitative Probabilistic Models
ROS	Reactive Oxygen Species
SE-CDSS	Simulation Environment and CDSS
UCE	Unobservable Clinical Entities
WP	Work Package

7 ANNEX 1: Model analysis and refinement for the Synergy-COPD mechanistic models

7.1 Sensitivity analysis

7.1.1 Sensitivity analysis for the model of mitochondrial respiration with regards to parameters

The sensitivity analysis for the model of mitochondrial respiration, which fits experimental data, was presented in Selivanov et al, 2011 (see **Annex 2**) as supporting **Table S1**, and here it can be found in **Annex 3** as **Table 5**. In this table the first column gives the list of parameters, next four columns give the relative change of respectively dynamics of NAD⁺ reduction in the absence and presence of rotenone, uncoupled respiration fuelled by succinate, and pyruvate/malate. Next four columns give the relative change of SQ at Qo site of complex III, in the same four simulations as above, then, relative change of SQ at Qn site of complex I, then FMNH, and finally, reduced N2 centres (the highest changes marked in black). The results indicate that significant changes in some parameters hardly affect the simulations (e.g. k_{qp_FS}).

Evidently, the data do not restrict the parameter values and they could not be defined unambiguously. However, changes in these parameters within the range, for which fitting remains good, do not affect the predictions in terms of free radical levels. The parameters shown in black highly affect the simulations. However, it is possible that different combinations of such parameters could fit the measured data equally well because of mutual compensatory changes. In this case, despite the high sensitivity, the parameters can have a wide range of values for which a good fit is obtained. Confidence intervals rather than sensitivity are used to characterize the robustness of parameter determination.

Different sets in the global space of parameters that fit the experimental data could be identified using our stochastic algorithm for minimization of the objective function χ^2 (sum of squares of deviations from measured data normalized by standard deviations). The algorithm identified confidence intervals for parameters based on fixed thresholds of χ^2 .

Table 5 shows the 99% confidence intervals for the free parameters. The ranges for which the values give a good fit to the data are large. Thus, even though the measurements cover various modes of respiratory chain operation, the data do not restrict the parameters sufficiently to define them unambiguously. Various sets over a wide range of parameters can describe the data equally well. However, the situation is different for free radical levels predicted for the simulated experimental conditions. In addition, **Table 5** lists intervals for predicted free radical levels simulated using the parameters sets that fit the data with χ^2 that is below the threshold. The confidence intervals for free radical levels are generally much narrower, so the predicted values are more robust. Although the intervals for SQ at Qo sites in succinate-fuelled mitochondria are relatively large, they are clearly almost the same for both conditions (with or without rotenone). The levels of all free radicals in complex I under the conditions for the first two simulations are very robust, despite the high parameter variability. If the parameters give a good fit, the model predicts similar levels of complex I radicals. Although the intervals are relatively large under the third condition (pyruvate/malate supply), they are much lower than the intervals for the condition of succinate supply, as well as the levels of radicals in complex III.

7.2 Model reduction

7.2.1 Reduction of the mitochondrial respiration model

The reduction of the model of mitochondrial respiration is based on the fact that the automated algorithm constructing the set of model equations is somehow excessive. This algorithm is described for respiratory complex III (Selivanov et al. 2009), and it was extended to the whole respiratory chain in the framework of Synergy-COPD (see **Annex 2**).

Briefly, the general algorithm constructing the Ordinary Differential Equations (ODEs) for the model of respiratory chain accounts for all the possible redox states of respiratory complex III. It assumes that the core of the complex contains four redox sites: cytochrome b with its two hemes, b_H and b_L , cytochrome c_1 , and the iron-sulphur containing Rieske protein ($b_H-b_L-c_1-FeS$). Each of these redox sites can carry one valence electron. The core of the complex can bind ubiquinone either in the matrix (Q_i) or cytosolic (Q_o) side of the inner mitochondrial membrane ($b_H-b_L-c_1-FeS-Q_o-Q_o$, $Q_i-Q_i-b_H-b_L-c_1-FeS$, $Q_i-Q_i-b_H-b_L-c_1-FeS-Q_o-Q_o$), giving four different species of the complex. The model describes binding/dissociation of ubiquinone/ubiquinol that results in interconversion of these four species. It takes into account that ubiquinone is a two-electron carrier.

The oxidized state of each redox site is coded as a binary “0” and the reduced state as “1”. In this way various combinations of reduced and oxidized states of carriers can be represented as a four-digit binary numbers with corresponding decimal values from 0 to 15 (i.e. from 0000 to 1111 in binary) representing redox states of the core ($b_H-b_L-c_1-FeS$), six-digit binary numbers with corresponding decimal values from 0 to 63 (i.e. from 000000 to 111111 in binary) representing the redox states of each of the two species containing one ubiquinone, ($Q_i-Q_i-b_H-b_L-c_1-FeS$ and $b_H-b_L-c_1-FeS-Q_o-Q_o$) and eight-digit binary numbers with corresponding decimal values ranging from 0 to 255 (i.e. from 00000000 to 11111111 in binary) representing the redox states of the species containing two ubiquinones ($Q_i-Q_i-b_H-b_L-c_1-FeS-Q_o-Q_o$). The algorithm constructs an ODE system for all the species and their redox states (400 equations in total). This ODE system accounts for the transitions of electrons between carriers resulting in oxidation of the donor ($1 \rightarrow 0$) and reduction of the acceptor ($0 \rightarrow 1$), and binding/dissociation of ubiquinone/ubiquinol. These reactions are simulated in accordance with the well accepted Q-cycle theory and are described in detail in (Selivanov et al. 2009).

The following electron transitions performed by complex III are considered:

- From ubiquinol bound at Q_o site to the iron-sulfur center of the Rieske protein (qo_FS) and the reverse transition (FS_qo).
- From the iron-sulfur center of the Rieske protein to cytochrome c_1 (FS_c_1) and the reverse transition (c_1_FS).
- From the semiquinone bound at the Q_o site to the b_L heme of cytochrome b (qo_bl) and the reverse transition (bl_qo).
- From the b_L to the b_H heme of cytochrome b (bl_bh) and the reverse transition (bh_bl).
- From the b_H heme of cytochrome b to an ubiquinone bound at Q_i site (bh_qi_1) and the reverse transition (qi_1_bh).
- From the b_H heme of cytochrome b to a semiquinone bound at Q_i site (bh_qi_2) and the reverse transition (qi_2_bh).

The model considers the following reactions of binding/dissociation of ubiquinone/ubiquinol to/from complex III:

- binding of ubiquinol at the Q_o site ($qhob$)
- dissociation of ubiquinol from the Q_o site ($qhob$)
- binding of ubiquinone at the Q_i site (qib)
- dissociation of ubiquinone from the Q_i site (qid)
- dissociation of ubiquinone from the Q_o site (qod)
- binding of ubiquinone at the Q_o site (qob)
- dissociation of ubiquinol from the Q_i site ($qhid$)
- binding of ubiquinol at the Q_i site ($qhib$)

The rate constants of the reactions listed above are shown in **Table 2**. In this table, units for the rate constants of monomolecular reactions of electron transition inside the complex and reactions of dissociation n are s^{-1} . For bimolecular reactions of ubiquinone/ubiquinol binding units are $(nmol/mg)^{-1}s^{-1}$. The reactions simulated and abbreviations used in the names of constants are explained in Methods (See Annex 2), part “Complex III model”.

Reaction	Model (rate constants)		
	145	257	267/272
k_{qo_FS}	348565	316575	316897
k_{FS_qo}	11515	43575	43852
k_{FS_c1}	510160	509775	510162
k_{c1_FS}	150780	137025	137082
k_{qo_bl}	69090	68775	69099
k_{bl_qo}	3220	1091	3225
k_{bl_bh}	87675	87675	87688
k_{bh_bl}	1155	539	1156
K_{bh_qi1}	99540	891608	90521
k_{qi1_bh}	29995	4056	30015
k_{bh_qi2}	298200	297675	298139
k_{qi2_bh}	27090	32498	27093
k_{c1c}	84525	112538	257
k_{lk}	1400	1417	1417
k_{qhob}		172200	2793
k_{qhod}		2326	2585
k_{qjib}		12600	12682
k_{qid}		237	180
k_{qod}		24554	3525
k_{qob}		4	740
k_{qhhd}		3768	3768
k_{qhhd}		17770	6912

Table 2: Rate constants of elementary reactions taking place in complex III.

7.2.1.1 Simplification of complex III model to 255 equations

Ubiquinone is a two-electron carrier and in the model two binary digits are used to model the state of ubiquinone, giving 4 possible combinations (00, 01, 10, and 11), although there are only 3 physically distinct states (i.e. 01 and 10 represent the same state, semiquinone with one valence electron). The algorithm was originally designed so that only the state “01” can be produced, and the amount of species containing “10” as a state of semiquinone always was zero. The presence of equations describing such zero-concentration states did not change the result of numerical integration of the initial value problem. Such subsidiary equations can be eliminated not affecting the result. We modified the algorithm constructing the ODEs so that it does not include the equations for the states containing “10” semiquinone. This modification allowed reducing the number of equations for the model of respiratory complex III from 400 to 255.

7.2.1.2 Further simplification of complex III model to 145 equations

In accordance with the Q-cycle mechanism, ubiquinol bound in the Qo site is oxidized giving its electrons to FeS center of the Rieske protein and cytochrome b_H and releasing its protons into the intermembrane space. Then the ubiquinone formed is released. The next pair of electrons can be

transported only after the next ubiquinol is bound to the same Qo site. For simplicity, release of ubiquinone and binding of new ubiquinol can be combined and described as an exchange of ubiquinone with ubiquinol at the Qo site. Similarly, the release of ubiquinol and binding of ubiquinone at Qi site can be combined. In this way, all the reactions of Q-cycle can be described considering only one configuration of complex III that contains two bound ubiquinones (Qi-Qi-b_H-b_L-c₁-FeS-Qo-Qo). After removing “zero-states” containing “10” semiquinone (as described above) and taking into account the conservation of the total contents of complex III and ubiquinone, the above model is reduced from 255 to 145 equations.

7.2.2 Model reduction for the oxygen transport and utilisation model

Model M6 includes an equation that links the amount of consumed oxygen, the maximum amount of consumed oxygen and the partial pressure of oxygen in the mitochondria (P50). The mathematical formulation of this link is:

$$V_{O_2} = V_{O_2max} \left(1 - e^{-\frac{0.069 \cdot P_{mitoO_2}}{P_{50 \text{ mito}}}} \right) \quad (27)$$

This equation updates previous models. Despite that the inclusion of this equation is necessary (and has been already discussed in other deliverables), we aim to clarify its relevance. It is not our aim to reduce the model by discarding this equation, but analysing the model with and without it to highlight the relevance of P50.

As an example, cardiac output average value was normalized adding +-(50%) to the average value published in (Wagner 1996), its effect was investigated on the value of one of the outputs of the model which is oxygen delivery. **Figure 14** illustrates the impact of not using (blue) versus using (green) Wagner’s mitochondrial equation (eq. 27).

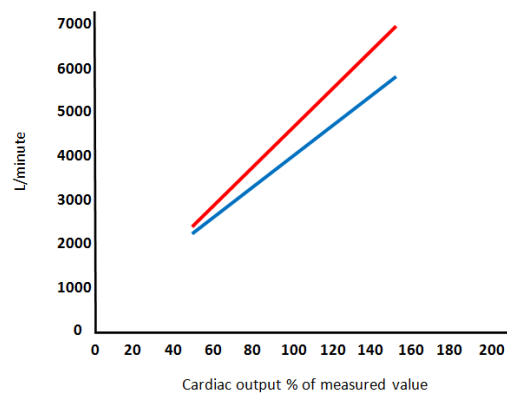


Figure 14: Impact in oxygen delivery when using (green) and not using (blue) eq. 27

Thus it could be seen that, in this specific case, not using the p50mit-related equation only results in a small error; however its effect depends on the Cardiac output estimation. More experiment procedure might be needed to prove this concept, and we aim to test this analysis under different physiological value’s ranges.

7.3 Numerical bifurcation analysis

7.3.1 Numerical bifurcation analysis of the respiratory chain

A numerical bifurcation analysis of the respiratory chain was started with the model of complex III simplified to 145 equations (referred to further as **model 145**) as described in subsection 7.2.1.2. This model accounts for only one type of complex III species, namely, denoted as Q_i - Q_i - b_H - b_L - c_1 - FeS - Q_o - Q_o , where the repeated ubiquinone symbols at the ends accommodate the possible redox states. Binding/dissociation of quinones in this model is accounted for by the substitution of reduced bound forms at Q_i for oxidized free form and oxidized bound forms at Q_o for reduced free form. Continuation of steady state solutions for transmembrane electric potential as a function of succinate concentration with CL_MATCONTL revealed an interval of parameter values with multiple steady state solutions (**Figure 15A**, yellow curve) enclosed between two limit points (LP). Left hand side (A) of **Figure 15** illustrates $\Delta\Psi$ (transmembrane potential) at steady state as a function of V_{mSDH} , with succinate concentration in relative units. The yellow curve is obtained by continuation of steady state (cnt) in the space of V_{mSDH} using CL_MATCONTL. The points indicated as “reduced” and “oxidized” are obtained as the steady states approached by the solution of an initial value problem starting from initially reduced or oxidized states of electron carriers respectively. Limit points (LP) are designated by symbols. Right hand side (B) of **Figure 15** illustrates stable steady states for semiquinone (SQ) formed at Q_o site obtained from the same solutions of initial value problem as in A. The values of other parameters are shown in Table 2 (column “145”). These values were optimized to maximize the width of the interval of V_{mSDH} corresponding to *multiple steady state solutions*. This interval of multiple solutions contains two curve segments of stable steady states and one curve segment of unstable steady states in between.

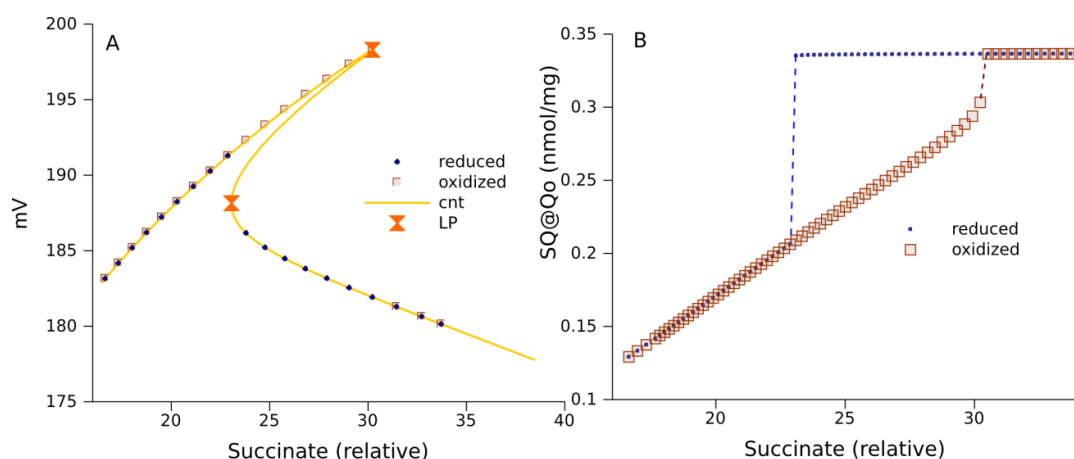


Figure 15: Multiple steady state solutions for the ODE system corresponding to the simplified model of complex III (model 145).

If initially the electron carriers are reduced, the solution for the ODE system approaches a steady state located on the lower branch of **Figure 15A**, and if initially the carriers are oxidized, the solution approaches a steady state on the upper branch. These two segments of the yellow curve, representing the whole continuum of steady states, consist of stable steady states. The intermediate segment linking these two separated branches consists of unstable steady states. Outside of the region between the two limit points the steady states approached from the initially reduced and oxidized states coincide.

Stable steady state concentrations of semiquinone radicals occupying the Q_o site of complex III are shown in **Figure 15B**. Within the same interval of parameter values that gives multi-stability in **Figure 15A**, the system can persist either in a state of the highest content of such radicals (characterized by the highest Reactive Oxygen Species (ROS) production rate), or in a state of much lower content of the free radicals (characterized by lower ROS production rate) at the same parameters' values. The initial level of reduction determines the curve segment of stable steady state solutions that the system will approach. The branches of stable steady states are connected with a segment of unstable steady states (not shown).

Model 145 has 13 parameters. **Figure 15** shows curve segments of multiple steady state solutions in an interval of values for one parameter. The shape and size of these curve segments depend on the values of other parameters. The width of this interval may be smaller or the interval may even disappear. **Figure 15A** shows an interval of V_{mSDH} values corresponding to multiple steady states (23.0, 30.2), obtained using an algorithm (see subsection 7.3.1.2) that scans all the parameters with the objective of finding as large interval as possible.

Including in our model all of the four species of complex III and an explicit description of quinone binding/dissociation increase the number of equations to 257. This more detailed model also has a region of multiple steady state solutions. Application of the same algorithm maximizing the V_{mSDH} region of multiple steady states resulted in the interval (33.8, 46.1). This interval is approximately twice as large as in the case of model 145, but qualitatively the behaviour of the two models remains similar (**Figure 16**). Regarding this figure, the values of other parameters are shown in **Table 2** (column “257”). The designations of panels, curves and points are the same as in Figure 15. Evidently, model 145 faithfully accounts for the main properties of complex III defined by the Q-cycle mechanism.

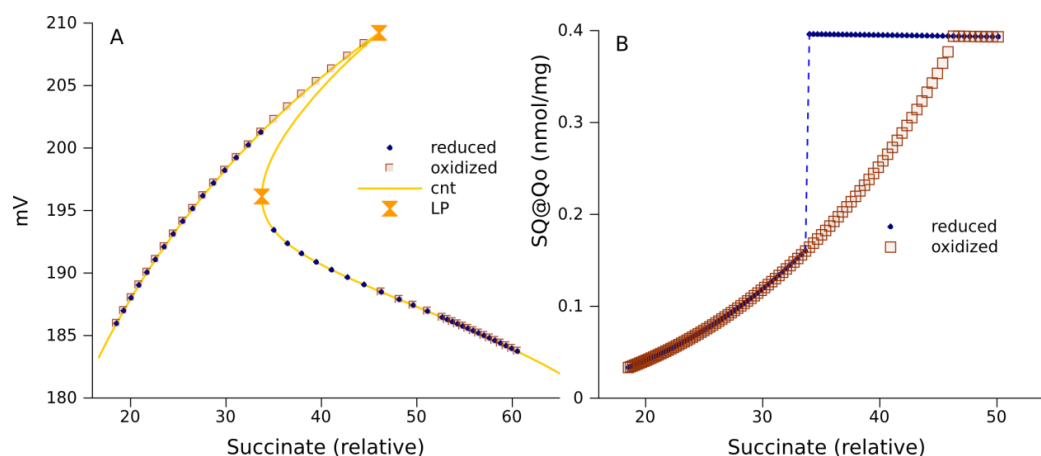


Figure 16: Multiple steady state solutions for the model of complex III consisting of 257 ODEs in the space of the parameter reflecting succinate concentration.

Model 267 is obtained by adding to model 257 equations that account for reactions taking place in complex I. This extended model contains almost all of the essential components of the respiratory chain model that we used for the analysis of experimental data (Selivanov et al. 2011). Using it enables us to start the bifurcation analysis from a “real” set of parameter values that reproduces the measured dynamics of NADH reduction in the presence and absence of rotenone, and maximal and state 4 respiration rates when mitochondria are fuelled by succinate or pyruvate/malate. Numerical continuation of steady state solutions for $\Delta\Psi$ as a function of succinate concentration indicates the existence of a region with multiple solutions enclosed between two limit points (**Figure 17A**). The lower stable steady states for $\Delta\Psi$ are coupled with the highest levels of SQ radicals (**Figure 17B**); this may be a physical basis for high ROS production rates. In **Figure 17**, the rate constant of electron transport from cytochrome c1 to cytochrome c (k_{c1c}) was 735 min^{-1} . The values of other parameters, which correspond to the best fit to measured dynamics of NADH and oxygen consumption under states 4 and 3 of mitochondrial respiration [2011], are shown in **Table 2** (column “267/272”) and **Table 3**. The designations of panels, curves and points are the same as in Figure 15; an additional point “H” designates a Hopf bifurcation. With respect to **Table 3**, units for the rate constants of monomolecular reactions of electron transition inside the complex and reactions of dissociation are s^{-1} . For bimolecular reactions of ubiquinone/ubiquinol binding units are $(\text{nmol/mg})^{-1}\text{s}^{-1}$. The reactions simulated and abbreviations used in the names of constants are explained in Methods (see **Annex 2**), part “Including complex I”.

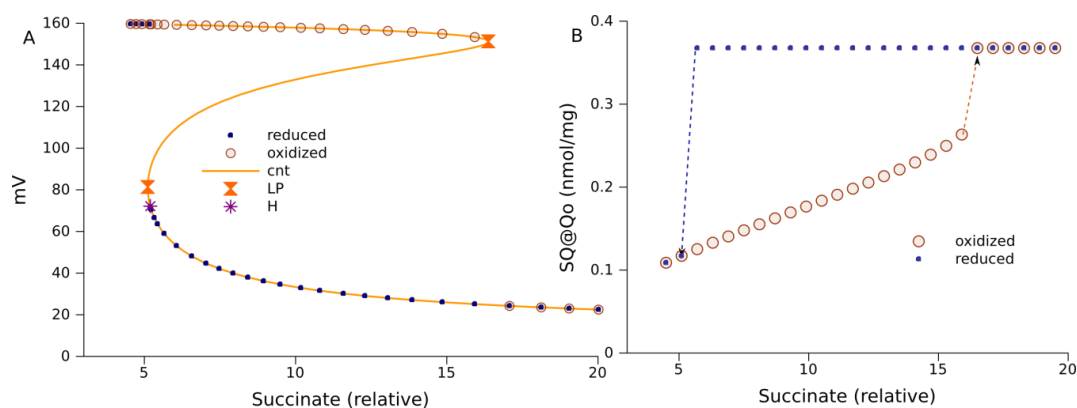


Figure 17: Multiple steady states for the integrated models of complex I and III (model 267) in the space of the parameter reflecting succinate concentration.

Reaction	Rate Constant
$k_{f_{mn}}$	368553
$k_{r_{f_{mn}}}$	508076
$k_{f_{n2}}$	99177
k_{n2_f}	4669
$k_{n2_{q1}}$	500906
$k_{q1_{n2}}$	51112
$k_{q_{pqn}}$	31657
$k_{r_{q_{nqp}}}$	116
$k_{q_{hdis}}$	213647
$k_{q_{hbnd}}$	20398
$k_{q_{bnd}}$	201029
$k_{q_{dis}}$	2829
$k_{n2_{q2}}$	146954
$k_{q2_{n2}}$	2159

Table 3: Rate constants of elementary reactions taking place in complex I.

The measurements that were used to find the given set of parameters were performed in a suspension of isolated mitochondria. The rate of electron transport from cytochrome *c1* to cytochrome *c* is the parameter most affected by the procedure of isolation, since it depends on the structure of intermembrane space, which is significantly changed after the isolation. In intact mitochondria the value of this parameter is expected to be higher than in isolated mitochondria. Increasing its value by less than an order of magnitude increases the interval of multiple steady state solutions to infinity (**Figure 18**). Starting from an initially oxidized state the system approaches a steady state, which with numerical continuation on substrate concentration as a parameter, results in the upper curve in **Figure 18A**. This curve does not contain any bifurcation points. However, at a high substrate concentration, and starting from a reduced state, the system approaches another steady state located in a different curve marked blue in **Figure 18A**. At high substrate concentrations, the lower segment of this curve is stable, but a decrease of the substrate supply parameter ultimately leads to a limit point. Further continuation of steady state solutions reverses the direction of change of this parameter giving a segment of unstable steady states, which is never connected with the upper curve of stable steady states in the space of the one parameter considered. Similar to the cases analysed above, the steady states corresponding to low $\Delta\Psi$ values are characterized by the maximal levels of free radicals SQ at Qo site, and, the steady states corresponding to high $\Delta\Psi$ are accompanied by low levels of SQ at Qo site (**Figure 18B**).

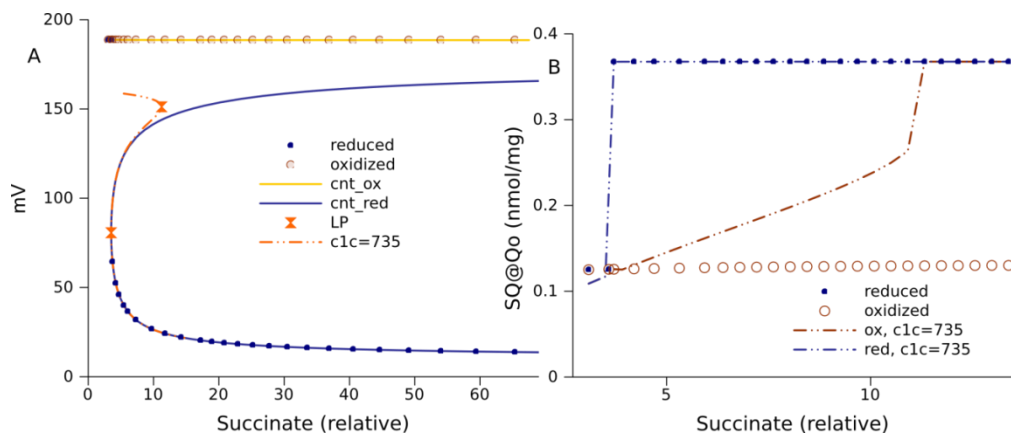


Figure 18: Infinite interval of multiple steady states for the integrated models of complexes I and III (model 267) as a function of succinate concentration (V_{mSDH}).

The change of a single parameter that characterizes interaction between cytochromes $c1$ and c (k_{c1c}) gives a qualitatively different behaviour of model 267, as is seen from the co-location of curves from **Figure 17** into **Figure 18** (in this figure, the rate constant of electron transport from cytochrome $c1$ further to cytochrome c (k_{c1c}) was 4200 s^{-1} . The values of other parameters, the same as in **Figure 17**, are shown in **Table 2** and **Table 3**. The dash-dot-dot curves are the same as in **Figure 17**). This difference in bifurcation diagrams can explain the change in ROS production induced by hypoxia/re-oxygenation. Indeed, the decrease of this parameter can be a result of deprivation of oxygen. Assume that before hypoxia the system effectively functions at some point on the upper yellow curve (**Figure 18A**). Suppose the change of k_{c1c} induced by hypoxia transforms the properties of the system so that the orange curve becomes the continuum of its steady states. If before hypoxia the functional steady state was to the right of the rightmost limit point in orange curve, then after hypoxia the system evolves until it reaches a steady state in the lower segment of orange curve (coinciding with the lower segment of blue curve). If then re-oxygenation comes, and the blue and yellow curves again become the continuum of steady states of the system, it remains in the same low segment of blue curve. Thus, the hypoxia and re-oxygenation changes the state of the system. Before hypoxia it generated high $\Delta\Psi$ and slowly produces ROS (brown cycles in **Figure 18B**), whereas after re-oxygenation it stays in a state characterized by low $\Delta\Psi$ and rapidly produces ROS (blue points in **Figure 18B**).

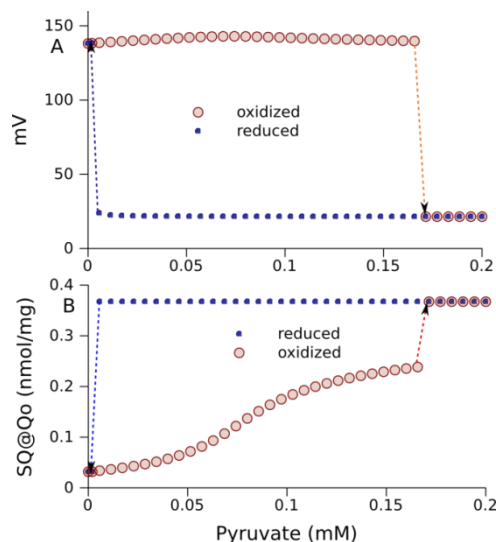


Figure 19: Multiple steady states at various pyruvate concentrations.

Further extension of the ODE model to 272 equations, as described in subsection 3.4.4.3, by including the reactions of the TCA cycle, allowed us to study a more detailed model of the biological system. In the extension, pyruvate serves a substrate for the TCA cycle, which provides succinate for complex II and NADH for complex I. Using parameter values verified by fitting the measured dynamics of NADH and respiration rates (Selivanov et al. 2011), the model predicts the existence of wide range of pyruvate

concentrations with two stable steady state segments, **Figure 19**. This figure shows multiple steady states at various pyruvate concentrations when the model 267 was extended to 272 equations by including TCA cycle as described in Section 3.4.4.3: Link between the model of central metabolism and respiration. The values of parameters are shown in **Table 2**, **Table 3** and **Table 4**. They are the same as used elsewhere to fit the experimental dynamics of NADH and respiration rate (Selivanov et al. 2011).

This model, in fact, can enter into an oscillatory mode of operation. An increase of the cytochrome *c1* to cytochrome *c* electron transition rate (k_{c1c}) to $782s^{-1}$ and an increase in V_{mSDH} (equation (5)) to 1714 nmol/s/mg switched the model into an oscillatory mode (**Figure 20**). The change of succinate concentrations significantly alters the period of oscillation (**Figure 20A-D**) while hardly affecting the phase of free radical increase, whereas the increase of pyruvate concentrations greatly increases the duration of free radical increase (**Figure 20E-F**).

Reaction	Parameter value
k_{pyr}	53
k_{CS}	2109
k_{TCA}	876
V_{SDH}	171
k_{MDH}	452
k_{suc}	376
k_{ME}	0.000231
k_{sm}	7
Km_{suc}	0.5
Km_q	0.5

Table 4: Parameters of TCA cycle reactions and substrate transport.

7.3.1.1 Discussion

Bifurcation behaviour inherent in the mechanism of electron transport in complex III was revealed by analysis of the simplest models that did not include anything except the Q-cycle reactions taking place in complex III. Two models of complex III were considered, where the model number is the size of the system of ODEs. Model 145 has a highly simplified representation of the binding and dissociation of quinones. Model 257 has a more detailed representation. Both models have two stable steady state solutions in an interval of the parameter representing succinate concentration; see **Figure 15** and **Figure 16**. This possible bistability (depending on parameter values) is inherent in the Q-cycle mechanism of electron transport in complex III, and may be the basis of increased ROS production by mitochondria after hypoxia/re-oxygenation.

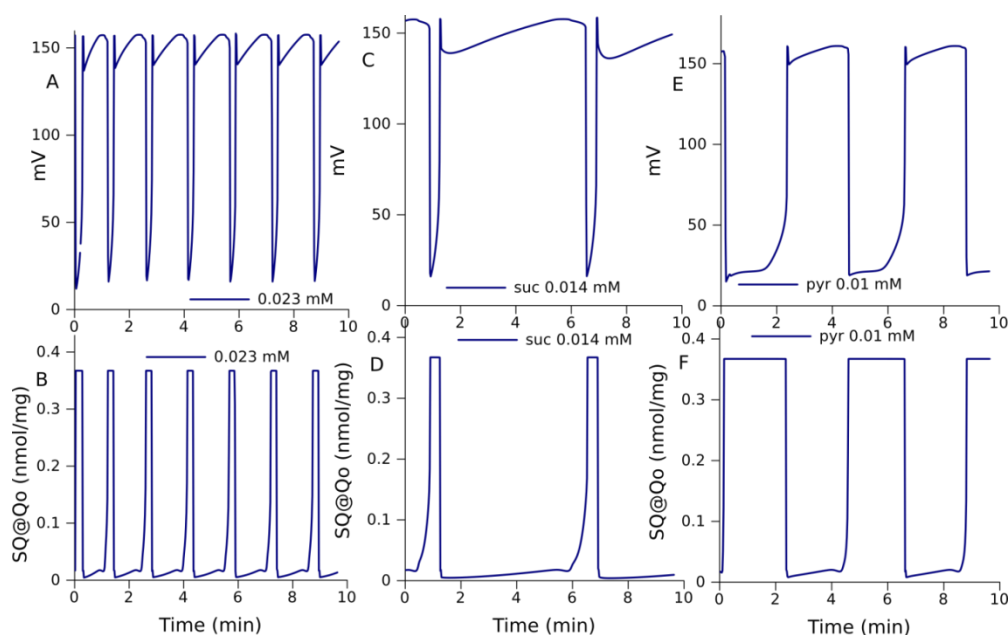


Figure 20: Sustained oscillations of levels of SQ bound at Qo site and $\Delta\Psi$ in model 272.

Extending the model by including complex I, to give model 267, it increases the width of the maximal interval of multiple solutions or may even make it infinite, as shown in **Figure 18**. The width of this interval is sensitive to the parameter (k_{c1c}) that characterizes interaction between cytochromes *c1* and *c*. This parameter can be affected by isolation of mitochondria, but also, in living cells, it characterizes the capacity of complex III to pass electrons to oxygen as a final acceptor. Thus, it characterizes the accessibility of oxygen. The comparison of **Figure 17** and **Figure 18** illustrates how hypoxia and re-oxygenation may perturb the system to a state of very high ROS production.

Further extending the model by including the reactions of TCA cycle, to give model 272, keeps an interval of parameters where it has multiple steady state solutions, but also introduces an oscillatory mode of behaviour. The model has two stable steady states at the parameter values defined by fitting measured experimental data, as shown in **Figure 19**. The switch to an oscillatory mode, shown in **Figure 20**, required increased values of two parameters, k_{c1c} and V_{mSDH} . In **Figure 20**, the rate constant of electron transport from cytochrome *c1* to cytochrome *c* (k_{c1c}) was 782 min^{-1} . V_{mSDH} was 1714 nmol/min/mg . The values of other parameters used are shown in Table 2, Table 3 and Table 4. Panels A and B show predicted oscillations when external pyruvate concentration is 0.001 mM and succinate is 0.023 mM. C and D, pyruvate concentration is the same, 0.001 mM and succinate is 0.012 mM. E and F, pyruvate increased to 0.01 mM, succinate remained the same, 0.012 mM.

The parameters shown in **Table 2**, **Table 3** and **Table 4** that were used for model 272, were defined as the best fit of experiments performed in vitro in isolated mitochondria. One can expect that mitochondria in suspension could be more swelled compared to their state in living cells. It may be expected that the intermembrane space is changed by the procedure of isolation. This change of intermembrane space may decrease k_{c1c} . Natural variability of V_{mSDH} , imprecision of its determination by data fitting, and inhomogeneity of the mitochondrial matrix space that results in spatial variability of succinate dehydrogenase activity all contribute to the uncertainty in the estimated value of V_{mSDH} . Our results show that respiratory chain has an oscillatory mode of operation and that the “oscillatory region” of parameter values is not so far away from the sets defined by experimental data fitting.

In fact, in mitochondria of living cells, flashes of ROS production and oscillations accompanied by decrease of $\Delta\Psi$ can be measured either as a response to laser excitation (Zorov, Juhaszova, and Sollott 2006), or as a spontaneous mitochondrial activity (Fang et al. 2011; Sheu et al. 2008; Slodzinski, Aon, and O'Rourke 2008; Wang et al. 2008; Aon et al. 2003). The decrease of $\Delta\Psi$ that accompanies ROS flashes was explained as a consequence of a ROS activated permeability transition (Zorov et al. 2000; Zorov, Juhaszova, and Sollott 2006) or inner membrane anions channel (Zhou et al. 2010). We do not study these two mechanisms here, and admit that they could take place. However, our results

show that ROS sparks and a decrease of $\Delta\Psi$ may be a direct consequence of the dynamics of electron transport, and may not require the permeability transition or IMAC activation.

7.3.1.2 Algorithm designed to maximize the region of multiple steady state solutions

Step 0. Localization of an interval of multiple solutions.

Once a multiple steady state solutions, approachable from distinct initial states, are found, then the interval of parameter of interest corresponding to multiple steady state solutions can be localized. In case of two stable steady states (as shown in **Figure 15** and **Figure 16**) the method of such localization is simple: starting subsequently from the proximities of each of the steady states, the algorithm repeatedly increases the parameter of interest and calculates approaching the corresponding steady states, until the obtained steady state coincide. This minimal value of parameter that corresponds to coincidence of solutions from different initial states gives right boundary of the interval of multiple steady states. The same algorithm applied for the decrease of the parameter gives the left boundary of the interval for the given parameter.

Step 1. Change a parameter in a given set.

The broadness of the interval of multiple solutions in the dimension of analysed parameter depends on the values of other parameters. The algorithm changes the value of parameter, randomly chosen in the list of parameters designed for change, and repeats **step 0**. If the interval of multiple solutions increases after this change, the algorithm accepts the changed parameter, in the opposite case it rejects the change and comes back to the previous value of the changed parameter.

Step 2. Passing through the lit of parameters.

After the step of acceptance or rejection of the change, the algorithm randomly choses another parameter from the list and repeats **step 1**. This procedure is repeated until the changes for all parameters in both directions are checked.

Step 3. Maximization of the interval of multiple solutions.

Step 2 is repeated many times until no changes after passing through the whole list of parameters are accepted, in other words, when maximal length of the interval of multiple steady state solutions is reached.

In every calculation the algorithm verifies (by comparing intermediate and last points) whether steady state is approached. This verification detects any kind of periodic solutions if they appear at some point.

7.4 Code optimisation

7.4.1 Code optimisation within M6

Currently, the implementation of the two mechanistic models is stand-alone applications, built statically. Therefore, the first step is to modularize both implementations, and separate the models from the main applications, so that they can be reused as shared object libraries in a new application, allowing for the combination of the two.

The old model M6 FORTRAN code has been therefore refactored and can be now built according to the new ISO/IEC 1539-1:2010 standard Fortran2003, also known as "Modern Fortran". The added benefit is a standard way to create shared libraries interoperable with C, using the ISO_C_BINDING intrinsic module. This allows for the technical sharing of functions and variables with the ROS model, which is already implemented in C.

The refactored code can be found in the Synergy subversion source-code control repository:

<https://synergy-copd.eu/svn/Synergy-COPD/PhysModels/trunk/lungsim/>

8 ANNEX 2: Supporting material for the detailed model of respiratory chain

Reactive Oxygen Species Production by Forward and Reverse Electron Fluxes in the Mitochondrial Respiratory Chain

Vitaly A. Selivanov^{1,2}, Tatyana V. Votyakova^{3*}, Violetta N. Pivtoraiko⁴, Jennifer Zeak³, Tatiana Sukhomlin⁵, Massimo Trucco³, Josep Roca⁶, Marta Cascante^{1*}

1 Departament de Bioquímica i Biologia Molecular, Facultat de Biologia, Universitat de Barcelona, and IBUB, Barcelona, Spain, **2** A. N. Belozersky Institute of Physico-Chemical Biology, Moscow State University, Moscow, Russia, **3** Department of Pediatrics, University of Pittsburgh School of Medicine and Children's Hospital of Pittsburgh, Diabetes Institute, Pittsburgh, Pennsylvania, United States of America, **4** Neuropathology Division, Department of Pathology, University of Alabama at Birmingham, Birmingham, Alabama, United States of America, **5** Institute of Theoretical and Experimental Biophysics, Pushchino, Russia, **6** Hospital Clinic, IDIBAPS, CIBERES, Universitat de Barcelona, Barcelona, Catalunya, Spain

Abstract

Reactive oxygen species (ROS) produced in the mitochondrial respiratory chain (RC) are primary signals that modulate cellular adaptation to environment, and are also destructive factors that damage cells under the conditions of hypoxia/reoxygenation relevant for various systemic diseases or transplantation. The important role of ROS in cell survival requires detailed investigation of mechanism and determinants of ROS production. To perform such an investigation we extended our rule-based model of complex III in order to account for electron transport in the whole RC coupled to proton translocation, transmembrane electrochemical potential generation, TCA cycle reactions, and substrate transport to mitochondria. It fits respiratory electron fluxes measured in rat brain mitochondria fueled by succinate or pyruvate and malate, and the dynamics of NAD⁺ reduction by reverse electron transport from succinate through complex I. The fitting of measured characteristics gave an insight into the mechanism of underlying processes governing the formation of free radicals that can transfer an unpaired electron to oxygen-producing superoxide and thus can initiate the generation of ROS. Our analysis revealed an association of ROS production with levels of specific radicals of individual electron transporters and their combinations in species of complexes I and III. It was found that the phenomenon of bistability, revealed previously as a property of complex III, remains valid for the whole RC. The conditions for switching to a state with a high content of free radicals in complex III were predicted based on theoretical analysis and were confirmed experimentally. These findings provide a new insight into the mechanisms of ROS production in RC.

Citation: Selivanov VA, Votyakova TV, Pivtoraiko VN, Zeak J, Sukhomlin T, et al. (2011) Reactive Oxygen Species Production by Forward and Reverse Electron Fluxes in the Mitochondrial Respiratory Chain. *PLoS Comput Biol* 7(3): e1001115. doi:10.1371/journal.pcbi.1001115

Editor: Daniel A. Beard, Medical College of Wisconsin, United States of America

Received: April 28, 2010; **Accepted:** February 28, 2011; **Published:** March 31, 2011

Copyright: © 2011 Selivanov et al. This is an open-access article distributed under the terms of the Creative Commons Attribution License, which permits unrestricted use, distribution, and reproduction in any medium, provided the original author and source are credited.

Funding: This work was supported by the European Commission (<http://cordis.europa.eu/fp7>) Diaprepp Health-F2-2008-202013, Etherpaths KBBE-grant n°222639, Synergy, FP7grant n° 270086; the Spanish Government and the European Union FEDER funds (http://ec.europa.eu/regional_policy/funds/feder/index_es.htm) SAF2008-00164 and Instituto de Salud Carlos III; Spanish Ministry of Science and Innovation & European Regional Development Fund (ERDF) "Una manera de hacer Europa" ISCIII-RTICC (RD06/0020/0046); Generalitat de Catalunya-AGAUR, (<http://www.gencat.cat/>) 2009SGR1308 and 2009 CTP 00026; Foundation Marato TV3-042010 (<http://www.tv3.cat/marato/missio>); the National Institutes of Health (<http://www.nih.gov/>)AG 20899 and U01 DK61058-01; and the Department of Defense W81XWH-06-1-0317. The funders had no role in study design, data collection and analysis, decision to publish, or preparation of the manuscript.

Competing Interests: The authors have declared that no competing interests exist.

* E-mail: tav2@pitt.edu (TVV); martacascante@ub.edu (MC)

Introduction

Reactive oxygen species (ROS) are side products of electron transport in the mitochondrial respiratory chain, the principal component of energy transformation in mitochondria. ROS generation starts with the formation of a superoxide radical (O₂⁻) as a result of interaction between molecular oxygen and free radicals, e.g. semiquinone (Q⁻): O₂+Q⁻→O₂⁻+Q [1]. This extremely active compound can be deactivated in cells, mainly through superoxide dismutase [2]. However, H₂O₂ formed in this process can interact with various intracellular compounds to produce ROS. ROS production serves as a metabolic signal [3–5]. However, when released in excess under certain stress conditions such as hypoxia/reoxygenation, ROS can also directly damage cells [6]. This destructive function of the electron transport chain

represents the main problem in organ transplantation [7] and in many systemic diseases, as diverse as Parkinson disease [8] and diabetes [9]. The problem can be so great that in some organisms disruption of the electron transport chain can be a positive factor in increasing lifetime [10].

Although electron transport and coupled ROS production have been the focus of intensive research, important details are still not understood. There is currently debate regarding the relative contribution of various sites of the respiratory chain to overall ROS production [11,12] and the factors that may alter this contribution [13]. The use of specific inhibitors can localize the sites of ROS production, but their contribution under normal and stress conditions without inhibitors *in vivo* is not clear. It is generally accepted that electron transport from succinate through complex I to NAD⁺, the phenomenon known as reverse electron transport

Author Summary

Respiration at the level of mitochondria is considered as delivery of electrons and protons from NADH or succinate to oxygen through a set of transporters constituting the respiratory chain (RC). Mitochondrial respiration, dealing with transfer of unpaired electrons, may produce reactive oxygen species (ROS) such as O_2^- and subsequently H_2O_2 as side products. ROS are chemically very active and can cause oxidative damage to cellular components. The production of ROS, normally low, can increase under stress to the levels incompatible with cell survival; thus, understanding the ways of ROS production in the RC represents a vital task in research. We used mathematical modeling to analyze experiments with isolated brain mitochondria aimed to study relations between electron transport and ROS production. Elsewhere we reported that mitochondrial complex III can operate in two distinct steady states at the same microenvironmental conditions, producing either low or high levels of ROS. Here, this property of bistability was confirmed for the whole RC. The associations between measured ROS production and computed individual free radical levels in complexes I and III were established. The discovered phenomenon of bistability is important as a basis for new strategies in organ transplantation and therapy.

[14], is important for respiration and ROS production [15,16]. However, the mechanism of ROS production as a result of electron transfer upstream in the respiratory chain is not understood. Some details of the general mechanism of electron transport, such as the interaction of complex I with quinones that results in translocation of four protons through the membrane and reduction of one ubiquinone molecule per two electrons transported, remain the subject of discussions [17,18]. Answering these questions will help in understanding the mechanisms of electron transport and coupled ROS production, and will be useful for advances in transplantation and therapy.

The solution to such problems requires not only improvements in experimental techniques and new experiments, but also modification of methods for theoretical analysis. Specifically, kinetic modeling, which is an efficient method for investigating complex systems, still needs to be adopted for the mitochondrial respiratory chain. In fact, kinetic modeling in its classical form has been used for analysis of mitochondrial respiration. However, even the most detailed models [19] could consider only simplified scenarios. Huge number of differential equations is necessary to describe the behavior of respiratory complexes, so an automated procedure is required for their construction. Previously we developed a rule-based methodology for the automated construction of large systems of differential equations for analysis of ^{13}C isotope tracing experiments in metabolic flux analysis [20–22]. We extended this methodology to the mathematical description of multienzyme complexes, specifically mitochondrial respiratory complex III based on a Q-cycle mechanism [23]. A detailed description of complex III operation revealed that in a certain range of parameters complex III has the property of bistability, where two different steady states exist for the same parameters and the system can reach one or the other, depending on its initial state. Perturbations, such as fluctuations in succinate concentrations or temporal hypoxia, can switch the system from low to high ROS producing steady state. Such a switch explains the damaging increase in ROS production on reoxygenation after hypoxia.

The prediction of bistability for the mitochondrial respiratory chain was based on analysis of the Q-cycle mechanism for complex

III. The contribution of other parts of the respiratory chain and linked processes that provide substrates must affect the properties of the respiratory chain. To study mitochondrial respiration as a whole, we extended the model of complex III [23]. The extended model includes the following elements: a detailed mathematical description of complex I; the stoichiometry of electron transport and proton translocation by the respiratory chain; the transmembrane potential; proton leak; oxidative phosphorylation; the TCA cycle that produces NADH and succinate as substrates for complexes I and III; and the transport of TCA cycle metabolites. The objective of this extension to the whole respiratory chain and linked processes was to create a tool for analysis of the basic behavior of the respiratory chain, in particular under conditions defining different fluxes in the forward and reverse directions. The ultimate aim was to reveal characteristics that have not been measured, such as the content of various free radicals, and thus to provide an insight into the relationship between states of the respiratory chain operation and ROS production.

Results

Figure 1 shows the components of the respiratory chain connected in the extended model. Respiratory complexes I to III

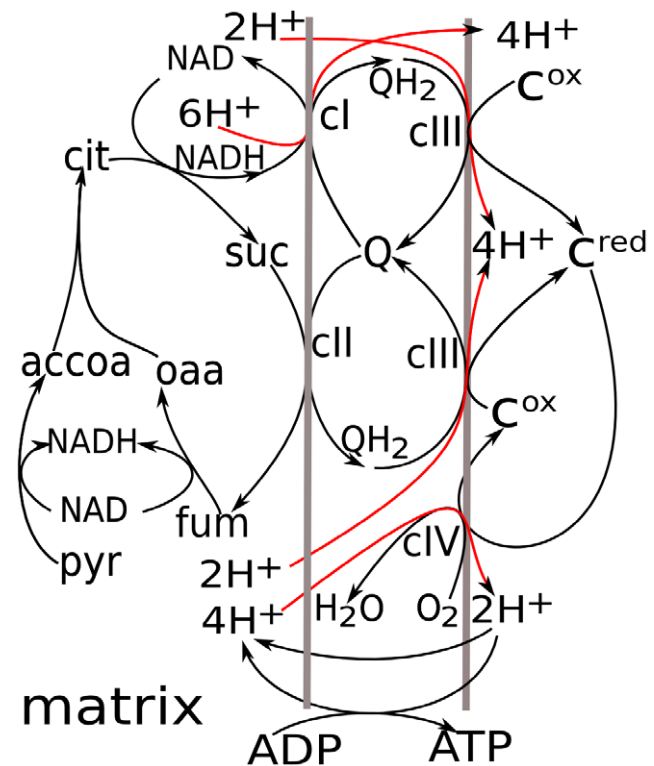


Figure 1. Scheme for mitochondrial respiration and linked processes simulated in the model. Two reactions lead from pyruvate to succinate and further transformation to oxaloacetate reduce NAD^+ to NADH. The latter is used by complex I to generate a transmembrane electrochemical proton potential ($\Delta\mu_{H^+}$) and reduce ubiquinone (Q) to ubiquinol (QH_2), oxidation of which by complex III also contributes to $\Delta\mu_{H^+}$. Complex III reduces cytochrome c, oxidation of which by complex IV and reduction of molecular oxygen to H_2O is also coupled to $\Delta\mu_{H^+}$ generation. Oxidation of succinate to fumarate by complex II is coupled to the reduction of ubiquinone and thus fuels complex III. The product of electron transport, $\Delta\mu_{H^+}$, is consumed for ATP synthesis.

doi:10.1371/journal.pcbi.1001115.g001

are components of the electron transport chain connected through ubiquinone. Complex III is linked to complex IV through reduction/oxidation of cytochrome *c*. NADH, which is a substrate for complex I, is produced in the TCA cycle. Since the total concentration of NAD^+ and NADH is conserved, NADH consumption, which fuels electron transport in the respiratory chain, defines the levels of NAD^+ , which is a substrate for several reactions in the TCA cycle. In this way, the extended model links electron transport with central energy metabolism, in particular with the reactions of the TCA cycle.

Determination of parameters by fitting experimental data

As described in the Methods section, the model of the respiratory chain and linked substrate transport and TCA cycle reactions contains 51 parameters. Out of 22 parameters of complex III, six ratios for forward and reverse rate constants were expressed through midpoint potentials. The order of magnitude for the rate constants for forward electron transport reactions in complex III can be estimated based on previous studies [19]. A qualitative reproduction of measured triphasic dynamics of cytochrome b_{H} reduction by succinate in isolated cytochrome *bc*₁ complex [24], as described in Text S1 and Figures S1, S2, S3 and S4, provides some restrictions for rate constants for binding/dissociation of complex III with ubiquinone species.

The rates of respiration in the presence of ADP (state 3) or an uncoupler characterize the maximal capacity of the respiratory chain. In the absence of ADP (state 4), the respiration rate is characterized by proton leaks, which must be compensated by respiration. According to our measurements, the respiration rate is 480 ± 40 and 170 ± 30 ng atom O/min/mg protein in the uncoupled and in state 4 in succinate-fueled mitochondria, and 410 ± 30 and 80 ± 20 ng atom O/min/mg protein in mitochondria fueled by pyruvate and malate, respectively.

If mitochondria fueled by succinate do not expend the energy of the transmembrane electrochemical potential on ATP synthesis (state 4), succinate oxidation results in fast reduction of intramitochondrial NAD^+ . In the presence of rotenone, an inhibitor of electron transport in complex I, NAD^+ reduction is characterized by NAD^+ -dependent reactions of the TCA cycle and in particular the forward respiratory flux resulting from succinate oxidation. In the absence of rotenone, reverse electron transport [14] also participates in NAD^+ reduction, which makes the process much faster (Figure 2A). These data define the rate constants for reverse electron transport.

While succinate fuels complex III through succinate dehydrogenase, the oxidation of malate and pyruvate in the TCA cycle fuels complex I by reducing NAD^+ to NADH. Respiration under such conditions defines the characteristics of complex I.

To evaluate the model parameters, we used a procedure that simulates all the different types of data listed above for the same set of parameters. The ratio of forward and reverse constants defined by a known midpoint potential or dissociation constant was kept fixed, and the conditions of substrate supply or membrane permeability for protons were changed in accordance with experimental conditions. The procedure fitted all the data by changing the free parameters within the order of magnitude indicated in [19], summarizing and minimizing the deviations in several calculations that simulated measurements. Minimization was performed using a standard stochastic procedure in the global space of parameters as described in Methods.

The best fit reproduces well the dynamics of NAD^+ reduction measured in brain mitochondria in the presence and absence of rotenone using the same set of parameters (Figure 2A). The insets

in Figure 2A show respiration rates and $\Delta\Psi$ in the presence and absence of rotenone. These characteristics remain practically the same in both conditions. Without rotenone inhibition reversible electron flow through complex I, which fits the experimental data shown in Figure 2A, is directed to NAD^+ reduction (is negative) only during a short period of time (Figure 2B), although ROS are constantly produced for a much longer time under such conditions [15,25]. Reverse electron flow is believed to induce excessive ROS production, but evidently these two processes are not correlated.

Rotenone essentially changes the dynamics of NADH measured before succinate addition. It is slightly oxidized by the RC in the absence of rotenone, but slowly reduced in its presence. This reduction is a result of oxidation of internal substrates while electron flow through the RC is blocked. We found that the metabolites of TCA cycle cannot be substrates that provide NADH reduction, because oxidation of TCA cycle metabolites results in much faster initial reduction of NADH. If the parameters of TCA reactions are changed to slow down and reproduce the initial dynamics of NADH, maximal respiration rate with pyruvate becomes inconsistent with experimental data (not shown). Rather, slow oxidation of other metabolites, probably aminoacids or lipids, contributes to NADH reduction. The simulation of such slow oxidation did not prevent NADH oxidation in the absence of rotenone, and reproduced NADH reduction in its presence.

While, in the absence of rotenone, succinate induced much faster NADH reduction due to reverse electron transport, the steady state levels are lower than in the presence of rotenone. The steady state levels are defined by NADH production and consumption in respiration. Rotenone blocks the consumption, therefore NADH levels further increase when rotenone is added after succinate. The model parameters were adjusted without considering subsequent NADH increase and the reproduction of this phenomenon validates the model.

The model reproduces measured maximal and state 4 respiratory electron flows for succinate-fueled mitochondria, as well as for mitochondria fueled by pyruvate/malate (Figure 2C). The change in $\Delta\Psi$ in the same simulations qualitatively corresponds to known changes measured under such conditions (Figure 2D). The parameters for simulations shown in Figure 2 are listed in Table 1 (column indicated as best fit).

These simulations of measured data provide an insight into important hidden characteristics, such as the capacity of ROS production. ROS are produced by the respiratory chain as a consequence of one-electron transfer directly to oxygen from free radicals of electron transporters such as the semiquinone radical (SQ) at the Q_o site in complex III [26–28] or FMNH [29], SQ bound to complex I [30], or N_2 centers [30] in complex I. Simulating the experimental data as presented in Figure 2 the model at the same time simulates the dynamics of these free radicals.

Qualitative analysis of associations between the overall ROS production and individual radicals

The model describes various states of respiratory complexes formed in the process of electron transport, including those containing free radicals. Such radicals could be responsible for passing unpaired electrons to oxygen thus forming superoxide radicals and other forms of ROS. The contributions of various radicals to ROS production remain unknown; to clarify it we compared measured ROS production and the levels of various free radicals predicted by the model for the same conditions. A similar change in radical content and measured ROS production indicates qualitative accordance between the model and the described process and thus validates the model.

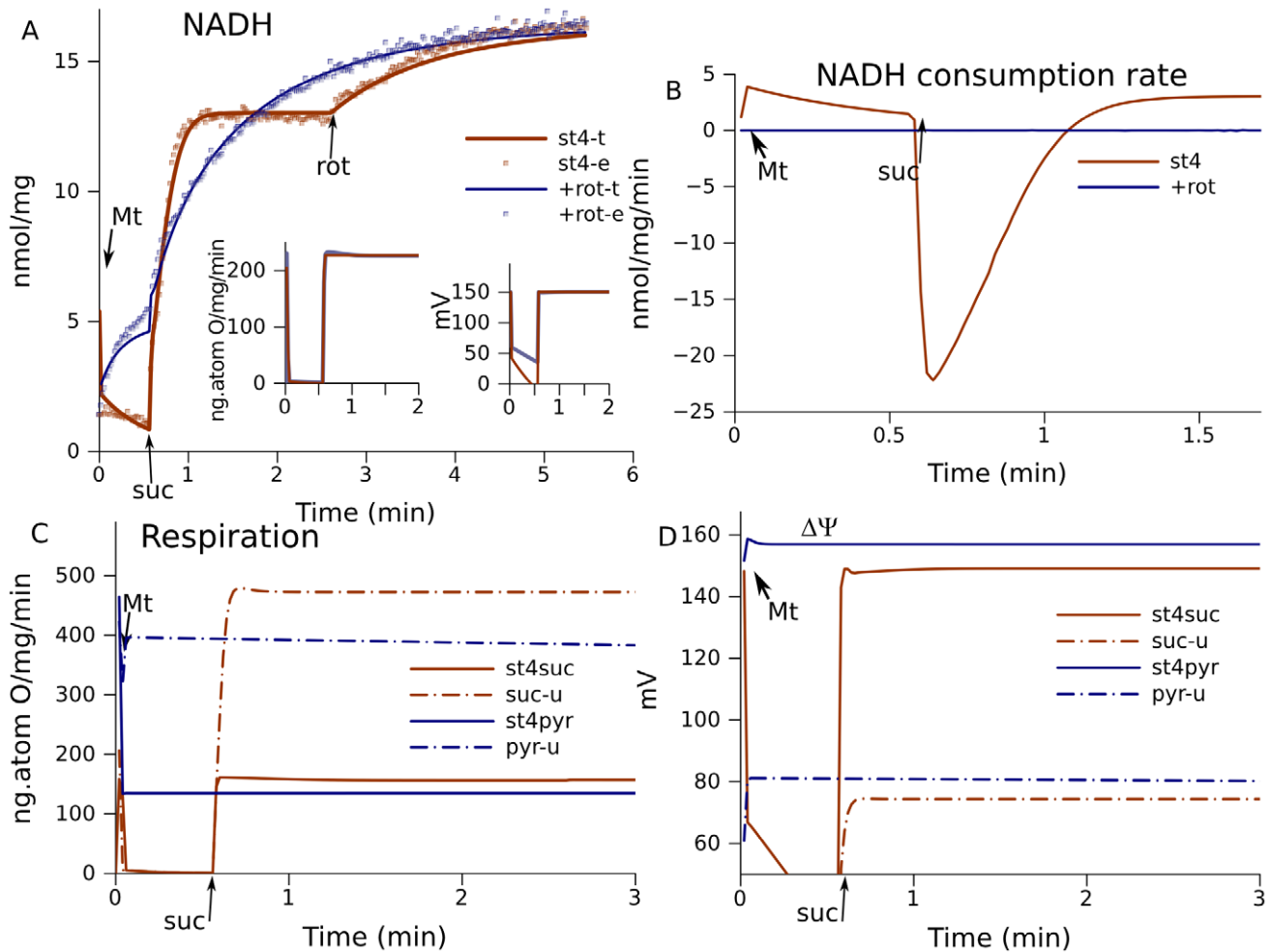


Figure 2. Simulation of forward and reverse electron flows in the respiratory chain. (A) NADH reduction in state 4 in the absence (st4) and presence of rotenone (+rot). Points are experimental data (–e) measured in brain mitochondria fueled by 1 mM succinate, lines are calculated (–t). (B) Reversible electron flow through complex I computed in the simulations shown in (A). (C) Respiration (net forward flux to oxygen) and (D) $\Delta\Psi$ under different substrate conditions (suc, 1 mM succinate; or pyr, 1 mM malate and 1.5 mM pyruvate). State 4 respiration (st4) was simulated using the parameters described in Methods. The action of rotenone was simulated by setting $k_{f15} = k_{r15} = 0$ (rate constants for N2–ubiquinone interactions). The maximal respiration rate (–u, uncoupled) was simulated by setting a high proton leak ($k_{lk} = 50000 \text{ s}^{-1}$). Arrows denote the time of additions of mitochondria (Mt, usually at time 0), succinate (suc), and rotenone (rot) if they are not present in the medium before mitochondria. doi:10.1371/journal.pcbi.1001115.g002

It is generally known that inhibition of reverse electron transport by rotenone decreases ROS production in succinate-fueled brain mitochondria [15,28]. In our measurements, ROS accumulation was inhibited immediately after rotenone addition (Figure 3A). The model predicts that the SQ content at site Q_o in complex III in succinate-fueled mitochondria is practically unchanged by the presence of rotenone (Figure 3B) and this remains valid for simulations with any set of parameters describing the data well. This is the reason for the coincidence of intervals for SQ at Q_o for the first two types of simulation shown in Table 1. Thus, the ROS-stimulating role of reverse electron transport and the ROS-inhibitory effect of rotenone cannot be explained at the level of complex III. Apparently, reverse electron flow mainly affects complex I by increasing the concentrations of free radicals able to pass electrons to oxygen.

The model predicts that rotenone essentially decreases initial levels of SQ bound on site Q_n (Figure 3C), FMNH (Figure 3D), and the content of reduced N2 centers (inset). After an initial decrease, levels of SQ and FMNH increase, in agreement with the acceleration of ROS production measured after initial inhibition

induced by rotenone (Figure 3A). The reason for accumulation of free radicals and acceleration of ROS production is the production of malate from succinate, which then reduces NAD^+ in malate dehydrogenase reactions. This supply of substrate for complex I increases ROS production in rotenone inhibited mitochondria. The increase in the rate constant for malate–succinate exchange eliminates a slow increase in free radical content when rotenone is present (dashed curve in Figure 3C and D). It should be noted that the acceleration of ROS accumulation is not always observed experimentally and this agrees with the predicted disappearance of this slow component after acceleration of malate-succinate exchange. Such similarity of experimental and simulated behavior supports the mechanism accepted for its simulation and in this way validates the model.

The fact that the species of complex I can contain more than one radical makes it more difficult to understand the contribution of each site. In particular, the species 1101001 (the positions of digits correspond to Q_p - Q_p - Q_n - Q_n -N2-FMN-FMN), which contain SQ and FMNH radicals, slowly accumulate after inhibition by rotenone. This accumulation defines the dynamics

Table 1. The 99% confidence intervals of parameters and levels of free radicals.

	max	min	bestfit
k_{qp_FS}	267000	117000	200000
k_{FS_c1}	1585000	305000	527000
k_{qp_bl}	121000	25000	37000
k_{bl_bh}	114000	17000	27000
k_{bh_qn1}	214000	32000	47000
k_{bh_qn2}	1118000	225000	254000
k_{qHbnd}	4000	1700	2800
k_{qnbnd}	23000	5000	7200
k_{qpdis}	9500	1700	2300
k_{qhnds}	9500	3300	4100
k_{c1c}	290	240	260
k_{fl0}	724000	460000	640000
k_{fl1}	525000	138000	140000
k_{fl2}	816000	255000	770000
k_{fl3}	34500	15000	23000
k_{fl6}	360000	138000	164000
k_{fl8}	721000	143000	205000
k_{fl7}	340000	148000	187000
k_{tca}	1600	650	710
k_{MDH}	1100	270	460
k_{spe}	340	140	270
k_{me}	0.000382	0.000064	0.000280
k_{pyrin}	1200	500	600
k_{sfe}	8.5	2.11	6.48
k_{cs}	1300	500	1290
SQ@Qo			
st4-suc	0.23318	0.07607	0.16491
+rot	0.23310	0.07602	0.16482
st4-pyr	0.01808	0.01615	0.01756
SQ@Qn			
st4-suc	0.12456	0.11350	0.06705
+rot	0.07607	0.06562	0.07120
st4-pyr	0.01293	0.00556	0.00835
FMNH			
st4-suc	0.00486	0.00407	0.02525
+rot	0.04094	0.02176	0.03152
st4-pyr	0.00702	0.00284	0.00439
N2			
st4-suc	0.135	0.12507	0.07098
+rot	0.07407	0.06320	0.06914
st4-pyr	0.00723	0.00327	0.00482

These intervals were calculated for each parameter separately among the sets of parameters that give χ^2 below than a fixed threshold [31]. The sets of parameters were found using a stochastic optimization algorithm (Simulated annealing) that minimized the deviation from measured dynamics of NAD+ reduction in the presence and absence of rotenone, and uncoupled and state 4 respiration rates. Only forward rate constants are shown assuming that the reverse constants change proportionally keeping constant the ratio in accordance with respective ΔE_m or dissociation constant. The units for rate constants of monomolecular electron transport are s^{-1} . For the reactions where protons are bound the concentration of protons for pH=7 is included in the constant ($k' = k \cdot [H^+]^2$). These values have the same units s^{-1} . Dissociation rate constants are also expressed in the same units. Since concentrations are

Table 1. Cont.

expressed in nmol/mg prot, rate constants for the bindings are expressed in $s^{-1} \cdot (nmol/mg \text{ prot})^{-1}$.
doi:10.1371/journal.pcbi.1001115.t001

of SQ and FMNH, whereas 1101100 defines the fast component in levels of Qn-bound SQ and reduced N2 (inset in Figure 3D). It is possible that only one of coupled radicals makes the major contribution to ROS production, but in this case the levels of other radicals would also correlate with ROS production. On the other hand, radicals situated inside the same species could interact, so that the specie as a whole produce superoxide. In the considered example the behavior of the whole ensemble of radicals in complex I agrees with the observed effect of rotenone, and this validates the model.

Overall, according to the model predictions, rotenone hardly affects SQ levels in complex III, but initially it significantly decreases the levels of free radicals produced in complex I; this is the reason for the decrease in ROS production induced by rotenone in succinate-fueled mitochondria. The model also explains the subsequent increase in ROS production as a result of the formation of malate in rotenone-inhibited mitochondria.

Rotenone induces a large increase in ROS production in pyruvate/malate-fueled mitochondria (Figure 4A). The corresponding simulations show that rotenone greatly increases the levels of FMNH and SQ at Qn site, but decreases the levels of reduced N2 (Figure 4B). Since the changes in N2 disagree with measured ROS production, probably N2 center does not make essential contribution in ROS production under the considered conditions. The same species (1101001) that defined the slow component in the increase in free radicals now change faster and defines the main part of the response to rotenone. Species 1101100 also constitute an essential part of the total radical content, but their levels decrease in response to rotenone in accordance with the decrease of total N2 radical levels.

Stimulation of electron transport by addition of ADP or an uncoupler such as FCCP to succinate-fueled mitochondria results in a decrease in ROS production (Figure 5A). This generally known phenomenon [15] validates the model prediction that the levels of all free radicals decrease when electron transport is stimulated by addition of ADP or an uncoupler.

Mitochondria fueled by pyruvate/malate also produce less ROS when electron transport is stimulated by an uncoupler (Figure 6A). Such measurements also validate the model, which predicts a decrease in the levels of free radicals (Figure 6B).

At high succinate concentrations, brain mitochondria produce much more ROS than those fueled by pyruvate (Figure 7A). The model also predicts higher levels of free radicals in complex III, as well as in complex I, for mitochondria fueled by succinate (Figure 7B).

Thus, the study of associations between measured ROS production and predicted radical levels in RC revealed qualitative consistency of measurements with all types of radicals and therefore validated the model, or showed a way of discrimination between possible sites of ROS production, and even between possible ROS producing species. However, in the latter case, a special, quantitative study is needed, which currently is beyond of the scope of presented study.

Prediction of bistability for the whole respiratory chain

It has been predicted that the Q-cycle mechanism of complex III can in principle induce bistable behavior [23]. The whole

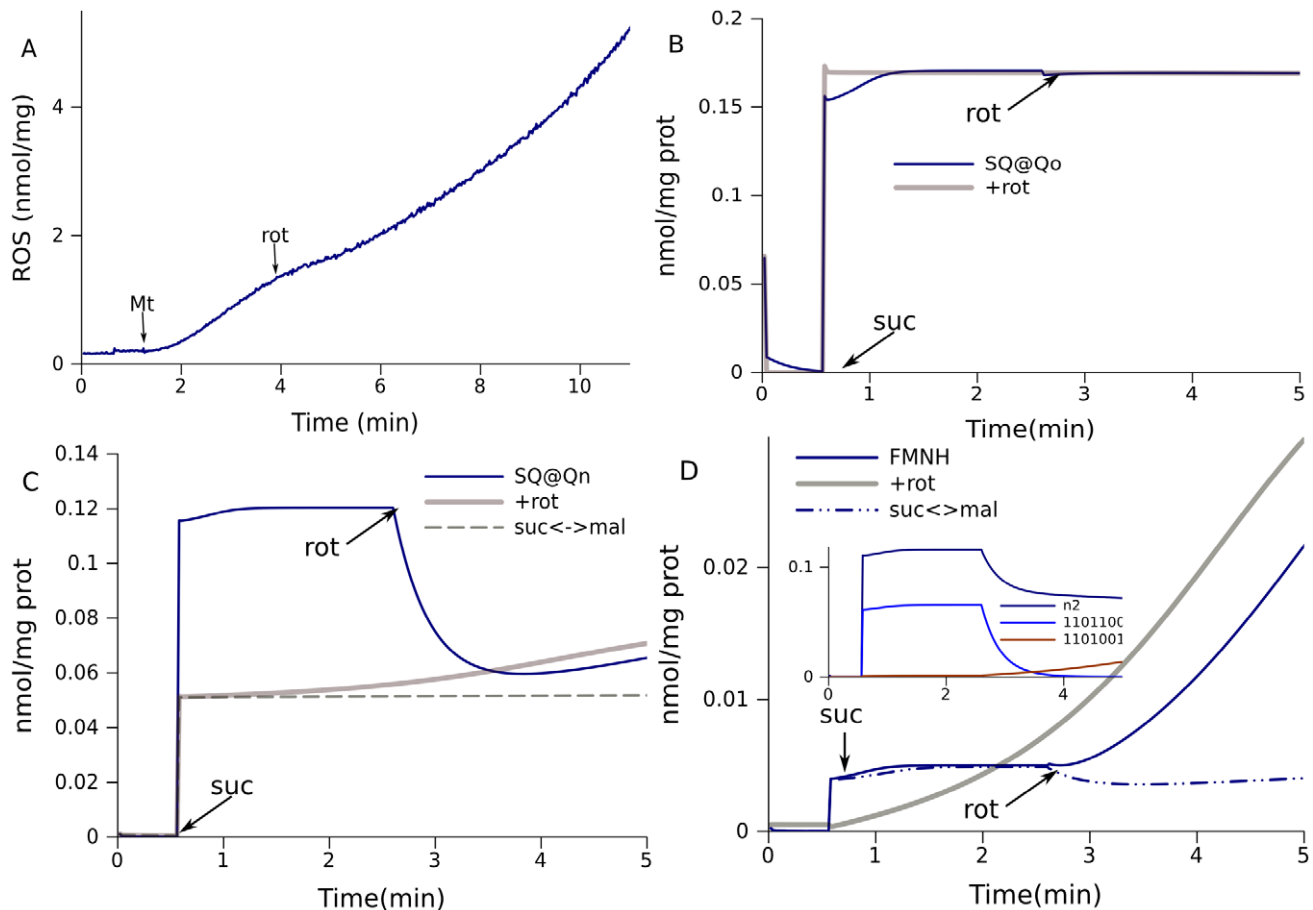


Figure 3. Effect of rotenone on ROS production in mitochondria fueled by 0.5 mM succinate. (A) ROS production measured. (B–D) Model prediction of the content of various free radicals. The dynamics of (B) SQ bound to Qo sites of complex III, (C) SQ at Qn sites of complex I and (D) FMNH were taken from the same simulations of state 4 respiration in succinate-fueled mitochondria for rotenone addition (+rot), either initially or in the course of measurements, as in Figure 2. The simulation marked suc<->mal had a tenfold increased rate constant for this exchange. The inset in (D) shows the dynamics of N2 radicals and species 1101100 and 1101001 for rotenone addition (the digit positions correspond to Qp-Qp-Qn-Qn-N2-FMN-FMN; 1 denotes reduced and 0 oxidized). Arrows indicate the time of additions of mitochondria (Mt), succinate (suc) and rotenone (rot). doi:10.1371/journal.pcbi.1001115.g003

respiratory chain considered here, with the parameters that fit the experimental data, also has two different steady states for the same parameters. Figure 8A shows that the SQ content at site Qo in complex III could persist at different values, depending on whether the respiratory chain is initially reduced or oxidized. Figure 8B shows how the steady states for free radicals of complexes I and III change with the external succinate concentration for a set of parameters that reproduces the experimental data described above.

With increase in succinate concentration at some point the system switches to the state with the highest levels of semiquinone radicals at Qo site of complex III. The difference here from the similar curve in Figure 7 is that pyruvate is present in addition to succinate. Once the system is switched to the state of highest SQ content at Qo, it remains in this state even if the succinate concentration decreases back to low values. Thus, if the system is initially in an oxidized state, the steady state SQ levels at Qo depend on the succinate concentration, in accordance with the blue curve in Figure 8B. If the system is initially in a reduced state, it remains in this state until succinate concentrations decrease to the micromolar range. Since complex III is directly connected to complex I through a common substrate (ubiquinone), the bistable behavior of complex III induces bistability in complex I. However,

when complex III enters the state with high SQ levels at Qo, SQ levels at Qn decrease (Figure 8B), as well as the levels of other free radicals in complex I (not shown). In some range of succinate concentrations total amount of radicals in the two presented steady states can be similar, but this does not necessary means similar ROS production in the two states since the probability of ROS production can be different for various radicals.

Thus, bistable behavior remains valid for the extended model of the RC with proton translocation and transmembrane potential ($\Delta\Psi$) generation, and with parameters defined by fitting the experimental data and validated by qualitatively similar predicted and measured ROS production. The model predicts also that a pulse of succinate is associated with decrease of $\Delta\Psi$. Such counterintuitive decrease of $\Delta\Psi$ induced by increase of substrate for respiration is shown in Figure 9A. The value of $\Delta\Psi$ decrease, induced by the same pulse of succinate, can be different, depending, for instance, on membrane leak, as illustrated by two curves in Figure 9A. Measurements of $\Delta\Psi$ using safranin O fluorescence revealed that the mean $\Delta\Psi$ at low succinate (0.2 mM) is greater than at high succinate (2 mM) (Figure 9B), thus validating the paradoxical prediction of the model.

The succinate threshold for a switch to the reduced state depends on the parameters of pyruvate transport and TCA

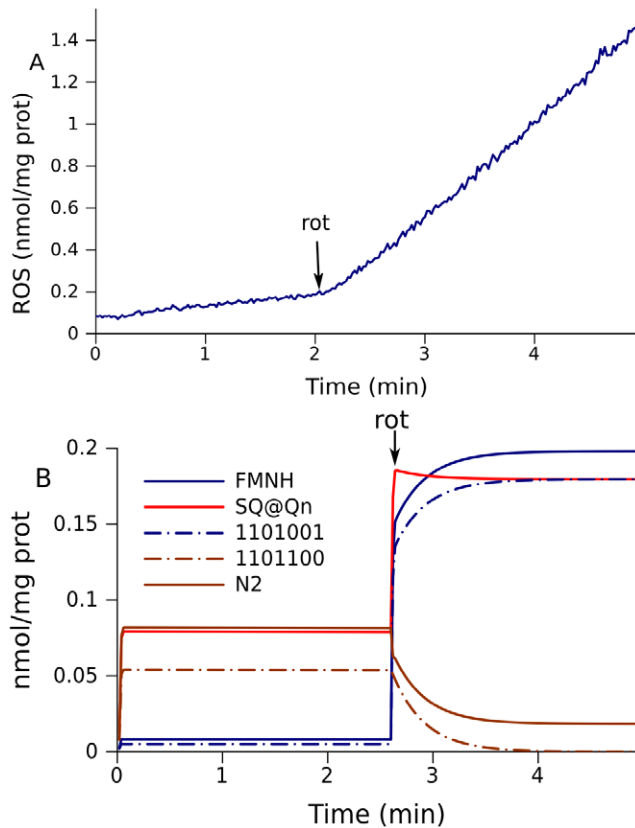


Figure 4. Effect of rotenone on ROS production in mitochondria fueled by 5 mM pyruvate and 5 mM malate. (A) ROS production measured in state 4 respiration and the change on addition of rotenone. (B) Model prediction of free radical levels in a simulation of the conditions for (A). The model parameters are the same as for the simulation shown in Figure 2. doi:10.1371/journal.pcbi.1001115.g004

reactions; here we do not investigate the quantitative details with respect to bistability, but emphasize only the qualitative similarity of predicted and measured behavior. With regards to the considered in the previous sections normal “working” steady state, the predicted levels of free radicals are robust with respect to the model parameters, as the next section shows.

Sensitivity to parameters and robustness of the model predictions

The sensitivity of simulations to variations in model parameters is shown in Table S1 for each type of experimental data presented in Figure 2 (dynamics of NAD^+ reduction, maximal and state 4 respiratory fluxes). The sensitivity is also listed for simulated levels of free radicals shown in Figure 3. The results indicate that significant changes in some parameters hardly affect the simulations (e.g. $k_{\text{qp-FS}}$). Evidently, the data do not restrict the parameter values and they could not be defined unambiguously. However, changes in these parameters within the range, for which fitting remains good, do not affect the predictions in terms of free radical levels. The parameters shown in red highly affect the simulations. However, it is possible that different combinations of such parameters could fit the measured data equally well because of mutual compensatory changes. In this case, despite the high sensitivity, the parameters can have a wide range of values for which a good fit is obtained. Confidence intervals rather than sensitivity are used to characterize the robustness of parameter determination.

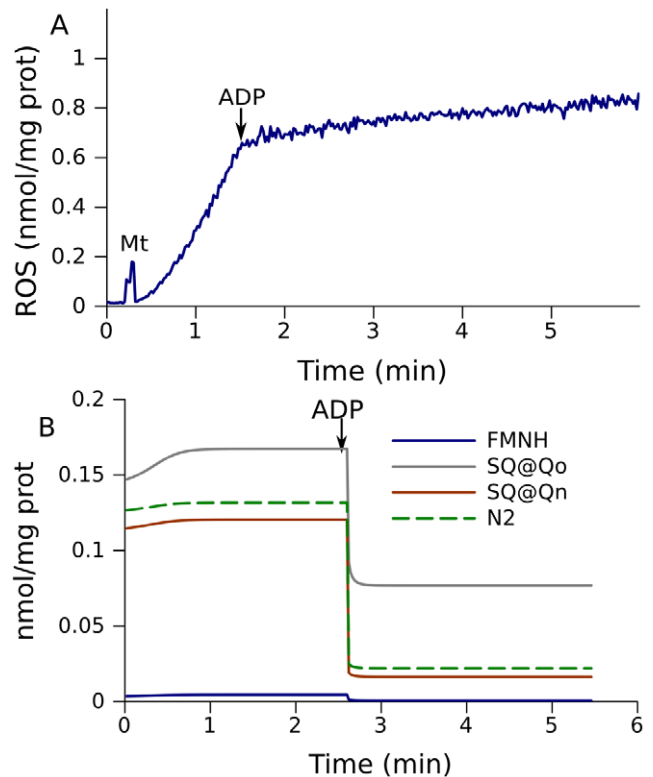


Figure 5. Effect of acceleration of electron transport on ROS production in mitochondria fueled by 3 mM succinate. (A) ROS production measured in state 4 and the change on addition of 1 mM ADP. (B) Model prediction of free radical content. The dynamics of free radical levels in a simulation of the conditions for (A). The model parameters are the same as for the simulation shown in Figure 2. doi:10.1371/journal.pcbi.1001115.g005

Different sets in the global space of parameters that fit the experimental data could be identified using our stochastic algorithm for minimization of the objective function χ^2 (sum of squares of deviations from measured data normalized by standard deviations). The algorithm identified confidence intervals for parameters based on fixed thresholds of χ^2 [31].

Table 1 shows the 99% confidence intervals for the free parameters. The ranges for which the values give a good fit to the data are large. Thus, even though the measurements cover various modes of respiratory chain operation, the data do not restrict the parameters sufficiently to define them unambiguously. Various sets over a wide range of parameters can describe the data equally well. However, the situation is different for free radical levels predicted for the simulated experimental conditions. Table 1 lists intervals for predicted free radical levels simulated using the parameters sets that fit the data with χ^2 that is below the threshold. The confidence intervals for free radical levels are generally much narrower, so the predicted values are more robust. Although the intervals for SQ at Q_o sites in succinate-fueled mitochondria are relatively large, they are clearly almost the same for both conditions (with or without rotenone). This result agrees with data indicating that the SQ content at Q_o practically shows no dependence on the presence of rotenone (Figure 3B). The levels of all free radicals in complex I under the conditions for the first two simulations are very robust, despite the high parameter variability. If the parameters give a good fit, the model predicts similar levels of complex I radicals. Although the intervals are relatively large under the third condition (pyruvate/malate supply), it is evident

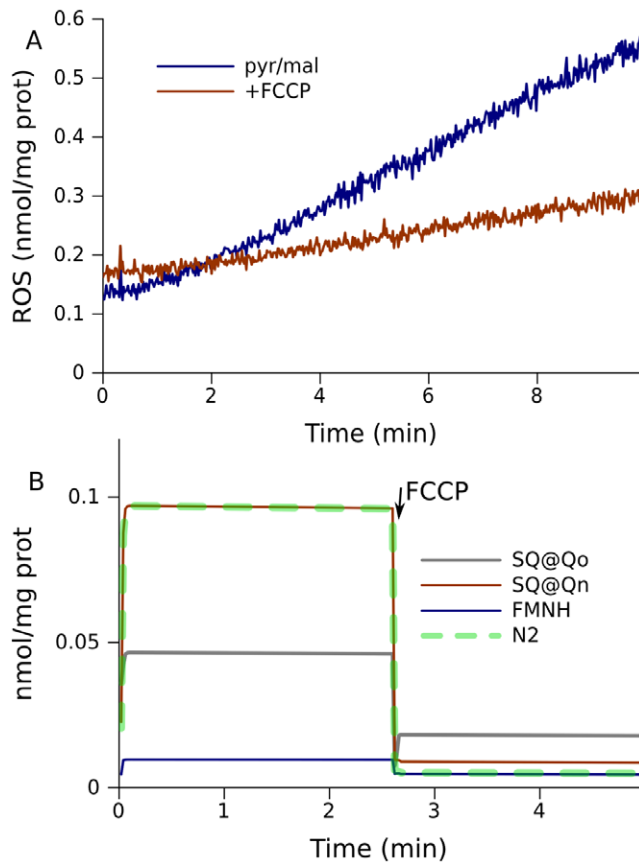


Figure 6. Effect of stimulation of electron transport on ROS production in mitochondria fueled by 5 mM pyruvate and 5 mM malate. (A) ROS production measured in state 4 and in the presence of uncoupler FCCP. (B) Model prediction of free radical content on addition of FCCP. The model parameters are the same as for the simulation shown in Figure 2. doi:10.1371/journal.pcbi.1001115.g006

that they are much lower than the intervals for the condition of succinate supply, as well as the levels of radicals in complex III.

Discussion

To construct a detailed mathematical model that accounts for all redox states formed during electron and proton transport in complexes III and I, we used our rule-based methodology for automated construction of large systems of ODE [23]. This model further extends our methodology previously used to model the distribution of ^{13}C isotopes in central metabolism [20–22], development of which occasionally coincided in time with that of similar rule-based methodology for signal transduction pathways [32,33]. For the study of mitochondrial processes our methodology gives a deep insight into the mechanics of respiration and ROS production. Here, rule-based algorithms for mathematical description of mitochondrial respiration coupled to proton translocation and $\Delta\Psi$ formation was linked to a classical kinetic model that accounts reactions of the TCA cycle, which provides succinate and NADH as substrates for respiration and substrate transport in mitochondria.

After fixing the ratios of forward and reverse rate constants for electron transport reactions, free parameters were defined by fitting of forward and reverse electron flows measured under various conditions. High variability of parameters with a good fit

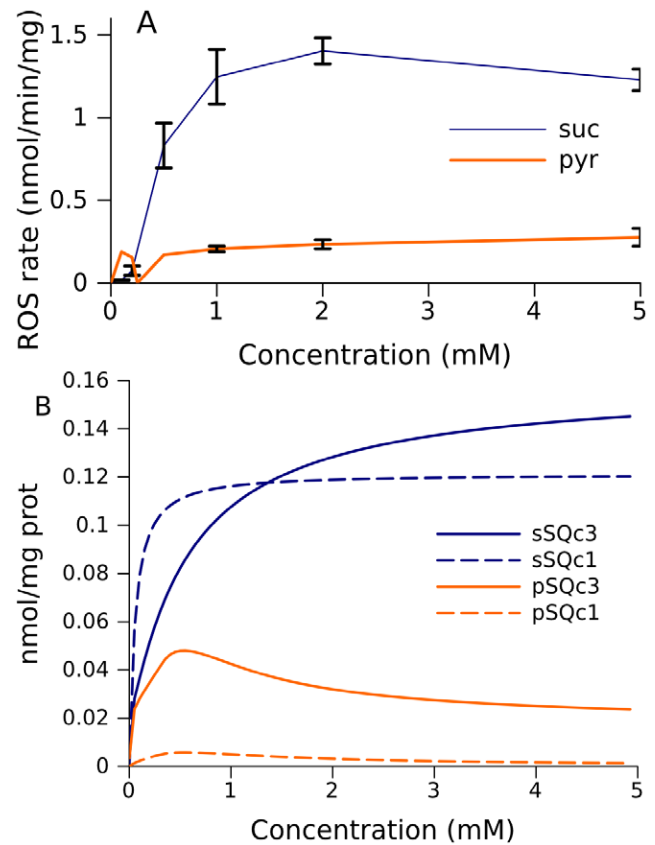


Figure 7. Substrate dependence of ROS production and levels of free radicals. (A) ROS production measured in brain mitochondria. (B) Predicted levels of free radicals in complexes I and III. Succinate (blue curves) or pyruvate (orange) was used as substrate. Semiquinone levels in complexes I (c1) and III (c3) are presented as indicators of ROS production. doi:10.1371/journal.pcbi.1001115.g007

to experimental data precluded definition of their values. However, the levels of free radicals calculated in the model showed much less variability. Different sets of parameters with a good fit to experimental data define very similar patterns for free radicals formed in complexes I and III. Thus, the analysis gives a valid insight into the mechanism of respiration and ROS production, even without precise evaluation of the model parameters.

A substantial body of experimental data on mitochondrial ROS production cannot be satisfactorily explained within the current experimentally based paradigm. Some of these results were obscure, such as acceleration of succinate-driven ROS production after initial inhibition by rotenone (Figure 3). Others, such as a lower membrane potential in mitochondria fuelled by higher succinate concentration (Figure 9), were even counterintuitive. Calculation for mitochondrial constituents not measurable by current techniques represents a powerful tool for mechanistic explanation of accumulated data and for directing experimental research to test model predictions.

A body of evidence indicate that either FMNH [29,30], or SQ bound to Qn sites of complex I [30], or reduced N2 centers [30,34,35] may be a major contributor to ROS production, depending on the tissue, substrate, energy demand and oxygen tension [36,37]. The simulations revealed correlations between measured ROS production rates and levels calculated for each type of free radical. In this first step of the study we did not assume

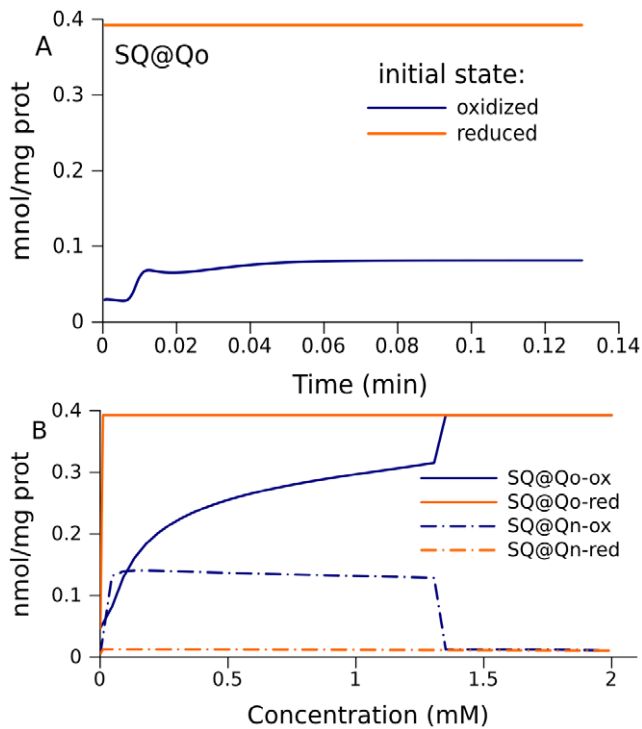


Figure 8. Bistable behavior of the respiratory chain. (A) Predicted dynamics of semiquinones bound to the Qo site of complex III when the system is initially in an oxidized or a reduced state. Substrate concentrations: succinate 0.1 mM, pyruvate 0.25 mM. (B) Steady-state levels of semiquinones bound at the Qo site of complex III and the Qn site of complex I as a function of succinate concentration. The pyruvate concentration for the blue curve is 0.1 mM. doi:10.1371/journal.pcbi.1001115.g008

any explicit link between any specific radical and ROS, but qualitatively compared all of them, taken separately, with measured ROS production. However, the method, which we use, opens a direction for future studies of quantitative contribution of various radicals of electron transporters, and even specific species of complex I and III, into total ROS production.

The similarity between changes in the ROS production rate and in the levels of specific free radicals validates the model and also provides an insight into the mechanism of ROS production. Rotenone inhibition of ROS production in succinate-fueled mitochondria correlated with the free radicals formed in complex I, but not in complex III. Evidently, under the given conditions, reverse electron transport must contribute to free radical formation in complex I, although the net flux reducing NAD^+ through complex I exists for only a very limited period of time.

In accordance with our previous study that revealed bistability for complex III [23], the extended model confirms the existence of two steady states for the same set of parameters. In one of these states (oxidized), mitochondria can develop a maximal rate of respiration, $\Delta\Psi$, and a capacity for ATP synthesis. This is the usual working state. In the presence of pyruvate high succinate concentrations can induce a switch of respiration to the reduced steady state, where lack of electron acceptors strongly restricts electron flow. The levels of free radicals in complex III greatly increase in this state, but decrease in complex I, in contrast. The switch to a more reduced state results in $\Delta\Psi$ decrease. Indeed, we observed a $\Delta\Psi$ decrease in isolated mitochondria in conjunction with an increase of succinate concentrations in the presence of pyruvate.

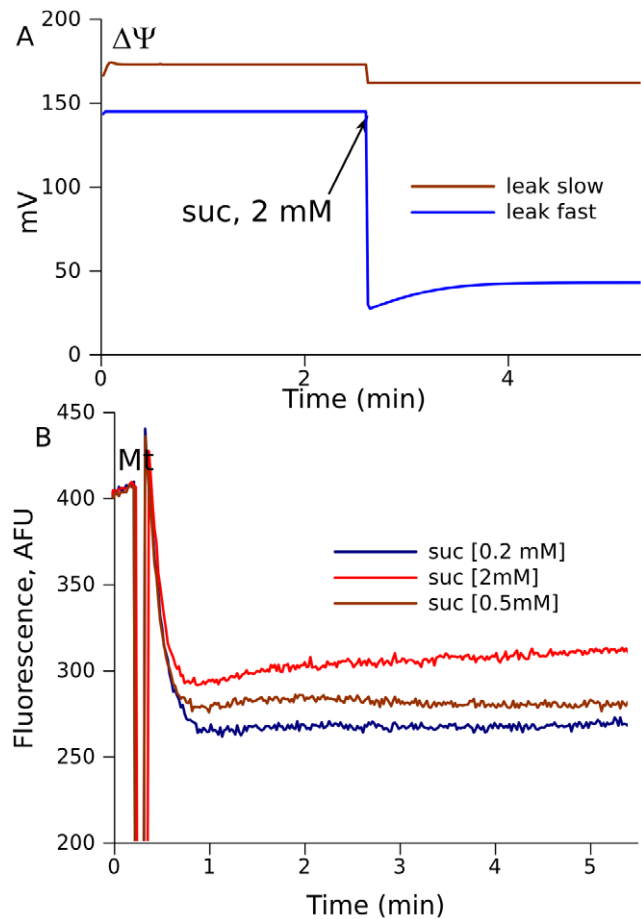


Figure 9. Decrease in $\Delta\Psi$ on transition from the oxidized to the reduced state. (A) Predicted dynamics of the transition induced by addition of 2 mM succinate to mitochondria initially in the oxidized state in the presence of 5 mM pyruvate, under the conditions of various proton leaks through the inner membrane, slow leak, $k_{ik}=17000$, and fast leak, $k_{ik}=80000$ mL/(s·mg prot) (eq.H.1). (B) $\Delta\Psi$ measured as safranin O fluorescence (lower values correspond to higher $\Delta\Psi$) at various succinate concentrations (as indicated). The initial levels of fluorescence (~ 400 AFU) is slightly increased in the moment of addition of mitochondria and, then, energization and uptake of the dye results in decrease of fluorescence. The initial levels after the addition of mitochondria correspond to deenergized mitochondria and final corresponds to maximally energized mitochondria. doi:10.1371/journal.pcbi.1001115.g009

Q-cycle mechanism of complex III operation assumes bifurcation of electron flow at Qo site: one electron goes to Rieske center and further to complex IV, and another one reduces cytochrome b. This bifurcation of electron flow underlies the bifurcation between the two steady states. If in some moment the rate of first electron transition to Rieske center is higher than that for the second electron (because cytochrome b is reduced), semiquinones at Qo accumulate, thus preventing Qo liberation, binding and oxidation new molecules of ubiquinol, and thus limiting electron flow. In the case, shown in Figure 9A, greater proton leak resulted in greater transient discrepancy between the two electron flows at the point of bifurcation, which ultimately led to more significant inhibition of respiration and deeper descent of $\Delta\Psi$.

The decrease of $\Delta\Psi$, in the case shown in Figure 9B, is relatively small, however, in living cardiomyocytes a much higher decrease of $\Delta\Psi$ can be observed, accompanied by high ROS production, and associated with mitochondrial permeability transition (MPT) [38].

Although the presented study does not touch a possible link between bistability and MPT, it puts forward some hypotheses, which verification in future can essentially clarify the mechanism of MPT. There are at least two phenomena, which do not find appropriate explanation in terms of current state of knowledge. First, the increase of permeability in this process does not increase electron flux and proton recirculation, as in case of uncouplers. Second, ROS production is high despite the decrease of $\Delta\Psi$. If we assume that the switch into the reduced state precedes MPT, both phenomena would find a natural explanation. This hypothesis, although not proved yet, opens avenues for deeper investigation of the MPT mechanisms.

The presented new insight into mitochondrial respiration was possible due to the application of novel methodology of modeling that allowed a detailed mathematical description of mitochondrial respiration. The phenomenon of bistability, predicted based on this methodology, has a potential to be a basis of new paradigm for the mechanism of ROS production, which will initiate new research with outcome on academic and practical levels.

Methods

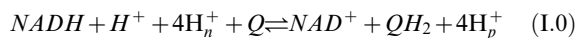
The file executable in Linux, which runs the simulations, and the C++ code of the program could be downloaded free from http://www.bq.ub.es/bioqint/ros_model/plcb2010.cpp.tar.gz.

Electron transport in complex III reflected in the model

The model of complex III described elsewhere [23] was used as a part of the extended model presented here. For each reaction two values, forward (K_f) and reverse (K_r) rate constants, were used as parameters. The order of magnitude of K_f was set based on [19] and then K_r was determined as described in [23] using midpoint electrochemical potentials, which determinations was variable and allowed refinement by fitting the data presented in “Results”. Table 2 summarizes the reactions and values of parameters for complex III that simulate the data.

Electron transport in complex I reflected in the model

The overall process catalyzed by complex I is oxidation of NADH coupled with ubiquinone reduction and pumping 4 protons from negative to positive side of the membrane:



This is a complex process that involves electron transport through a chain of intermediates coupled with proton translocations through inner mitochondrial membrane. The structure and mechanism of catalysis of complex I is reviewed in [39] and the data from this review are used for the construction of model of complex I.

It is assumed that proton translocation is a result of Q reduction (with proton binding) at the negative side and its oxidation (and proton release) at the positive side. If several protons are translocated per one electron, then this electron must pass several cycles of Q reduction and oxidation. Such mechanism, similar to that accepted for complex III, called Q-cycle, was suggested for complex I (see e.g. [17]). We constructed a model based on electron cycling that is in accordance with the measured stoichiometry of proton translocations per one electron passed through the chain.

The initial step of such transport is the oxidation of NADH coupled with the reduction of FMN; further, electrons from FMN pass through a relay of eight different iron-sulfur (Fe-S) containing centers [40], which possibly form a relay for electron transport from FMN to the last Fe-S center N2 (see e.g. the review [40,41]). The Fe-S centers have similar midpoint potential close to that for FMN ($E \sim -350$ mV) with an exception of N2, which is much

Table 2. Reactions and rate constants for complex III.

Electron transport					
1,Qo: $Fe^{3+}+QH_2 \leftrightarrow Fe^{2+}+Q^-+2H^+$					
k_{qp_FS}	200000	ΔE	50	k_{rqp_FS}	28000
2,c1: $Fe^{2+}+c_1^{ox} \leftrightarrow Fe^{3+}+c_1^{red}$					
k_{FS_c1}	528000	ΔE	33	k_{rFS_c1}	143000
3,Qo: $Q^-+b_L^{ox} \leftrightarrow b_L^{red}+Q$					
k_{qp_bl}	90000	ΔE	80	k_{rqp_bl}	4000
4,b: $b_L^{red}+b_H^{ox} \rightarrow b_H^{red}+b_L^{ox}$					
k_{bl_bh}	80000	ΔE	119	k_{rbl_bh}	900
5,Qi: $Q+b_H^{red} \rightarrow Q^-+b_H^{ox}$					
K_{bh_qn1}	100000	ΔE	29	K_{rbh_qn1}	33000
6,Qi: $Q^-+b_H^{red}+2H^+ \leftrightarrow QH_2+b_H^{ox}$					
k_{bh_qn2}	250000	ΔE	50	k_{rbh_qn2}	25000
7,c1: $c_1^{red} \rightarrow c_1^{ox}$					
k_{c1c}	260				
Binding - dissociation					
8,Qo: $Qo+QH_2 \leftrightarrow QH_2@Qo$					
k_{qHbnd}	3700			k_{rqHbnd}	2600
9,Qi: $Qi+Q \leftrightarrow Q@Qi$					
k_{qnbnd}	7000			$k_{rqnbnnd}$	200
10,Qo: $Q@Qo \leftrightarrow Qo+Q$					
k_{qpdis}	3600			k_{rqpdis}	1000
11,Qi: $QH_2@Qi \leftrightarrow Qi+QH_2$					
k_{qHnds}	4000			k_{rqHnds}	2500
12,Qo: $O_2+Q-@Qo \rightarrow O_2-+Q@Qo$					
k_{ros}	0.02652				

Reverse rate constants marked (K_r) are calculated from the respective forward rate constants and midpoint potentials (ΔE) as described in [23]. Although the reactions of electron transport are shown in simplified form as bimolecular, in fact they are performed (and simulated in the model) as transitions between the states of the whole complex (monomolecular). The units of rate constants are described in the legend of Table 1 (s^{-1} for monomolecular reactions and $s^{-1} \cdot (nmol/mg \text{ prot})^{-1}$ for the rate constants of bimolecular binding). doi:10.1371/journal.pcbi.1001115.t002

more positive (-150 mV, [40]). In this model the relay of Fe-S centers is simplified, so that electrons pass from FMN directly to the N2 center, which can interact with quinones. In this way, two-electron transporter FMN and one-electron transporter N2 form the core of complex I, N2-FMN- FMN (referred as core).

The mechanism of interaction of N2 center with ubiquinone that results in the translocation of four protons from matrix to cytosol and one ubiquinol synthesized is not fully understood. Here we implemented in the model a proposed mechanism, which we consider as a working hypothesis that could be checked by the analysis of model behavior. In this way the model could serve as a tool for checking different possible mechanisms.

According to the EPR data [42,43] there are two ubiquinone-binding sites; bound ubiquinones possess different EPR characteristics, one of them is fast- and another is slow-relaxing. The former one bound in oxidized form in the proximity of N2, in Qn site, could be reduced by N2 and bind protons taking them from negative (matrix side of the membrane) (indicated as Qn below). The other one, bound in the reduced form in Qp site, situated in the proximity of Qn, can interact with Qn-bound semiquinone releasing protons to the positive (cytosolic) side of the membrane. This interaction of two quinones in fact is in agreement with the idea outlined in [39]

that complex I contains a single, but very large, binding domain for its hydrophobic substrate. Binding Q_n and Q_p gives additional three species of the complex I, Q_n-Q_n-N2-FMN- FMN, Q_p-Q_p-N2-FMN- FMN, and Q_p-Q_p-Q_n-Q_n-N2-FMN- FMN.

The proposed mechanism of N2-ubiquinone interactions, which we implemented in the model, is shown in Figure 10, and the individual reaction steps are described in the legend. It satisfies the known stoichiometry of proton translocation and ubiquinone reduction (four protons translocated and one ubiquinol synthesized per two electrons taken from NADH).

The elementary reactions of complex I simulated in the model

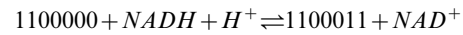
0. Reduction of oxidized FMN by NADH.

In traditional form this equation is expressed as



Any of the forms of complex I with reduced FMN can receive two electrons from NADH, however, subsequent transitions require the interaction of three centers, N2, Q_n and Q_p. Therefore

effective outcome produces only the reduction of FMN in the specie qnpc with ubiquinone bound at Q_n and ubiquinol bound at Q_p, which is reflected by binary number 1100000 corresponding to decimal 96. The reduction of FMN results in the production of redox state 1100011 (decimal 99):



The forward and reverse reaction rates for this transformation are expressed in accordance with mass action law:

$$v_{fI0} = k_{fI0} \times C_{1100000} \times NADH \times H^+; \quad (I.0.1)$$

$$v_{rI0} = k_{rI0} \times C_{1100011} \times NAD^+$$

Here, as described for the complex III, “0” designates oxidized and “1” reduced states.

The ratio of rate constants from I.0.1 could be found from the known redox potentials. Equilibrium constant for this reaction as a function of midpoint electrochemical potentials could be found from the condition of equality of electrochemical potentials at equilibrium:

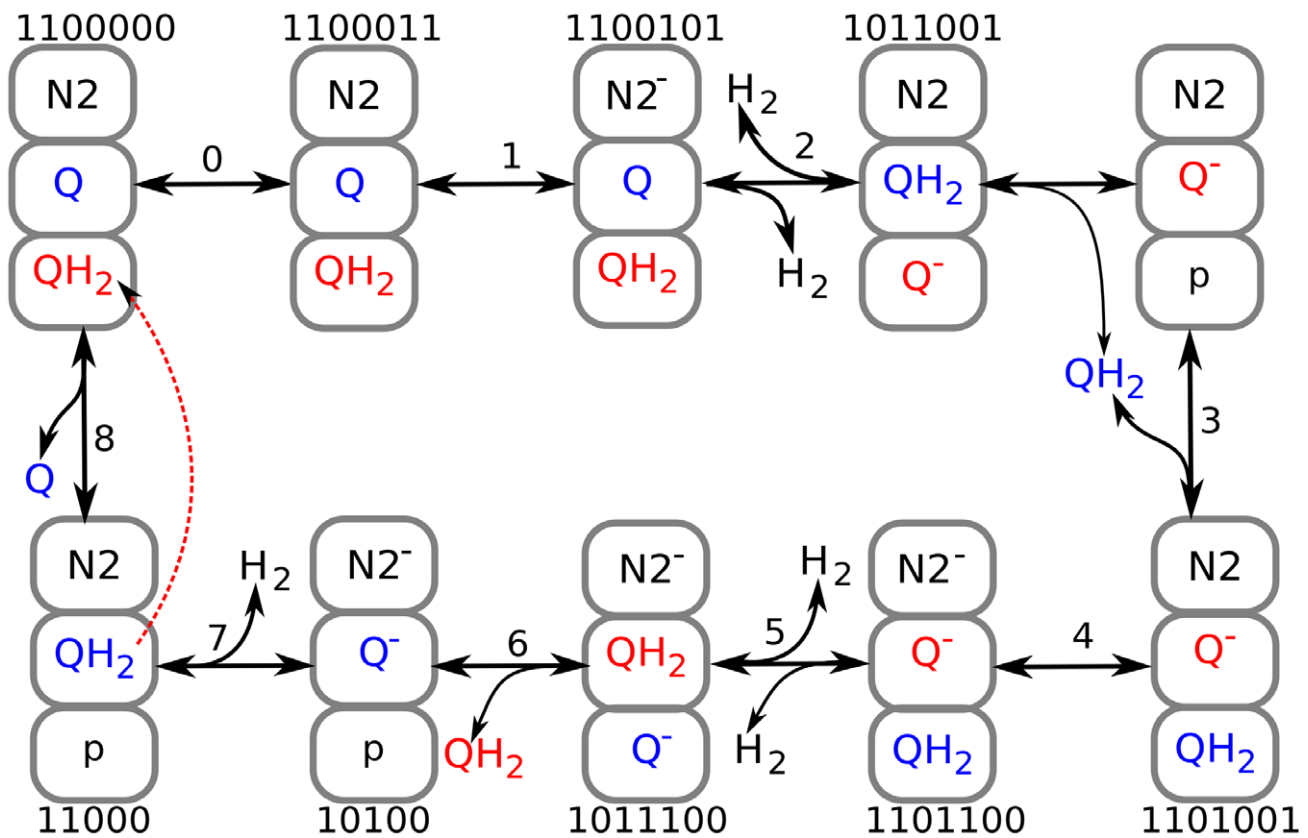


Figure 10. Interactions between N2 centers and quinones in complex I. Numbers above or below a species indicate the redox state of the complex as a combination of electron transporters. The last two digits indicate the presence (1) or absence (0) of two valence electrons of FMN (not shown graphically). The third digit from the right denotes the state of the N2 center, the next two digits from the right indicate the presence or absence of two valence electrons of Q/Q⁻/QH₂ at the n-site. The next two digits from the right indicate the valence electrons of Q/Q⁻/QH₂ at the p-site. Numbers 0–8 above arrows denote individual reactions. 0, FMN reduction by NADH; 1, electron transition from FMN to the N2 center; 2, electron transition from reduced N2 to n-site ubiquinone. This interaction results in electron transfer from p-side ubiquinol to n-side semiquinone, which is coupled to binding of two protons taken from the matrix side and release of two protons to the intermembrane space. 3, ubiquinol thus produced is released and p-site semiquinone changes its position, releasing the p-site, which binds the released ubiquinol; 4, n-site semiquinone takes an electron from p-site semiquinone and forms ubiquinol, taking two protons from the matrix, while the p-site semiquinone formed releases two protons to the p-side of the membrane. 6, ubiquinol formed at the n-site dissociates and semiquinone bound at the p-site changes its location, binding to the n-site. 7, the non-paired electron of N2 is captured by n-site semiquinone, which subsequently takes two protons from the matrix and is converted to ubiquinol. 8, release of n-site bound ubiquinol, and binding of ubiquinol at the p-site and ubiquinone at the n-site. doi:10.1371/journal.pcbi.1001115.g010

$$E_m(FMN/FMNH_2) + \frac{RT}{nF} \times \ln\left(\frac{FMN}{FMNH_2}\right) = E_m(NAD^+/NADH) + \frac{RT}{nF} \times \ln\left(\frac{NAD^+}{NADH}\right) \quad (I.0.2)$$

$$\Delta E_m = E_m(NAD^+/NADH) - E_m(FMN/FMNH_2) = \frac{RT}{nF} \times \ln\left(\frac{NAD^+ \times FMNH_2}{NADH \times FMN}\right) \quad (I.0.3)$$

since $K_{eq} = \frac{k_f}{k_r} = \frac{NAD^+ \times FMNH_2}{NADH \times FMN \times H^+}$, expression (I.0.3) could be rewritten as

$$\Delta E_m \times \frac{nF}{RT} = \ln\left(\frac{k_f \times H^+}{k_r}\right) \quad (I.0.4)$$

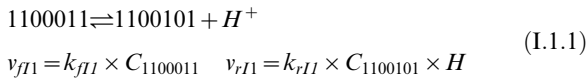
$$\text{and } \frac{k_f \times H^+}{k_r} = \exp(\Delta E_m \times \frac{nF}{RT}) = \exp(-20 \times 2 \times 0.039) = 0.21 \quad (I.0.5)$$

taking into account that the difference between midpoint potentials for NADH (-320 mV) and FMN (-340 mV) [40] is $\Delta E_m = -20$ mV.

1. Reduction of the N2 center by FMN (step 1 in Figure 7):



First electron of FMNH₂, which by convention occupied second position from the right in binary representation, passes to N2 converting 0 into 1 in the third position from the right:



The relationship between forward and reverse rate constants could be defined similar to (I.7). For the first transition at equilibrium

$$E_m(Fe^{3+}/Fe^{2+}) + \frac{RT}{nF} \ln\left(\frac{Fe^{3+}}{Fe^{2+}}\right) = E_m(FMNH/FMNH_2) + \frac{RT}{nF} \times \ln\left(\frac{FMNH}{FMNH_2}\right) \quad (I.1.2)$$

$$\Delta E_m = E_m(Fe^{3+}/Fe^{2+}) - E_m(FMNH/FMNH_2) = \frac{RT}{nF} \times \ln\left(\frac{FMNH \times Fe^{2+}}{FMNH_2 \times Fe^{3+}}\right)$$

since $K_{eq} = \frac{k_f}{k_r} = \frac{FMNH \times Fe^{2+} \times H}{FMNH_2 \times Fe^{3+}}$, eq (I.1.2) can be written as

$$\Delta E_m = E_m(Fe^{3+}/Fe^{2+}) - E_m(FMNH/FMNH_2) = \frac{RT}{nF} \times \ln\left(\frac{k_f}{k_r \times H}\right) \quad (I.1.3)$$

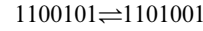
$$\frac{k_f}{k_r \times H} = \exp(\Delta E_m \times \frac{nF}{RT}) = \exp((-150 + 350) \times 0.039) = 2440$$

since at pH=7 $E_m(FMN^-/FMNH_2) = -350$ mV [43], and E_m for N2 iron-sulfur center $E_m = -150$ mV [40].

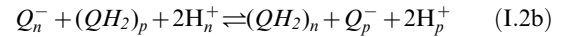
2. Reduction of Q_n by the reduced N2 center (first electron) and by QH₂ bound at Q_p center (second electron):



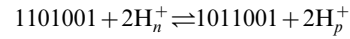
In binary form:



The semiquinone Q_n⁻ is very active [17], so it reacts with QH₂ bound at p-site:

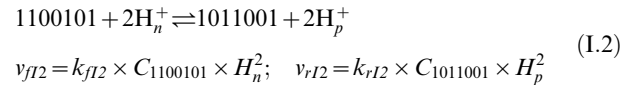


In binary form:



This reaction is symmetrical: p-side quinol and n-side semiquinone give p-side semiquinone and n-side quinol. The distance between the two quinone binding sites can be estimated as follows. Fast-relaxing semiquinone (bound to n-side oriented proton well) situated at the distance of ~12 Å from N2, slow-relaxing semiquinone (bound to p-side oriented proton well) situated at the distance of ~30 Å from N2 [42]. The distance between the bound quinones could be around 18 Å, which makes possible the interaction between them, taking into account the high energy of electron coming from FMN to Q_n-bound quinone through N2 center. The assumption of such interaction fulfills the known stoichiometry of translocation of four protons and overall reduction of one ubiquinone coupled with the transport of two electrons through complex I.

We grouped together these two reactions:



Overall in this reaction the oxidation of N2 center is coupled with the reduction of Q_n.

$$E_m(Q/Q^-) + \frac{RT}{nF} \times \ln\left(\frac{Q}{Q^-}\right) = E_m(Fe^{3+}/Fe^{2+}) + \frac{RT}{nF} \ln\left(\frac{Fe^{3+}}{Fe^{2+}}\right) \quad (I.2)$$

$$\Delta E_m = E_m(Fe^{3+}/Fe^{2+}) - E_m(Q/Q^-) = \frac{RT}{nF} \times \ln\left(\frac{FMNH \times Fe^{2+}}{FMNH_2 \times Fe^{3+}}\right)$$

Since

$$K_{eq} = \frac{k_f}{k_r} = \frac{Fe^{3+} \times Q^- \times H_n^2}{Fe^{2+} \times Q \times H_p^2}, \quad \Delta E_m = E_m(Q/Q^-) - E_m(Fe^{3+}/Fe^{2+}) = \frac{RT}{nF} \times \ln\left(\frac{k_f \times H_n^2}{k_r \times H_p^2}\right)$$

$$\text{and } \frac{k_f \times H_n^2}{k_r \times H_p^2} = \exp(\Delta E_m \times \frac{nF}{RT}) = \exp((-45 + 150) \times 0.039) = 60$$

Here is considered that Em for N2 center is -150 mV [40] and Em for ubiquinone one-electron reduction is -45 mV [42].

3. Dissociation of QH_{2n} at n-site, transition of p-site SQ_p to the n-site and binding of dissociated QH_{2n} at p-site.

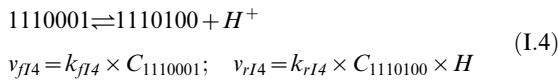
In this step the three reactions are combined: dissociation of QH_2 formed at n-site, change of position of p-site bound semiquinone, and binding QH_2 at p-site. Overall in binary form:



and the forward and reverse rates are:

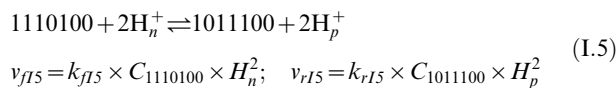
$$v_{r13} = k_{r13} \times C_{1011001} \quad v_{f13} = k_{f13} \times C_{1110001}$$

4. Second electron (from radical FMN^- , which by convention occupied the right position) passes to N2 converting 0 into 1 in the third position from the right:

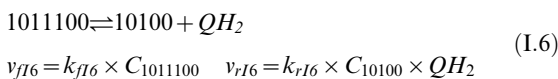


The transition of second electron characterized by the same ΔE_m as accepted in (I.1), but it is not related with proton binding or release, therefore the right hand side value of (I.1.3) equals to the ratio k_f/k_r .

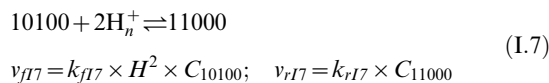
5. Reduction of N2 by FMN in step 4 induces the interaction of n-site semiquinone with p-site quinol resulted in the production of n-site quinol and p-site semiquinone coupled with the translocation of two protons:



The dissociation of n-site quinol produced and the change of position of p-site semiquinone:



6. The reduction of n-site semiquinone by N2 coupled with the binding of two protons:



In equilibrium

$$E_m(Q_n^- / (QH_2)_n) + \frac{RT}{nF} \times \ln\left(\frac{Q_n^-}{(QH_2)_n}\right)$$

$$= E_m(Fe^{3+} / Fe^{2+}) + \frac{RT}{nF} \ln\left(\frac{Fe^{3+}}{Fe^{2+}}\right)$$

$$\Delta E_m = E_m(Q_n^- / (QH_2)_n) - E_m(Fe^{3+} / Fe^{2+})$$

$$= \frac{RT}{nF} \times \ln\left(\frac{(QH_2)_n \times Fe^{3+}}{Q_n^- \times Fe^{2+}}\right)$$

$$\text{Since } K_{eq} = \frac{k_f}{k_r} = \frac{(QH_2)_n \times Fe^{3+}}{Q_n^- \times Fe^{2+} \times H_n^2}$$

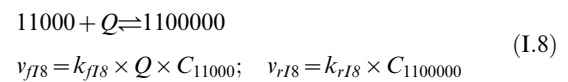
$$\Delta E_m = E_m(Q_n^- / (QH_2)_n) - E_m(Fe^{3+} / Fe^{2+}) = \frac{RT}{nF} \times \ln\left(\frac{k_f \times H_n^2}{k_r}\right)$$

and the ratio of forward and reverse rate constants could be expressed as

$$\frac{k_f \times H_n^2}{k_r} = \exp(\Delta E_m \times \frac{nF}{RT}) = \exp((-63 + 150) \times 0.039) = 30$$

taking into account that Em for ubiquinol reduction in -63 mV [42] and Em for reduced N2 center oxidation is -150 mV [40].

7. QH_2 dissociates, Q binds at n-site and QH_2 binds at p-site, overall:



Above, the ratios of forward and reverse rate constants for the redox reactions of complex I are defined and summarized in Table 3. The particular values were defined from fitting the experimental data presented in "Results" using these ratios as restrictions. In some cases the fitting required different value of midpoint potential. This may indicate the differences in the operation of complex I in situ and under the specific conditions of midpoint potentials determination. Recognizing the importance of this subject we leave its studying for future because it deserves a separate consideration.

Although the mathematical description of complex I and complex III are similar, they differ in the strictness of rules for electron transport and proton translocation. For complex III the transition between two transporters allowed for any states of other transporters. This assumes participation of all 400 redox forms in electron transport. For complex I the rules accepted in the model allow participation in electron transport only several selected form. This illustrates the flexibility of methodology applied.

Transmembrane electrochemical gradient of H^+

Proton binding to ubiquinone at the matrix side of the membrane and their dissociation from ubiquinol to the intermembrane space results in the translocation of protons and arising the transmembrane gradient of H^+ concentration and electric potential. As described above for complex I, the reactions (I.2), (I.5) and (I.7) reduce ubiquinone each time taking two protons from the matrix. In complex III the reduction of ubiquinone at Qj site by reduced cytochrome b_H is coupled with binding two protons taken from the matrix. The rate of this process (v_{35}) is calculated as described in [23]. The electron flow (v_O) through complex IV results in the reduction of oxygen with the uptake of two protons from the matrix and additional two protons are transferred from the matrix to cytosol. Proton leak (v_{lk}) and ATP synthesis (v_{syn}) return the protons transferred back to the matrix: v_{lk} is leak of protons through the membrane:

$$v_{lk} = k_{lk} \times (H_o - H_i) \times \exp\left(\frac{F}{RT} \times \Psi\right); \quad (H.1)$$

v_{syn} is the reaction rate of ATP synthase, which uses the energy of three protons translocating them back to matrix to synthesize one ATP:

Table 3. Rate constants for the reactions performed by complex I.

FMN: FMN+NADH+H⁺↔FMNH₂+NAD⁺					
k_{f10}	640000	ΔE	-20	k_{r10}	880000
N2: FMNH₂+Fe³⁺↔FMNH+Fe²⁺+H⁺					
k_{f11}	157000	ΔE	93	k_{r11}	4200
N2: Q(n)+Fe²⁺↔Fe³⁺+Q-(n)					
k_{f12}	770000	ΔE	60	k_{r12}	80000
Qp-Qn, 1: Q⁻(n)+2H⁺(n)+QH₂(p)↔					
QH₂(n)+2H⁺(p)+Q⁻(p)					
2: QH₂(n) Q⁻(p)↔QH₂(p) Q⁻(n)					
k_{f12}	23000			k_{r12}	150
FMN: FMNH+Fe³⁺↔FMN+Fe²⁺+H⁺					
k_{f14}	157000	ΔE	93	k_{r14}	4200
N2: Q⁻n+Fe²⁺+2H⁺n = QH₂+Fe³⁺					
k_{f15}	190000	ΔE	107	k_{r15}	3000
QH2: QH2@Qn↔Qn+QH2					
k_{f16}	160000			k_{r16}	16000
Q: Qn+Q↔Q@Qn					
k_{f18}	200000			k_{r18}	3000

The units are the same as described in Table 1.
doi:10.1371/journal.pcbi.1001115.t003

$$v_{syn} = v_{lk} \frac{V_{syn} \times ADP}{K_m(ADP) + ADP} \quad (H.2)$$

The total rate of reversible uptake of the matrix protons is expressed as follows:

$$v_{Hi} = (-2v_{35} - 2v_{12} - 2v_{15} - 2v_{17} - 4v_0 + v_{lk} + v_{syn}) \quad (H.3)$$

The reactions (I.2) and (I.5) also release protons into the intermembrane space. For complex III the rate v_{30} release protons as described in [23]. The flux v_0 transfers two electrons outside and leak and ATP synthesis consume the gradient:

$$v_{Ho} = (2v_{35} + 2v_{12} + 2v_{15} + 2v_0 - v_{lk} - v_{syn}) \quad (H.4)$$

The rates of proton translocations (H.1) and (H.2) change cytosolic (outside) and matrix (inside) proton concentrations (H_o and H_i) as described by the following differential equations:

$$dH_i/dt = v_{Hi}/bi/Vi \quad (H.5)$$

$$dH_o/dt = v_{Ho}/bo/Vo \quad (H.6)$$

Here bo , bi , Vo , Vi are the buffer capacity and volume of outer and inner intracellular space with regards to mitochondria respectively.

The differential equation for electric potential difference (Ψ) used the same terms as that for proton concentration, but multiplied by a coefficient, which transforms the flux of ions into the change of electric potential:

$$d\Psi/dt = (v_{Hi} + v_{Ho}) \times F/C \quad (H.7)$$

where F is Faraday number (96000 cu/mol or $0.96 \cdot 10^{-4}$ cu/nmol), C is electric capacity of the membrane ($2 \cdot 10^{-4}$ F/mg of protein, as computed based on [44]).

Connection of respiration with central energy metabolism

Substrates for respiration, i.e. NADH and succinate are produced in TCA cycle inside mitochondria and in the model the connection of this part of intracellular metabolism with respiration through these common metabolites is taken into account by the simulations of following reactions.

Since the emphasis of work described here is the operation of respiratory chain, the reactions of TCA cycle were simulated in simplified form, as linear function of each substrate. Such expressions assume that the substrate concentrations are far from saturation, which should be true for the most cases. In this case the usual hyperbolic dependence of enzymatic reactions on substrate concentrations is close to the linear dependence. On the other hand, this simplification allows to avoid such unfavorable situation, when choosing inappropriate K_m makes reactions artificially insensitive to substrate changes. Therefore we used such assumption as a first approximation, which could be easily corrected with obtaining more information about the properties of system.

Pyruvate transport and transformation to acetyl coenzyme A:

$$v_{PDH} = k_{pyrIn} \times (C_{aMax} - C_{accoa}) \times C_{NAD}; \quad (T.1)$$

Citrate Synthase :

$$v_{cs} = k_{cs} \times C_{oaa} \times C_{pyr}; \quad (T.2)$$

here the conversion of pyruvate into acetyl coenzyme A, linked with $NAD^+ \rightarrow NADH$ transformation, is included in the same reaction.

The reactions converting citrate into succinate were joined together, taking into account that NAD^+ is used in these reactions:

$$v_{tea} = k_{tea} \times C_{NAD} \times C_{cit}; \quad (T.3)$$

Then succinate is transformed into fumarate in succinate dehydrogenase reaction, which reduces Q taking two protons from matrix:

$$v_{SDH} = \frac{V_{SDH} \times Q \times suc}{(K_m(Q) + Q) \times (K_m(suc) + suc)} \quad (T.4)$$

Here the total content of reduced and oxidized ubiquinone is conserved at the levels defined by [45] (6 nmol/mg prot).

Succinate not only could be produced in TCA cycle but also transported from outside of mitochondria in exchange to fumarate or malate (which are lumped in one pool in the present version of the model):

$$v_{sfe} = k_{sfe} \times (C_{sucOut} \times C_{fum} - C_{suc} \times C_{fumOut}); \quad (T.5)$$

Succinate could also be exchanged to phosphate:

$$v_{spe} = k_{spe} \times (C_{sucOut} \times C_{pi} - C_{suc} \times C_{po}); \quad (T.6)$$

Malate dehydrogenase reaction transforms lumped fumarate/malate pool into oxaloacetate producing NADH:

$$v_{MDH} = k_{MDHf} \times C_{NAD} \times C_{fum} - k_{MDHr} \times C_{NADH} \times C_{oaa}; \quad (T.7)$$

Malic enzyme transforms malate into pyruvate producing NADH:

$$v_{me} = k_{me} \times C_{NAD} \times C_{fum}; \quad (T.8)$$

The concentrations of metabolites were calculated by numerical solving the differential equations constructed using the above expressions for reaction rates:

$$dC_{oaa}/dt = -v_{cs} + v_{MDH} - v_{me} - v_{soae}; \quad (T.9)$$

$$dC_{accoa}/dt = v_{PDH} - v_{cs} + v_{me}; \quad (T.10)$$

$$dC_{cit}/dt = v_{cs} - v_{tca}; \quad (T.11)$$

$$dC_{suc}/dt = v_{tca} - v_{MDH} - v_{SDH} + v_{sfe} + v_{soae}; \quad (T.12)$$

$$dC_{fum}/dt = v_{SDH} - v_{MDH} - v_{sfe} - v_{me}; \quad (T.13)$$

The differential equation, which describes the evolution of NADH takes into account the stoichiometry of its production in TCA cycle and consumption by complex I (reaction (I.0) described above.

$$dC_{NADH}/dt = v_{PDH} + 2v_{tca} + v_{MDH} + v_{me} - v_{I0}; \quad (T.14)$$

The total concentration of NAD and NADH is assumed to be constant, so that NAD+, which defines the rates of TCA cycle reactions is computed as $C_{NAD} = C_{NADt} - C_{NADH}$.

The reactions linked with electron transport and respective parameters are summarized in Table 4. In total, without the reactions of pyruvate transport and ATP synthase, which were switched out in accordance with experiments analyzed, this module contains 11 parameters.

As the presented equations show, although the expressions for reaction rates are simplified, the stoichiometry of succinate and NADH production and succinate transport is reflected precisely in the model and this was the most important for the presented step of study of the link between central metabolism and ROS production by electron transport chain and the role of reverse electron transport in this process.

An algorithm for fitting experimental data

The whole model contains $(22-6)+(18-7)+11 = 51$ parameter (22 for complex III, 18 for complex I, and 11 for the rest of reactions simulated). The six parameters of complex III and seven parameters of complex I are defined by the known values of midpoint potential. The other parameters were validated by fitting experimental data. To fit the experimental data our modification of Simulating Annealing algorithm was implemented in the way similar to that in [22]. The specificity of this algorithm was defined by the specificity of experimental data. The dynamics of NAD+ reduction was measured under the two different conditions, in the presence and absence of rotenone, an inhibitor of reduction/oxidation of quinones in complex I. The presence of rotenone was simulated by decreasing to zero the rate constants of step 5 in the reactions performed by complex I ($k_{f15} = k_{r15} = 0$), and the two conditions were fitted simultaneously for the same values of all other parameters. The procedure consisted of minimization of χ^2 ,

Table 4. Reactions and rate constants for the reactions linked with respiratory chain.

H⁺ leak:			
	k_{lk}		1500
ATP synthase			
V_{syn}	0	K_{mADP}	0.01
pyr transport & pdh			
k_{pyrin}	630		
accoa+pyr→cit			
k_{cs}	1300		
2NAD⁺+cit→suc+2NADH+2H⁺			
k_{tca}	750		
CII: suc→fum			
	V_{SDH}		170
K_{mQ}	0.5	K_{mSUC}	0.1459
Dicarboxylate exchange			
k_{sfe}	6.5		
Exchange suc↔Pi			
k_{spe}	270		
NAD⁺+fum↔oaa+NADH+H⁺			
k_{MDHf}	460	k_{MDHr}	460
ME: fum+NAD⁺→pyr+NADH			
k_{me}	0.0003		

Maximal rates (Vmax) are expressed in (nmol/mg prot)/s, Km are expressed in nmol/mg prot, rate constants for bimolecular reactions are in $s^{-1} \cdot (mg \text{ prot})^{-1}$, monomolecular reactions are in s^{-1} .
doi:10.1371/journal.pcbi.1001115.t004

normalized sum of squares of deviations from experimental data. χ^2 was calculated based on two simulations, first, normal conditions and, second, the presence of rotenone ($k_{f15} = k_{r15} = 0$, and all other parameters as in the first simulation).

The fitting algorithm made the following actions:

1. made the stochastic perturbation of given set of parameters (Vmax for the reactions of TCA cycle and substrate transport through the membrane)
2. performed coordinate descent, taking the parameters one by one and changing them in the direction, which decreased χ^2
3. after reaching the local minimum of χ^2 the program saved the respective set of parameters
4. returned back to step 1.

The cycles of perturbations and coordinate descent repeated thousands times and saved sets of parameters were analyzed: program read the saved sets with corresponding values of χ^2 , defined the best fit (absolute minimum of χ^2), the set of parameters, corresponding to the best fit, and defined confidence intervals for the parameters using the criterion of $\Delta\chi^2$ [31].

Experimental procedures

All procedures involving animals were approved by Children's Hospital of Pittsburgh and were in compliance with "Principles of Laboratory Animal Care" and the current laws of the United States.

Brain mitochondria were isolated from the cortex of adult Wistar rats. After removal, tissue was minced and homogenized in ice-cold isolation buffer I (IB I) which contained: 225 mM mannitol, 75 mM sucrose, 5 mM HEPES buffer (pH adjusted to 7.3 with KOH), 0.1 mg/ml fatty acid free BSA, 1 mM tetrapotassium EDTA and 12% Percoll. The homogenate thus

obtained was carefully layered on the top of a discontinuous gradient of Percoll (24% and 42%) prepared using the same buffer. The preparation was then centrifuged at $16,000\times g$ for 10 min. The fraction containing the mitochondria located between 42% and 24% Percoll was carefully withdrawn by a syringe and washed from Percoll twice by pelleting in IB I. The resulting mitochondrial suspension was diluted in isolation buffer II (IB II), which was similar to IB I, except for the concentration of EDTA (0.1 mM) and lack of albumin, and spun down at $12,000\times g$ for 10 min. The deposit of mitochondria was homogenized in IB II at a final protein concentration of ~ 20 mg/ml and stored on ice until use. The protein concentration in the mitochondrial samples was determined using a Protein Assay kit (Pierce Chemical Company, Rockford IL) according to the manufacture's instructions. Mitochondria prepared in this way were active for at least 5–6 hours, as determined by their ability to maintain a stable transmembrane potential in the presence of oxidizable substrates.

Fluorescence measurements were performed in a stirred cuvette mounted in a Shimadzu RF-5301 spectrofluorimeter maintained at 37°C . Mitochondria (0.2 mg/ml of protein) were added to 1.5 ml of the basic incubation medium that contained: 125 mM KCl; 2 mM KH_2PO_4 ; 2 mM MgCl_2 ; 10 mM Tris; 10 mM HEPES (pH 7.0); 100 μM EGTA; and oxidizable substrates as indicated in a particular experiment. Concentration of rotenone, when indicated, was 1 μM .

Fluorescence of NAD(P)H was measured at excitation/emission wavelengths 365 nm (slit 5 nm)/463 nm (slit 10 nm), respectively. To quantify the measurements a calibration curve was constructed using standard concentrations of commercial NADH.

Hydrogen peroxide was measured by fluorescence of Amplex red (2 μM), which increased upon oxidation to resorufin in the presence of 1 U/ml of horseradish peroxidase (HRP) as previously described [15]. Measurements were carried out at excitation/emission wavelengths of 560 nm (slit 1.5 nm)/590 nm (slit 3 nm), respectively. Amounts of H_2O_2 released by mitochondria were estimated by constructing calibration curves using known H_2O_2 concentrations in the standard incubation buffer together with Amplex red and HRP, but without mitochondria.

Mitochondrial transmembrane potential, $\Delta\Psi_m$, was estimated using fluorescence quenching of the cationic dye safranin O. Since polarized mitochondria have a negative charge inside, positively charged molecules of safranin O are accumulated inside the matrix; increase in dye concentration inside the matrix leads to fluorescence quenching, thus, a decrease in fluorescence corresponds to an increase of membrane potential. The excitation wavelength was 495 nm (slit 3 nm) and emission 586 nm (slit 5 nm), and the dye concentration used was 2.5 μM [15].

Mitochondrial respiration rates were measured by an Oroboros High Resolution Respirometer (Innsbruck, Austria) in a stirred 2 mL chamber at 37°C in the same incubation media as indicated above. Oxygen sensor was calibrated at each experiment according to the manufacture's instructions. Calculations of respiratory rates were performed by software built into the instrument.

Supporting Information

Figure S1 The scheme of reactions performed by complex III as it is generally accepted (considered in Selivanov et al, 2009). One of two electrons taken from ubiquinol (QH₂), which releases its

two protons into the intermembrane space, recycles through cytochromes bh and bl reducing another quinone. The other electron continues its way to oxygen through cytochromes c1 and c and complex IV. Complexes I and II provide QH₂. The reactions 0–12 are described in detail in the text.

Found at: doi:10.1371/journal.pcbi.1001115.s001 (0.04 MB TIF)

Figure S2 Simulation of time course of reduction of cytochromes bh (thick grey line) and c1 (thin black line), and ubiquinone (dashed line). This simulation was made using initial set of parameters. Ordinate represents the content of reduced forms in nmol/mg of protein, time units are arbitrary.

Found at: doi:10.1371/journal.pcbi.1001115.s002 (0.02 MB TIF)

Figure S3 Simulation of time course of reduction of cytochromes bh performed with various values of dissociation constants for Q and QH₂ species. Curve 0 calculated with initial values of parameters taken in (Selivanov et al, 2009), curve 1 calculated with the tenfold decrease of K_d for QH₂ and Q binding at Q_o and Q_i respectively, and the tenfold increase of K_d for Q and QH₂ dissociation at Q_o and Q_i respectively. All the changes favor forward direction of Q-cycle. Curve 2 calculated favoring the reverse direction of Q-cycle by the tenfold decrease of initial value of K_d for QH₂ dissociation, and all other parameters as for curve 1.

Found at: doi:10.1371/journal.pcbi.1001115.s003 (0.03 MB TIF)

Figure S4 Simulation of time course of reduction of cytochromes bh performed with various combinations of ΔE_m for the first and second electron transitions from bh to Q at Q_i. In all presented cases $E_m(\text{bHox/bHred}) = 61$ mV. Curve 0 is the same as in Figure 3, Curve 1 is calculated accepting $E_m(\text{Q/Q-}) = 45$ mV and $E_m(\text{Q-/QH}_2) = 150$ mV (Rich, 1984). Curve 2 is calculated accepting $E_m(\text{Q/Q-}) = 90$ mV and $E_m(\text{Q-/QH}_2) = 16$ mV (Covian, 2007). All other parameters are the same for all curves with the values given in (Selivanov et al, 2009).

Found at: doi:10.1371/journal.pcbi.1001115.s004 (0.03 MB TIF)

Table S1 Sensitivity of simulation of mitochondrial respiration with regards to the parameters. First column gives the list of parameters, next four columns give the relative change of respectively dynamics of NAD⁺ reduction in the absence and presence of rotenone, uncoupled respiration fueled by succinate, and pyruvate/malate. Next four columns give the relative change of SQ at Q_o site of complex III, in the same four simulations as above, then, relative change of SQ at Q_n site of complex I, then FMNH, and finally, reduced N₂ centers. The highest changes marked black.

Found at: doi:10.1371/journal.pcbi.1001115.s005 (0.03 MB XLS)

Text S1 Analysis of triphasic dynamics of cytochrome bh reduction using the model of Complex III from our publication (PLoS Comput Biol 2009, 5(12): e1000619) for the validation of parameter.

Found at: doi:10.1371/journal.pcbi.1001115.s006 (0.08 MB PDF)

Author Contributions

Conceived and designed the experiments: VAS TVV. Performed the experiments: TVV VNP JZ. Analyzed the data: VAS TS MT JR MC. Contributed reagents/materials/analysis tools: VAS. Wrote the paper: VAS TVV.

References

- Koopman WJ, Nijtmans LG, Dieteren CE, Roestenberg P, Valsecchi F, et al. (2010) Mammalian mitochondrial complex I: biogenesis, regulation, and reactive oxygen species generation. *Antioxid Redox Signal* 12: 1431–1470.
- McCord JM, Fridovich I. Superoxide dismutase: the first twenty years (1968–1988) (1988). *Free Radic Biol Med* 5: 363–369.
- Acker H (2005) The oxygen sensing signal cascade under the influence of reactive oxygen species. *Philos Trans R Soc Lond B Biol Sci* 360: 2201–2210.

4. Brookes PS, Yoon Y, Robotham JL, Anders MW, Sheu SS (2004) Calcium, ATP, and ROS: a mitochondrial love-hate triangle. *Am J Physiol Cell Physiol* 287: C817–C833.
5. Waypa GB, Marks JD, Guzy R, Mungai PT, Schriewer J, et al. (2010) Hypoxia triggers subcellular compartmental redox signaling in vascular smooth muscle cells. *Circ Res* 106: 526–535.
6. Cheng Y, Zhu P, Yang J, Liu X, Dong S, et al. (2010) Ischemic preconditioning-regulated miR-21 protects the heart from ischemia/reperfusion injury via anti-apoptosis through its target PDCD4. *Cardiovasc Res* 87: 431–439.
7. Won Kim H, Haider HK, Jiang S, Ashraf M (2009) Ischemic preconditioning augments survival of stem cells via miR-210 expression by targeting caspase-8-associated protein 2. *J Biol Chem* 284: 33161–33168.
8. Kroemer G, Blomgren K (2007) Mitochondrial Cell Death Control in Familial Parkinson Disease. *PLoS Biol* 5(7): e206. doi:10.1371/journal.pbio.0050206.
9. Armann B, Hanson MS, Hatch E, Steffen A, Fernandez LA (2007) Quantification of basal and stimulated ROS levels as predictors of islet potency and function. *Am J Transplant* 7: 38–47.
10. Rea SL, Ventura N, Johnson TE (2007) Relationship Between Mitochondrial Electron Transport Chain Dysfunction, Development, and Life Extension in *Caenorhabditis elegans*. *PLoS Biol* 5(10): e259. doi:10.1371/journal.pbio.0050259.
11. Chen Q, Vazquez EJ, Moghaddas S, Hoppel CL, Lesnfsky EJ (2003) Production of reactive oxygen species by mitochondria: central role of complex III. *J Biol Chem* 278: 36027–36031.
12. St-Pierre J, Buckingham JA, Roebuck SJ, Brand MD (2002) Topology of superoxide production from different sites in the mitochondrial electron transport chain. *J Biol Chem* 277: 44784–44790.
13. Hoffman DL, Brookes PS (2009) Oxygen sensitivity of mitochondrial reactive oxygen species generation depends on metabolic conditions. *J Biol Chem* 284: 16236–1623645.
14. Boveris A, Chance B (1973) The mitochondrial generation of hydrogen peroxide: general properties and effect of hyperbaric oxygen. *Biochem J* 134: 707–716.
15. Votyakova TV, Reynolds IJ (2001) DeltaPsi(m)-Dependent and -independent production of reactive oxygen species by rat brain mitochondria. *J Neurochem* 79: 266–277.
16. Schönfeld P, Wojtczak L (2007) Fatty acids decrease mitochondrial generation of reactive oxygen species at the reverse electron transport but increase it at the forward transport. *Biochim Biophys Acta* 1767: 1032–1040.
17. Dutton PL, Moser CC, Sled VD, Daldal F, Ohnishi T (1998) A reductant-induced oxidation mechanism for complex I. *Biochim Biophys Acta* 1364: 245–257.
18. Ohnishi T, Salerno JC (2005) Conformation-driven and semiquinone-gated proton-pump mechanism in the NADH-ubiquinone oxidoreductase (complex I). *FEBS Lett* 579: 4555–4561.
19. Orii Y, Miki T (1997) Oxidation process of bovine heart ubiquinol-cytochrome c reductase as studied by stopped-flow rapid-scan spectrophotometry and simulations based on the mechanistic Q cycle model. *J Biol Chem* 272: 17594–17604.
20. Selivanov VA, Puigjaner J, Sillero A, Centelles JJ, Ramos-Montoya A, et al. (2004) An optimized algorithm for flux estimation from isotopomer distribution in glucose metabolites. *Bioinformatics* 20: 3387–3397.
21. Selivanov VA, Meshalkina LE, Solovjeva ON, Kuchel PW, Ramos-Montoya A, et al. (2005) Rapid simulation and analysis of isotopomer distributions using constraints based on enzyme mechanisms: an example from HT29 cancer cells. *Bioinformatics* 21: 3558–3564.
22. Selivanov VA, Marin S, Lee PWN, Cascante M (2006) Software for dynamic analysis of tracer-based metabolomic data: estimation of metabolic fluxes and their statistical analysis. *Bioinformatics* 22: 2806–2812.
23. Selivanov VA, Votyakova TV, Zeak JA, Trucco M, Roca J, Cascante M (2009) Instability of mitochondrial respiration underlies paradoxical reactive oxygen species generation induced by anoxia. *PLoS Comput Biol* 5(12): e1000619.
24. Tang HL, Trumpower BL (1986) Triphasic reduction of cytochrome b and the protonmotive Q cycle pathway of electron transfer in the cytochrome bcl complex of the mitochondrial respiratory chain. *J Biol Chem* 261: 6209–6215.
25. Selivanov VA, Zeak JA, Roca J, Cascante M, Trucco M (2008) The role of external and matrix pH in mitochondrial reactive oxygen species generation. *J Biol Chem* 283: 29292–29300.
26. Boveris A, Cadenas E, Stoppani AO (1976) Role of ubiquinone in the mitochondrial generation of hydrogen peroxide. *Biochem J* 156: 435–444.
27. Cadenas E, Boveris A, Ragan CI, Stoppani AO (1977) Production of superoxide radicals and hydrogen peroxide by NADH-ubiquinone reductase and ubiquinol-cytochrome c reductase from beef-heart mitochondria. *Arch Biochem Biophys* 180: 248–257.
28. Kwong I.K., Sohal RS (1998) Substrate and site specificity of hydrogen peroxide generation in mouse mitochondria. *Arch Biochem Biophys* 350: 118–126.
29. Zickermann V, Dröse S, Tocilescu MA, Zwicker K, Kerscher S, Brandt U (2008) Challenges in elucidating structure and mechanism of proton pumping NADH:ubiquinone oxidoreductase (complex I). *J Bioenerg Biomembr* 40: 475–483.
30. Fato R, Bergamini C, Bortolus M, Maniero AL, Leoni S, Ohnishi T, Lenaz G (2009) Differential effects of mitochondrial Complex I inhibitors on production of reactive oxygen species. *Biochim Biophys Acta* 1787: 384–392.
31. Press WH, Flannery BP, Teukolsky SA, Vetterling WT (2002) *Numerical Recipes in C: The Art of Scientific Computing*. New York: Cambridge University Press.
32. Blinov ML, Faeder JR, Goldstein B, Hlavacek WS (2004) BioNetGen: software for rule-based modeling of signal transduction based on the interactions of molecular domains. *Bioinformatics* 20: 3289–3291.
33. Hlavacek WS, Faeder JR, Blinov ML, Posner RG, Hucka M, Fontana W (2006) Rules for modeling signal-transduction systems. *Sci STKE* 344: re6.
34. Kudin AP, Debska-Vielhaber G, Kunz WS (2005) Characterization of superoxide production sites in isolated rat brain and skeletal muscle mitochondria. *Biomed Pharmacother* 59: 163–168.
35. Genova ML, Ventura B, Giuliano G, Bovina C, Formiggini G, Parenti Castelli G, Lenaz G (2001) The site of production of superoxide radical in mitochondrial Complex I is not a bound bisemiquinone but presumably iron-sulfur cluster N2. *FEBS Lett* 505: 364–368.
36. Brand MD (2010) The sites and topology of mitochondrial superoxide production. *Exp Gerontol* 45: 466–472.
37. Lambert AJ, Brand MD (2009) Reactive oxygen species production by mitochondria. *Methods Mol Biol* 554: 165–181.
38. Zorov DB, Filburn CR, Klotz LO, Zweier JL, Sollott SJ (2000) Reactive oxygen species (ROS)-induced ROS release: a new phenomenon accompanying induction of the mitochondrial permeability transition in cardiac myocytes. *J Exp Med* 192: 1001–1014.
39. Brandt U (2006) Energy converting NADH:quinone oxidoreductase (complex I). *Annu Rev Biochem* 75: 69–92.
40. Ohnishi T (1998) Iron-sulfur clusters/semiquinones in complex I. *Biochim Biophys Acta* 1364: 186–206.
41. Vinogradov AD (1998) Catalytic properties of the mitochondrial NADH-ubiquinone oxidoreductase (Complex I) and the pseudo-reversible active/inactive enzyme transition. *Biochim Biophys Acta* 1364: 169–185.
42. Ohnishi T, Johnson JE, Jr., Yano T, LoBrutto R, Widgerb WR (2005) Thermodynamic and EPR studies of slowly relaxing ubisemiquinone species in the isolated bovine heart complex I. *FEBS Lett* 579: 500–506.
43. Sled VD, Rudnitsky NI, Hatefi Y, Ohnishi T (1994) Thermodynamic analysis of flavin in mitochondrial NADH:ubiquinone oxidoreductase (complex I). *Biochemistry* 33: 10069–10075.
44. Massari S, Frigeri L, Azzone G (1972) A quantitative correlation between the kinetics of solutes and water translocation in Liver Mitochondria. *J Membr Biol* 9: 71–82.
45. Lass A, Agarwal S, Sohal RS (1997) Mitochondrial ubiquinone homologues, superoxide radical generation, and longevity in different mammalian species. *J Biol Chem* 272: 19199–19204.

9 ANNEX 3: Supporting table for the sensitivity analysis of model M7

	χ^2 : st4	+rot	Suc-u	Pyr-u	SQ@Qo: st4	+rot	Suc-u	Pyr-u	st4pyr	SQ@I: st4	+rot	Suc-u	Pyr-u	st4pyr	FMN: st4	+rot	Suc-u	Pyr-u	st4pyr	N2: st4	+rot	Suc-u	Pyr-u	st4pyr
Complex III																								
K _{qp FS}	-1,738E-05	-9,08388E-05	-0,00028107	7,23E-07	2,73645E-05	3,017E-05	0,0001062	1,282E-05	4,704E-05	-3,492E-06	4,778E-05	7,431E-06	-3,918E-07	-2,266E-05	2,48E-07	5,256E-05	4,274E-06	-9,999E-08	1,273E-06	-5,03E-06	6,266E-06	5,294E-06	-5,641E-07	-2,669E-05
K _{qp FS}	3,978E-08	0,00010539	1,1307E-07	-2,681E-07	-1,55695E-08	-5,313E-05	-8,741E-09	7,169E-08	2,591E-06	2,075E-07	5,609E-05	-1,097E-09	5,382E-08	-8,206E-06	1,767E-08	6,17E-05	-6,243E-10	3,058E-08	-8,944E-07	2,268E-07	7,083E-05	-9,324E-10	3,386E-08	-8,221E-06
K _{FS c1}	-0,0017333	4,85914E-05	0,00339271	-2,815E-06	0,00178442	0,0017648	-0,0004631	3,175E-05	0,0047506	-7,644E-05	0,0006387	-4,3E-05	1,337E-07	-0,0014567	4,786E-05	0,0007025	-2,438E-05	3,133E-07	0,0002968	-0,000225	-0,0001905	-3,126E-05	-5,17E-07	-0,001946
K _{FS c1}	0,0017119	-0,000706114	3,5234E-05	2,47E-07	-0,00127788	-0,0019815	2,095E-05	-3,066E-05	-0,0047412	-0,0009503	-0,0084975	4,486E-06	3,769E-07	0,0014511	-9,731E-05	-0,0093473	2,458E-06	-2,015E-08	-0,0002966	-0,0009013	0,0003037	3,724E-06	8,37E-07	0,0019397
K _{qp bl}	-0,0059017	0,0103588	-0,0005165	-8,446E-06	-0,184062	-0,182053	-0,0427978	-0,0534443	-0,249662	-1,291E-05	-0,0022095	4,726E-06	6,498E-07	-0,0047345	0,0001819	-0,0024304	2,817E-06	7,935E-07	0,0009887	-0,0005261	-0,0011825	1,959E-06	-1,73E-06	-0,0063814
K _{qp bl}	0,004262	0,000525751	0,00228367	9,815E-06	0,154588	0,152602	0,0413037	0,0521821	0,224247	-0,003065	-0,0101662	-1,692E-05	-9,409E-07	0,0035471	-0,0006237	-0,0111829	-9,756E-06	-9,541E-07	-0,0007441	-0,0025558	0,0004744	-1,037E-05	1,506E-06	0,0047889
K _{bl bh}	-0,0075257	0,00474002	-0,00220415	-7,789E-06	-0,216184	-0,214258	-0,0300294	-0,0354286	-0,277463	-0,0003213	0,0007003	1,612E-05	9,078E-07	-0,0059041	0,0001288	-0,0007704	9,263E-06	7,737E-07	0,00123	-0,0008845	-0,0008364	1,06E-05	-7,481E-07	-0,0079506
K _{bl bh}	0,0046029	0,00891822	-0,00068468	6,555E-06	0,191609	0,191525	0,0266921	0,0313419	0,260404	-0,0042843	-0,0071529	6,674E-06	-5,058E-07	0,005167	-0,0005981	-0,0078682	3,721E-06	-5,227E-07	-0,0010814	-0,0038954	0,0001434	5,502E-06	8,562E-07	0,0069658
K _{bh-qn1}	-0,0036937	0,00869274	0,00073596	-3,851E-06	-0,101269	-0,0996518	-0,0182364	-0,0211463	-0,133228	-0,0014429	-0,0024286	-2,375E-06	3,651E-07	-0,0025073	-6,517E-05	-0,0026715	-1,298E-06	3,671E-07	0,0005176	-0,0017334	-0,0009203	-1,939E-06	-5,45E-07	-0,0033711
K _{bh-qn1}	0,0038004	0,00853512	0,00021383	1,387E-05	0,0995167	0,0975628	0,0180828	0,0209002	0,1312	0,0015779	-0,0124602	-3,76E-07	-0,000127	0,0024091	2,521E-05	-0,0137062	-2,603E-07	-7,234E-05	-0,0005056	0,0019444	-0,0001311	7,283E-08	-7,463E-05	0,0032484
K _{bh-qn2}	-0,0024965	0,00914613	0,00058861	-1,623E-08	-0,0820572	-0,0824589	-0,0025583	-0,0037616	-0,109181	0,0002369	-0,004321	-8,796E-07	2,321E-07	-0,0015351	0,0001001	-0,0047531	-4,933E-07	1,541E-07	0,0005918	1,958E-05	-0,0011718	-4,382E-07	1,243E-08	-0,0023523
K _{bh-qn2}	0,0027753	-0,000754761	9,3459E-05	-5,726E-08	0,0731225	0,072753	0,0015946	0,0023583	0,098615	0,0010544	-0,000447	-9,014E-07	6,218E-08	0,0015081	-3,868E-05	-0,0004917	-5,172E-07	2,164E-08	-0,0003223	0,0013665	0,0002731	-5,991E-07	1,247E-07	0,0020448
K _{qHbnd}	-0,0028726	-0,00278466	-0,00088315	-4,79E-05	-0,0868279	-0,0852892	0,0001104	-3,144E-05	-0,146216	-0,0053572	0,0018423	6,015E-06	-8,953E-06	-0,0015611	-0,0004783	0,0020265	6,318E-06	3,207E-06	0,0002788	-0,0055585	0,0004199	-7,573E-06	-2,644E-05	-0,0019997
K _{qHbnd}	0,0009688	0,000245291	0,00731964	-1,499E-07	0,0839622	0,0844259	-0,0006032	0,0001034	0,144004	0,0006666	-0,000614	-6,312E-05	3,007E-07	0,0013064	1,122E-05	-0,0006754	-3,599E-05	9,554E-09	-0,0002326	0,0007263	0,0001812	-4,486E-05	5,599E-07	0,0016663
K _{qnbnd}	-0,0026453	0,000176513	-0,00022554	2,259E-06	-0,0848749	-0,0845545	-0,0002586	-0,0003394	-0,102765	-0,0002009	0,0009127	2,137E-06	-4,29E-07	-0,0016909	6,813E-05	0,0010039	1,218E-06	-2,4E-07	0,0004929	-0,0004221	-0,0002952	1,859E-06	1,459E-07	-0,0023942
K _{qnbnd}	0,0022008	-0,000187559	0,00017355	-4,11E-06	0,0755221	0,0753415	0,0002551	0,0003315	0,0981792	0,0001771	-0,0007538	-1,626E-06	7,922E-07	0,0014171	-5,608E-05	-0,0008291	-9,266E-07	4,494E-07	-0,0002959	0,0003607	0,0002512	-1,481E-06	1,059E-07	0,0019013
K _{qpdis}	-0,0036121	0,00287574	-0,00099254	-0,0001311	-0,143247	-0,142856	-0,0144924	-0,0184443	-0,207969	0,001648	-0,0086523	8,189E-06	1,042E-05	-0,0033852	0,0002607	-0,0095175	6,572E-06	1,138E-05	0,0007099	0,0013758	-0,0002947	-1,29E-05	-2,037E-05	-0,0045729
K _{qpdis}	0,0016793	-0,00475567	0,00520317	0,0001299	0,10198	0,101272	0,00136172	0,01794	0,174482	-0,0010132	0,0015169	-4,133E-05	-1,193E-05	0,0015381	-9,856E-05	0,0016686	-2,543E-05	-1,224E-05	-0,0003293	-0,0009572	0,0005593	-1,143E-05	1,929E-05	0,0020955
K _{qndis}	-0,0027429	0,0095208	-0,00128252	-1,351E-06	-0,0862526	-0,0864704	-0,0029054	-0,0039463	-0,106237	0,0002954	-0,0031749	6,743E-06	1,575E-07	-0,001263	0,0001089	-0,0034924	3,85E-06	1,12E-07	0,000541	5,517E-05	-0,0011063	4,814E-06	-4,384E-08	-0,0019974
K _{qndis}	0,0027222	-6,61953E-05	0,000702	-9,198E-07	0,0833319	0,0830015	0,0001203	0,0001637	0,102739	-8,158E-05	-0,0008356	-1,977E-06	2,468E-07	0,00152	-8,765E-05	-0,0009191	-1,125E-06	1,39E-07	-0,0003238	0,0001576	0,000328	-1,142E-06	1,631E-07	0,0020642
K _{ctc}	-0,271943	0,00695542	0,00517065	8,853E-05	0,267563	0,270673	6,797E-05	0,0005034	0,573946	-0,0213408	0,10528	-6,895E-05	5,372E-05	-0,176714	0,0072042	0,115808	-3,83E-05	3,279E-05	0,0351001	-0,0456992	-0,0305519	-4,793E-05	2,745E-05	-0,234925
Complex I																								
K _{i10}	0,0624232	7,31417E-05	0,00091658	-0,085637	0,000645134	-5,12E-05	0,001318	0,0144984	-0,095677	0,0039886	0,0655357	0,0013973	0,0175731	0,1358	0,0010266	0,0720893	0,0007966	0,0099892	0,0155787	0,0033411	-0,0008068	0,0008341	0,0104276	0,133505
K _{i10}	-0,0632384	3,32211E-05	0,0110904	0,0842812	-0,00165015	-1,89E-06	-0,0024558	-0,0137075	0,0906813	-0,0056828	-0,0652517	-0,0014737	-0,0166005	-0,127862	-0,0012889	-0,0717769	-0,0008401	-0,0094364	-0,0146585	-0,0049724	0,0008748	-0,000892	-0,0098509	-0,125706
K _{i11}	0,123545	-3,57218E-05	0,00067059	-0,0814081	0,0011926	1,91E-06	0,0013314	0,0137634	-0,113486	0,0071516	0,0655717	0,0013813	0,0165784	0,152837	-0,0170289	0,0720939	0,0007337	0,0086859	-0,0090571	0,0182365	-0,0008365	0,0008278	0,0098897	0,168607
K _{i11}	-0,118217	0,000138165	0,00322081	0,0188053	-0,00332259	-5,511E-05	-0,0005425	-0,0031114	0,0838677	-0,0130104	-0,0652948	-0,0003054	-0,0036945	-0,10988	0,0166237	-0,0717889	-0,0001354	-0,0015499	0,0135907	-0,0243999	0,0009047	-0,0001871	-0,002231	-0,1261
K _{i12}	0,0618946	0,00623609	-0,00194479	-0,0187146	0,000959311	0,0001149	0,0004738	0,0032207	-0,0603894	0,00079139	0,058921	0,0002998	0,0039108	0,0884587	6,835E-05	0,0542203	2,943E-05	0,0002371	0,0033901	0,0059997	-0,0107061	3,966E-05	0,0003384	0,0803135
K _{i12}	-0,0589224	-0,00226659	0,00745685	0,018938	0,000401576	1,847E-06	-0,0010574	-0,0033001	0,0615404	-0,0034905	-0,0679768	-0,0003643	-0,0036631	-0,0886703	0,0002973	-0,0642027	-6,506E-05	-8,014E-05	-0,003213	-0,0013098	0,010585	-8,295E-05	-0,0001746	-0,0806151
K _{i13}	0,12356	0	-0,00230292	-0,0255023	0,000781008	0	0,0005215	0,0042747	-0,155102	-0,11521	0	-0,0025205	-0,0345347	0,028969	-0,0220994	0	-0,0014188	-0,0194936	-0,0619556	-0,085003	0	-0,0013625	-0,0186268	0,106418
K _{i13}	-0,115656	0	1,2385E-05	0,0002485	-0,000988347	0	-3,751E-06	-4,158E-05	0,0901544	0,113889	0	2,176E-05	0,0002742	0,010803	0,0217112	0	1,257E-05	0,0002013	0,0213842	0,0839719	0	1,15E-05	0,0001085	-0,0226445
K _{i16}	0,120596	-2,29715E-07	-0,00001134	-0,0002808	0,0102275	-4,748E-07	3,662E-06	4,694E-05	-0,0904797															

10 ANNEX 4: Roadmap

- **October 2011 to June 2012** - Mapping of skeletal muscle gene expression into the integrated mechanistic model (M8) to establish semantic interoperability between mechanistic and probabilistic modelling (Subsection 4.3.1).
- **December 2011 to December 2012** - Assessment of associations between estimated ROS levels with mechanistic modelling and blood & skeletal muscle nitroso-redox stress measured in healthy subjects and in COPD patients in Biobridge pre- and post-endurance training and interactions of nitroso-redox stress (estimated and measured) within an enhanced network analysis will be explored (Subsection 4.3.1).
- **December 2011** - validation of the integration of lung heterogeneities within M6 (Subsection 3.2.2) and model optimization of this subset of M6 (Section 2).
- **January 2012 to February 2012** - we will be completing integration of heterogeneities of peripheral gas exchange into the M6 module (Section 3.2.2) and we will address model optimization of M8. Moreover, specific interventions on M3 will be done and model optimization for M3 completed (Section 2).
- **March 2012** - Operational prototype of the entire vertical integration by early and completed model optimization within that month (Section 2).
- **June 2012 to February 2013** - Identification of shared pathways among clusters of comorbidities observed in COPD patients of the Medicare dataset (Subsection 4.3.3).
- **June 2012 to October 2012** - Explore novel ways for quantitative assessment of the interactions between the two modalities of modelling (Subsection 4.3.1).
- **June 2012 to February 2013** - Identification of differential pathways between Group I and Group III. Exploring the role of nitroso-redox stress on the systemic effects of the disease (Subsection 4.3.2).
- **November 2012 to June 2013** - Identification and validation of biomarkers with potential clinical applications (Subsection 4.3.2).
- **November 2012 to June 2013** - Identification of shared pathways among clusters of comorbidities observed in PAC-COPD (entire study and group III) (Subsection 4.3.3).
- **November 2012 to June 2013** - Explore novel ways for quantitative assessment of the interactions between the two modalities of modelling (Subsection 4.3.3).